UNIVERSITY OF CALIFORNIA SAN DIEGO
SAN DIEGO STATE UNIVERSITY

Structural and Mechanistic Investigations of the N6-threonylcarbamoyladenosine Biosynthesis System in Bacteria

A Dissertation submitted in partial satisfaction of the requirements
for the degree Doctor of Philosophy

in

Chemistry

by

Ana Kutchuashvili

Committee in charge:

University of California San Diego
Professor Kevin Corbett
Professor Kimberly Schurmeier
Professor Navtej Toor

San Diego State University
Professor Manal Swairjo, Chair
Professor Tom Huxford

2026

The Dissertation of Ana Kutchuashvili is approved, and it is acceptable in quality and form for publication on microfilm and electronically.

Chair

University of California San Diego

San Diego State University

2026

Dedication

I dedicate this work to my husband and my sister. My sister's determination and confidence in me have continually inspired me to pursue my goals. My husband shared this Ph.D. journey with me in the same laboratory, and his support, encouragement, and steady optimism helped me stay focused and persistent through its many challenges.

Table of Contents

List of Figures

List of Tables

Acknowledgements

Chapter 2, in part is currently being prepared for submission for publication of the material. Kutchuashvili, A., Wood, E., Scheleen, E., Luthra, A., Sankaran, B., Iwata-Reuyl, D., Swairjo, M.A. “Structure–Function Analysis of the *Thermotoga maritima* t^6A Biosynthesis Enzyme TsaC2”. The dissertation author was the primary researcher and author of this material.

Chapter 3, in part is a reprint of the material as it appears in Kutchuashvili, A., Scheleen, E., Guynes, G., Wu, J., Chan, C.K., Dedon, P., Iwata-Reuyl, D. and Swairjo, M.A., 2026. Anticodon loop remodeling and D-stem shape drive the specific recognition of ANN-decoding tRNAs for t^6A modification. *Nucleic Acids Research*, *54*(11), p.gkag599. The dissertation author was the first author of this paper.

In Chapter 4, Figure 4-1A is adapted from material currently being prepared for publication: Kutchuashvili, A., Wood, E., Scheleen, E., Luthra, A., Sankaran, B., Iwata-Reuyl, D., and Swairjo, M. A., “Structure–Function Analysis of the *Thermotoga maritima* t^6A Biosynthesis Enzyme TsaC2.” The figure and the underlying data were generated by Erik Scheleen and Prof. Dirk Iwata-Reuyl.

I would like to express my deepest gratitude to my advisor, Prof. Manal Swairjo, for her guidance, support, and mentorship throughout my Ph.D. I am grateful for the many opportunities she provided and especially thankful that she believed in my ability to take on and accomplish challenging projects.

I would also like to thank my committee members for their guidance and support throughout this process and for helping me stay on track toward completing my degree. I am

especially grateful to Prof. Kevin Corbett and Prof. Navtej Toor for their help with cryo-EM data processing, and to Prof. Tom Huxford for his advice, encouragement, and general guidance.

I am grateful to Dr. Nathan Burrows from SLAC National Accelerator Laboratory for training me in cryo-EM grid preparation and for his help with data processing. I would also like to thank Dr. Marzia Miletto from the Pacific Northwest Center for Cryo-EM (PNCC) for training me in cryo-EM grid screening.

I would like to acknowledge our collaborators at Portland State University, Prof. Dirk Iwata-Reuyl and Erik Scheleen, whose contributions were essential to the work presented in this dissertation.

I would also like to thank my fellow graduate students for helping me troubleshoot experiments, discuss ideas, practice presentations, and navigate the many challenges of graduate school. Their support helped me grow as a scientist and get through some challenges of my Ph.D.

Vita

2020 Bachelor of Science in Chemistry, San Diego State University Georgia

2026 Doctor of Philosophy in Chemistry, University of California San Diego/San Diego State University

Publications

Ana Kutchuashvili, Erik Scheleen, George Guynes, Junzhou Wu, Chi-Kong Chan, Peter Dedon, Dirk Iwata-Reuyl, Manal A Swairjo, Anticodon loop remodeling and D-stem shape drive the specific recognition of ANN-decoding tRNAs for t^6A modification, *Nucleic Acids Research*, Volume 54, Issue 11, 24 June 2026, gkag599, https://doi.org/10.1093/nar/gkag599.

Ho-Ching Tiffany Tsui, Chi-Kong Chan, Yifeng Yuan, Roba Elias, Jingjing Sun, Virginie Marchand, Marshall Jaroch, Guangxin Sun, Irfan Manzoor, Ana Kutchuashvili, Grazyna Leszczynska, Kinda Seaton, Yuri Motorin, Kelly Rice, Manal Swairjo, Peter C. Dedon, Malcolm E. Winkler, Valérie de Crécy-Lagard; tRNA modification landscapes in streptococci: shared losses and clade-specific adaptations. *Open Biol* 1 April 2026; 16 (4): 250445. https://doi.org/10.1098/rsob.250445.

Field of Study

Major Field: Biochemistry and Biophysics

Abstract of the Dissertation

Structural and Mechanistic Investigations of the N6-threonylcarbamoyladenosine Biosynthesis System in Bacteria

by

Ana Kutchuashvili

Doctor of Philosophy in Chemistry

University of California San Diego, 2026
San Diego State University, 2026

Professor Manal A. Swairjo, Chair

N^6-threonylcarbamoyladenosine (t^6A) is a universally conserved tRNA modification found at position 37 of ANN-decoding tRNAs (N is A, U, G or C) and is essential for accurate and efficient translation. t^6A37 biosynthesis occurs in two steps: synthesis of the pathway intermediate threonylcarbamoyladenylate (TC-AMP) by TsaC/TsaC2 enzymes, followed by

transfer of the threonylcarbamoyl moiety onto A37 of substrate tRNAs, catalyzed in bacteria by the threonylcarbamoyl transfer (TCT) complex. Although the enzymes responsible for t^6A37 biosynthesis have been identified and characterized biochemically, key mechanistic questions have remained unresolved, including how TsaC2 catalyzes TC-AMP formation and what drives substrate tRNA recognition. In this dissertation, I used X-ray crystallography, SEC-SAXS, cryo-EM, and biochemical assays to investigate t^6A biosynthesis in *Thermotoga maritima*. In Chapter 2, I performed time- and pH-dependent soaking of *Tm*TsaC2 crystals to capture substrate-, intermediate-, and product-bound states of the enzyme. These structures provide direct evidence for N-carboxy-L-threonine as a reaction intermediate. In addition, SEC-SAXS analysis revealed that *Tm*TsaC2 adopts a closed conformation in the presence of substrates in solution but exhibits high conformational flexibility in their absence. In Chapter 3, I used cryo-EM to determine structures of the *Thermotoga maritima* t^6A synthase bound to unmodified and t^6A-modified tRNA. These structures reveal that productive tRNA binding requires dramatic remodeling of the anticodon loop into a zig-zag conformation. tRNA is recognized through an indirect readout mechanism in which the key t^6A determinants, U36 and A38, form a base triple with U32 instead of making base-specific interactions with the protein. The tRNA D-stem is also recognized predominantly by shape rather than sequence-specific contacts. Together, these data fill important knowledge gaps in the t^6A field by defining key steps in TC-AMP synthesis and revealing how the bacterial t^6A synthase selects substrate tRNAs for modification. This work provides a structural and mechanistic foundation for future studies of this essential tRNA modification pathway.

Chapter 1: Introduction

1.1. transfer RNA: structure, function and modifications

Transfer RNA (tRNA) is an adaptor molecule in protein synthesis and plays a crucial role in accurate decoding of genetic information carried by messenger RNAs (mRNA). Most mature tRNAs are 76-90 bases long and adopt a cloverleaf-like secondary structure, composed of five regions: acceptor stem, D (dihydrouridine) arm, T (TΨC) arm, variable loop and anticodon stem-loop (ASL) (Fig. 1-1A). Tertiary interactions between D-loop and T-loop promote formation of L-shaped tertiary structure of tRNAs (Fig. 1-1B). tRNAs are aminoacylated at the 3′ end by aminoacyl-tRNA synthetases and then recruited to the aminoacyl site of ribosomes where the tRNA anticodon, specifically the bases at 34, 35 and 36 positions, pair with the three-base codon of mRNA. After the peptide bond forms and translocation takes place, tRNA migrates to the peptidyl site and then to the exit site of the ribosome.

Although all tRNAs adopt a common L-shaped structure, each species accepts a specific amino acid. tRNA recognition by aminoacyl-tRNA synthetases is supported by tRNA determinants and anti-determinants, mainly clustered in the anticodon and acceptor stem, in combination with the discriminator base 73 (3). Besides these determinants, aminoacylation efficiency can also be enhanced by tRNA modifications (4-8).

So far more than 170 chemical modifications have been discovered in RNAs, and more than half of them have been found in tRNAs (Fig. 1-1A) (9). Typical tRNAs carry around 8-13 chemical modifications (10). Modifications in the main body of the tRNA are relatively small in size and support its structural stability and flexibility (11). Dihydrouridine (D), pseudouridine (Ψ) and methylated and thiolated bases (e.g. 1-methyladenosine, m^1A, 4-thiouridine, s^4U) are the most abundant and conserved small modifications. On the other hand, modifications in the ASL,

especially at positions 34 and 37, tend to be more chemically complex and larger in size and they often contribute to proper selection of codons (12).

Position 34 base pairs with the wobble position of mRNA codons and these interactions can be either Watson-Crick or non-canonical base-pairing. The non-canonical wobble-tRNA interactions are often mediated by modifications at position 34, most frequently present in U34. Modifications at 34 can expand codon decoding capacity. For example, when A34 is converted to Inosine (I) through deamination, the tRNA can recognize codons with U, C or A in the wobble position, expanding beyond U-A base pairing (3, 13).

While modified purines at position 37 are not directly involved in codon-anticodon base pairing, they can stabilize the anticodon loop conformation and interactions with the mRNA codon. For instance, isopentyladenosine (i^6A) modification is added to UNN-decoding tRNAs at position 37 (N being any canonical nucleotide). This modification stabilizes U1:A36 base pairing and enhances the ability of tRNA to recognize the appropriate codon (14).

The role of tRNA modifications is underscored by their essentiality in cellular function and implications in human diseases such as neurological disorders, cancer, diabetes, and mitochondrial diseases. Clear examples of this are the neurodegenerative diseases Mitochondrial Encephalomyopathy, Lactic Acidosis and Stroke-like Episodes (MELAS), and Myoclonic Epilepsy with Ragged-Red Fibers (MERRF) (15, 16). These diseases are directly caused by mutations in tRNA genes which in turn result in the decreased levels of taurine modifications at the wobble position of the anticodon (17-20). Deficiencies in 5-taurinomethyluridine (τm^5U) and 5-tauromethyl-2-thiouridine (τm^5s^2U) interfere with the decoding capacity of tRNA and impair mitochondrial translational efficiency (21).

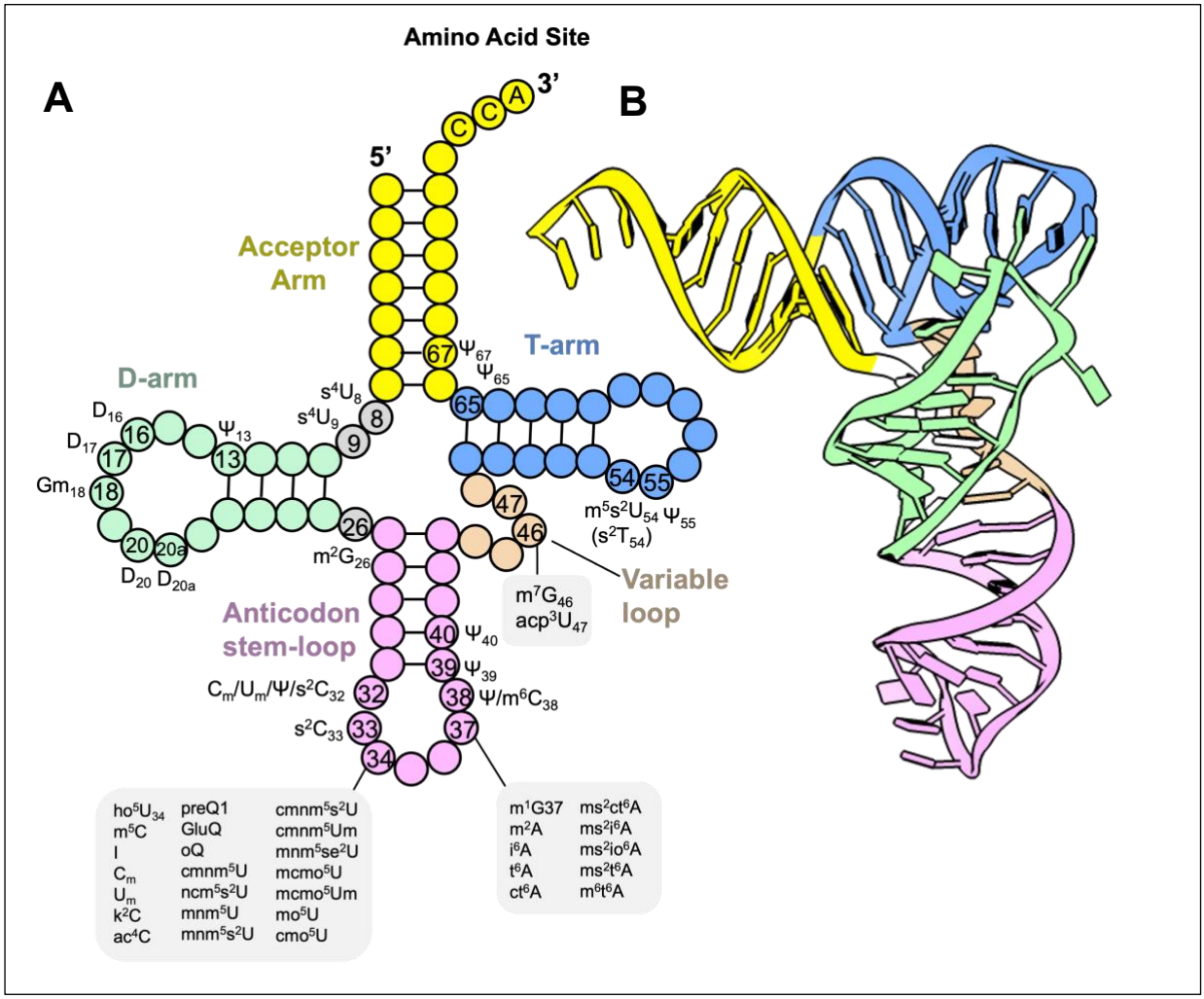

Figure 1-1: tRNA structure and modifications.
A) tRNA secondary structure showing modifications at various positions. **B)** Tertiary structure of *Thermotoga maritima* $tRNA^{Lys}_{CUU}$ as an example (AlphaFold3 model, visualized in ChimeraX).

1.2. N^6-threonylcarbamoyladenosine (t^6A37)

1.2.1. Structure and function of t^6A37

N^6-threonylcarbamoyladenosine (t^6A) is a universally conserved modified nucleoside at position 37 of tRNAs that decode ANN codons (N is A, G, U or C) (Fig. 1-2A) (8-12). In t^6A, the threonylcarbamoyl group is attached to the exocyclic N6 amino group of adenosine through a

ureido linkage. In free t^6A, the carbamoyl/ureido group adopts a coplanar orientation with A37 and the -NH from the threonylcarbamoyl (TC) moiety forms a hydrogen bond with N1 of A37 (22-24).

Because the t^6A37 modification is immediately adjacent to the anticodon, it plays an important role in accurate and efficient protein synthesis. The t^6A37 modification has been shown to significantly enhance the affinity of the ASL towards AAA-programmed ribosomes (25). Conversely, loss of t^6A37 promotes improper start codon selection, U36-U1(mRNA) mismatches, and frameshift events (26). In addition to its direct role in decoding, t^6A also supports aminoacylation efficiency, as reduced t^6A levels have been associated with decreased aminoacylation (7, 27-30).

Structural and NMR studies have provided insight into how t^6A37 supports these functions at the molecular level. Structures of ribosomes bound to modified ASLs or tRNAs and mRNAs show that t^6A37 acts as an additional ring-like extension of the adenine base. The modification stacks against U36 and A38, while the A37 base itself stacks against the U36-A1(mRNA) base pair in the ribosome decoding center (31-33). In some structures, the threonyl moiety also interacts with A38 and the modified wobble base, U34 (31, 33). Additionally, the bulky threonylcarbamoyl moiety prevents intraloop base pairing between A37 and U33, thereby maintaining a loop structure favorable for accurate decoding (34).

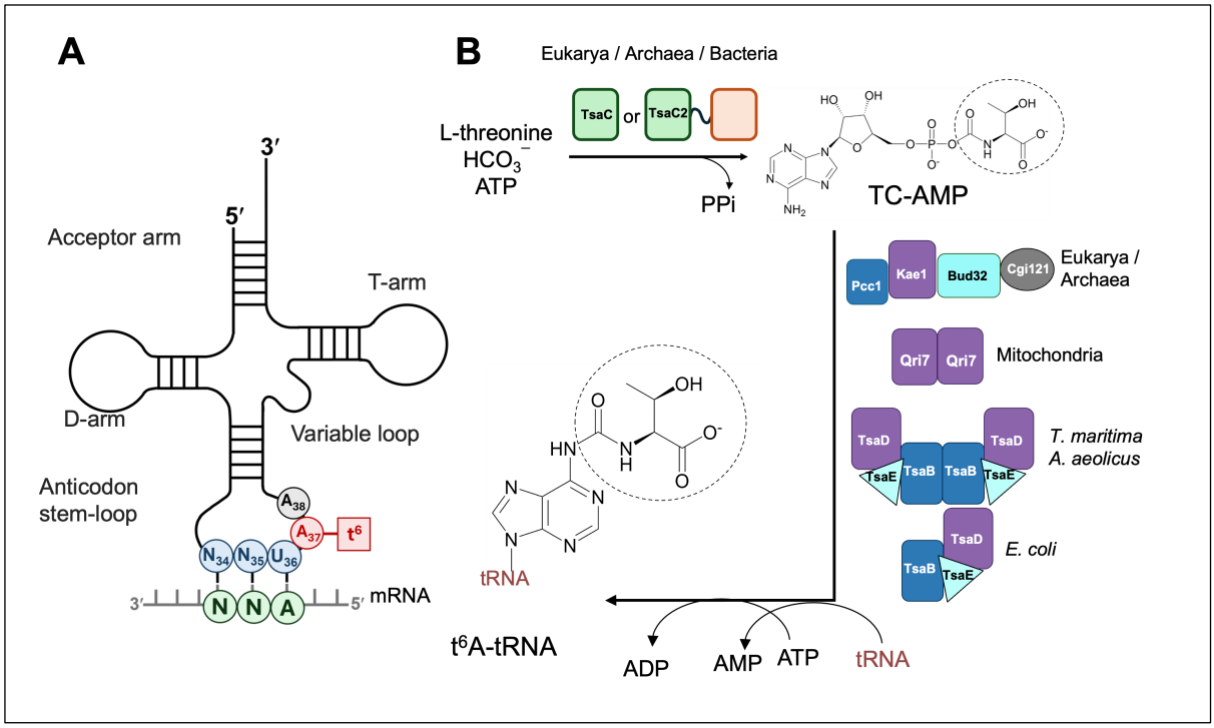

Figure 1-2: Location and biosynthesis of t^6A37.
A) Position of t^6A modification in ANN-decoding tRNAs. The universal determinant 36-UAA-38 sequence for t^6A modification is highlighted. N is any canonical nucleotide. **B)** The t^6A biosynthesis pathway across the three domains of life. TsaC/TsaC2 synthesizes TC-AMP from L-threonine, CO_2/bicarbonate and ATP. The transfer of the threonylcarbamoyl (TC) moiety onto the substrate tRNA is catalyzed by the KEOPS complex in eukarya and archaea, Qri7 in mitochondria, and by TsaB, TsaD and TsaE in bacteria.

1.2.2. The ancient origins of t^6A37

t^6A37 has been regarded as one of the "molecular fossils" of the origins of life, reflecting both its ancient chemical features and its broad conservation (35, 36). Its presence in bacteria, archaea, and eukaryotes, together with its role in stabilizing codon–anticodon interactions, supports the idea that t^6A emerged early during evolution of the genetic code, possibly before the divergence of modern organisms from the Last Universal Common Ancestor (LUCA) (37, 38). Recent work on a giant-virus enzyme system further supports the ancient origin of t^6A-related chemistry by showing that the threonylcarbamoyl group can be installed on ATP or ADP independently of tRNA (39). This expands the known scope of threonylcarbamoyl chemistry and

suggests that modern t^6A biosynthesis may have evolved from a more ancient biochemical system.

1.2.3. Biosynthesis of t^6A37

t^6A biosynthesis occurs in two major steps: synthesis of the pathway intermediate, threonylcarbamoyladenylate (TC-AMP) and transfer of the threonylcarbamoyl (TC) moiety from TC-AMP onto the tRNA substrate (Fig. 1-2B).

In the first step of the reaction, TsaC or TsaC2 enzymes utilize L-threonine, HCO_3^- or CO_2 and ATP to form TC-AMP (40-42). TsaC (also known as YRDC in some organisms) is a single-domain enzyme, whereas TsaC2 (also known as Sua5) contains a catalytic, N-terminal TsaC domain connected to a C-terminal SUA5 domain by a flexible linker (43-45). Although there is no strict phylogenetic pattern, TsaC is more commonly found in multicellular eukaryotes and mesophilic bacteria, while TsaC2/Sua5 is often present in Archaea, fungi and thermophilic bacteria (43, 45).

In the second step of the reaction, the TC moiety of TC-AMP is transferred to A37 of substrate tRNA. During this reaction, N6 of A37 acts as a nucleophile and attacks the carbamoyl carbon of TC-AMP, resulting in formation of the t^6A37. This step is catalyzed by a transferase embedded in a larger protein complex that differs across the domains of life. In bacteria, it is the threonylcarbamoyl transfer (TCT) complex, comprised of TsaD, TsaB and TsaE (2, 41, 42). In archaea and the cytosols of eukaryotes, it is the KEOPS (Kinase, putative Endopeptidase, and Other Proteins of Small size) complex, comprised of Kae1, Bud32, Cgi121 and Pcc1 (46-48), and in some eukaryotes and archaea, is regulated by an additional Gon7 or Pcc2 subunit, respectively (49). In mitochondria, the enzyme responsible for TC-transfer is the TsaD ortholog Qri7, functioning alone as a homodimer (50). The TsaD/Kae1/Qri7 protein family harbors the active site for the transfer reaction.

In bacteria, TsaB and TsaD associate to form a TsaB/TsaD hetero complex with a 1:1 stoichiometry (e.g. *Salmonella typhimurium* and *Escherichia coli* systems (51, 52)), or a 2:2 stoichiometry where TsaB serves as the dimerization module (e.g. *Thermotoga maritima* and *Aquifex aeolicus* systems (2, 53, 54)). This minimal complex binds tRNA and carries out the TC transfer reaction (2, 42, 53). In the absence of tRNA, TsaE binds to this minimal complex at the TsaB/TsaD interface in an ATP-dependent manner to form a 1:1:1 complex (*e.g. S. typhimurium* and *E. coli* (51, 52)) or a 2:2:2 complex (*e.g. T. maritima* (2, 53) and *A. aeolicus* (54)). TsaE is an atypical ATPase that belongs to the P-loop NTPase structural superfamily (55), and its ATPase activity is enhanced in the presence of TsaB and TsaD (2, 51, 53).

1.2.4. t^6A37 biosynthesis cycle in *Thermotoga maritima*

Among the bacterial t^6A biosynthesis systems characterized to date, that of *T. maritima* has been investigated most extensively at the mechanistic level and has served as the primary model for understanding the catalytic cycle. In *T. maritima*, the TC-AMP synthase is *Tm*TsaC2. In 2018, Luthra *et al.* showed that the 2:2 heterocomplex of *Tm*TsaB and *Tm*TsaD (*Tm*$TsaB_2D_2$) acts as the minimal tRNA-binding unit, and binds only one tRNA molecule despite containing two TC-transfer sites (53). *Tm*$TsaB_2D_2$ catalyzes one reaction cycle, and releases the modified tRNA product (2, 53). Further, using competition binding assays and SAXS analysis of the tRNA-bound complex, Luthra *et al.* showed that tRNA binding and ATP-dependent TsaE binding to *Tm*$TsaB_2D_2$ (the latter forms the *Tm*$TsaB_2D_2E_2$ complex) are mutually exclusive, demonstrating that TsaE and tRNA bind to overlapping sites on *Tm*$TsaB_2D_2$ (2, 53). Critically, using careful radiochemical assays, they showed that TsaE-catalyzed ATP hydrolysis is required for multiple turnover of the t^6A biosynthesis reaction (53). Based on these observations, a catalytic cycle has been proposed, in which the TCT complex becomes inactivated after one

round of reaction, and TsaE-mediated ATP hydrolysis serves to reset/re-activate the system for the next cycle (Fig. 1-3) (2).

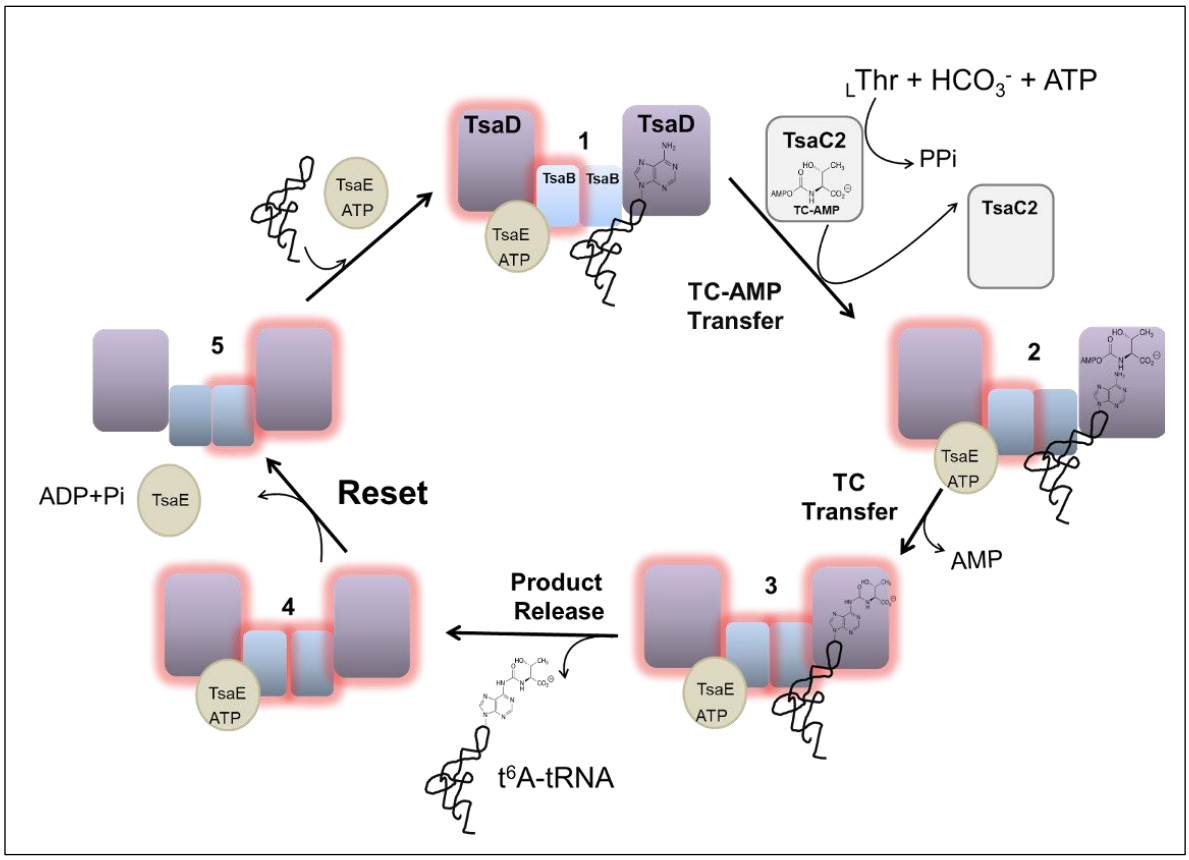

Figure 1-3: Proposed t^6A37 biosynthesis cycle in *T. maritima*. (figure from Luthra *et al*., 2019) (2).

1.2.5. t^6A37 derivatives

In some organisms, t^6A is further processed into hypermodified derivatives, including N^6-methyl-N^6-threonylcarbamoyladenosine (m^6t^6A), 2-methylthio-N^6-threonylcarbamoyladenosine (ms^2t^6A), and 2-methylthio cyclic N^6-threonylcarbamoyladenosine (ms^2ct^6A) (Fig. 1-4) (9). These derivatives expand the chemical diversity of t^6A-containing tRNAs and may further modulate decoding efficiency of the t^6A modification.

Methylation and thiomethylation are among the most common t^6A hypermodifications. The methyltransferase TrmO methylates the N^6 position of t^6A to form m^6t^6A, which likely further enhances the stacking capacity of the modified base (56). A methylthio group can also be installed at the C2 position of t^6A37 in $tRNA^{Lys}$, generating ms^2t^6A. This reaction is catalyzed by the methylthiotransferase MtaB in bacteria, and by CDKAL1 in eukaryotic cytosolic and mitochondrial tRNAs (57-59).

t^6A can also be dehydrated to cyclic t^6A (ct^6A) by TcdA and its orthologs in an ATP-dependent manner (60). ct^6A is a predominant form of t^6A in some bacteria, fungi and plants and has been shown to support more efficient decoding of certain codons than uncyclized t^6A (60). In some organisms, ct^6A can be further thiomethylated by MtaB to form ms^2ct^6A (58).

Additional t^6A derivatives include hydroxy-N^6-threonylcarbamoyladenosine (ht^6A), first discovered in sea urchin mitochondria. ht^6A helps reassign the AAA codon from lysine to asparagine in mitochondria, by restricting mitochondrial $tRNA^{Lys}$ decoding to the AAG codon and preventing its binding to the AAA codon (61). However, it remains unclear whether the hydroxyl group is added after t^6A formation or whether 4-hydroxythreonine is directly used by the t^6A biosynthesis machinery. Similarly, N^6-hydroxynorvalylcarbamoyladenosine (hn^6A) and 2-methylthio-N^6-hydroxynorvalylcarbamoyladenosine (ms^2hn^6A) are found in some thermophiles (62-64), and the *T. maritima* and *E. coli* t^6A37 biosynthesis enzyme systems have been shown to use hydroxynorvaline (instead of L-threonine) to form hn^6A37-modified tRNA *in vitro* (65).

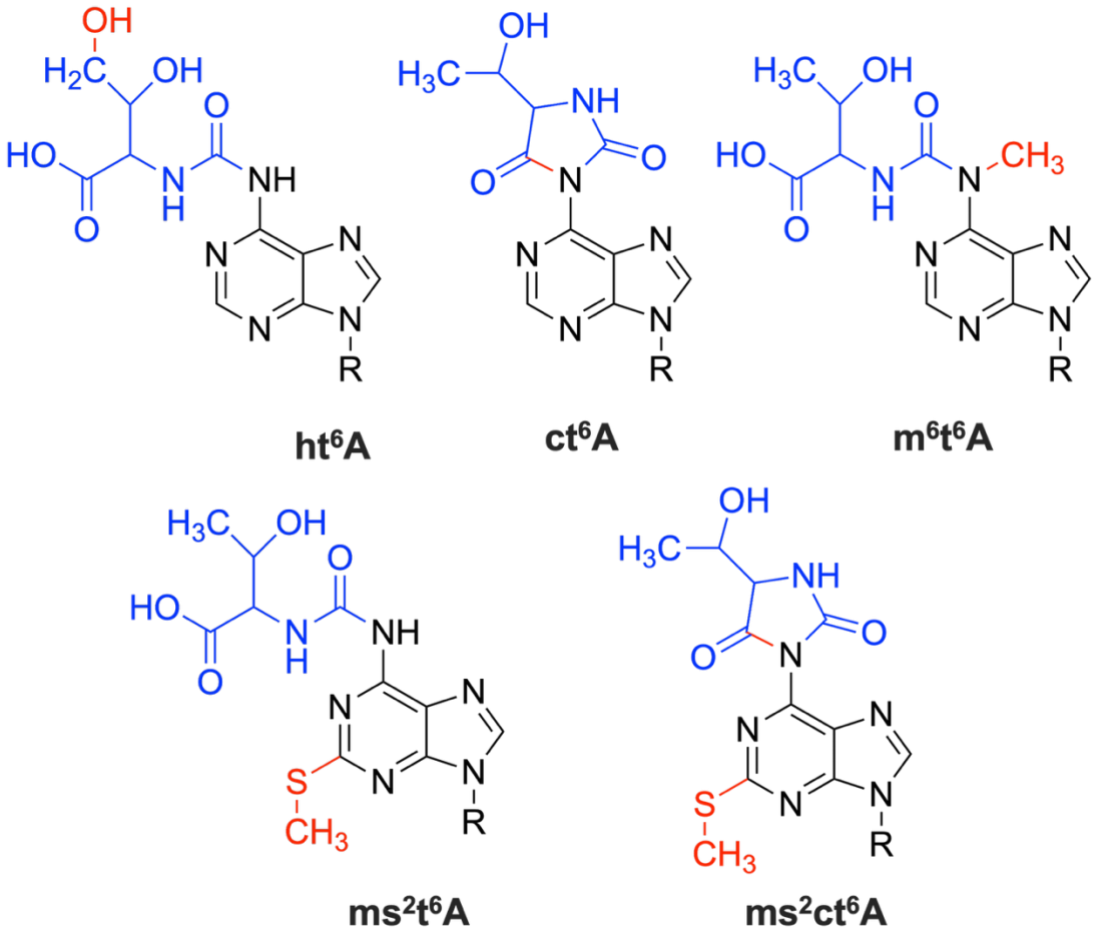

Figure 1-4: t^6A derivatives.
The t^6A moiety is highlighted in blue, additional groups shown in red. R=ribose.

1.2.6. Essentiality of t^6A37

The importance of t^6A37 is underscored by its requirement for normal cellular function across diverse organisms. In humans, mutations in t^6A37 biosynthesis genes cause Galloway-Mowat syndrome (GAMOS), a rare disorder characterized by steroid-resistant nephrotic syndrome (SRNS) accompanied by neurological impairment (66-68). GAMOS-associated mutations have been identified in YRDC and KEOPS genes and can disturb t^6A biosynthesis by affecting catalytic sites, KEOPS complex assembly, individual protein expression, or folding (24).

t^6A37 modification is essential for cell growth. Absence of t^6A37 causes severe growth defects in yeast and drosophila (40, 69-71). In some bacterial species, such as *Escherichia coli*, *Streptococcus pneumoniae, Staphylococcus aureus, and Pseudomonas aeruginosa,* t^6A37 modification is essential for viability (7, 72, 73). Even in species where t^6A37 is not strictly required, loss of the modification can impair normal cellular function, leading to defects in cell morphology and growth, compromised biofilm formation, and increased sensitivity to oxidative stress (74, 75). As mentioned earlier, the essentiality of t^6A37 in bacteria may reflect not only its role in decoding but also its contribution to tRNA aminoacylation and broader cellular physiology. In *S. pneumoniae*, t^6A37 synthesis genes are essential; however, deletion of *tsaE* can be tolerated in the presence of a suppressor mutation in the *asnS* gene*,* corresponding to Asp121Ala substitution in asparaginyl-tRNA synthetase (AsnRS) (73). This suggests a functional connection between t^6A37 biosynthesis and recognition of $tRNA^{Asn}$ for aminoacylation in this organism. To explore this possibility, I generated a structural model of the AsnRS/$tRNA^{Asn}$ complex using an AlphaFold2 model of *S. pneumoniae* AsnRS (*Sp*AsnRS) and available structures of class IIb synthetases bound to their cognate tRNAs as references (Fig. 1-5) (76-78). In this model, the linker connecting the catalytic and anticodon-binding domains of *Sp*AsnRS contacts both the tRNA acceptor stem and anticodon loop: Asp121 is positioned to interact with the 2′-OH of ribose 67, while Lys116 may contact t^6A37, similar to interactions observed in the recently determined structure of human lysyl-tRNA synthetase (LysRS) bound to $tRNA^{Lys}$ (77). In case of t^6A37 loss, the Asp121Ala mutation may allow the linker to adopt an alternative conformation that preserves productive tRNA binding. Thus, t^6A37 may act as a positive determinant for recognition of $tRNA^{Asn}$ by wild-type *Sp*AsnRS, while the Asp121Ala

suppressor mutation may relax this requirement, allowing aminoacylation of unmodified $tRNA^{Asn}$ sufficiently enough to support growth in the absence of t^6A37.

Because t^6A37 is essential in most bacterial species, the bacterial t^6A biosynthesis system represents an attractive target for the development of new antibiotics against pathogenic bacteria. TsaB and TsaE are particularly promising targets because they are bacterial-specific proteins and essential components of the bacterial t^6A biosynthesis pathway (79).

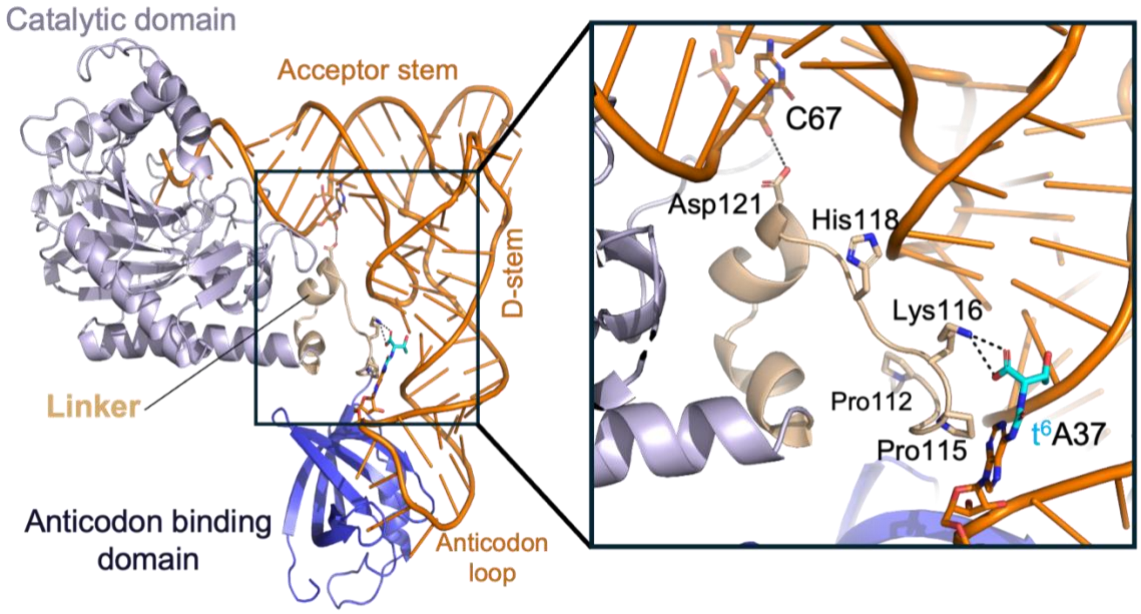

Figure 1-5: Model of t^6A-modified $tRNA^{Asn}$ bound to *Streptococcus pneumoniae* asparaginyl-tRNA synthetase (*Sp*AsnRS) (73).
*Sp*AsnRS is shown in purple, with its interdomain linker region highlighted in tan. Potential interactions between linker residues and C67 at the base of the tRNA acceptor stem, as well as with t^6A37, are shown as dashed lines. The threonylcarbamoyl moiety of t^6A37 is highlighted in cyan.

Chapter 2: TC-AMP synthesis by *Tm*TsaC2

2.1. Introduction

The first step of the t^6A biosynthesis is the formation of the pathway intermediate, TC-AMP from L-threonine, ATP, and CO_2/bicarbonate. The reaction is catalyzed by either TsaC/YrdC or TsaC2/Sua5 enzymes (42). These two enzyme families contain orthologous catalytic domains; however, TsaC2/Sua5 contains an additional C-terminal segment comprising a linker and SUA5 domain, both of which are required for TsaC2 activity (44). There is no strict phylogenetic pattern in the distribution of TsaC and TsaC2 enzymes. A bioinformatics study by Pichard-Kostuch *et al.* suggested that TsaC arose from TsaC2 through repeated loss of the SUA5 domain during evolution (45). This study also identified protein residues that are conserved in TsaC but not in TsaC2, and vice versa, and proposed that these residues may support distinct ligand-binding modes in the two enzyme varieties.

Lauhon extensively characterized TC-AMP synthesis and stability (42). TC-AMP is relatively unstable in solution, with a half-life of 3.5 min at pH 7.5, 37°C and 2 mM magnesium chloride. TC-AMP readily undergoes hydrolysis to AMP and equimolar amounts of L-threonine or oxazolidinone, a cyclized form of N-carboxy-L-threonine. Increasing temperature or magnesium concentration further destabilizes TC-AMP. *E. coli* TsaC catalyzes the formation of TC-AMP while producing only a small amount of AMP. In contrast, *B. subtilis* TsaC2 generates a large excess of AMP unless inorganic pyrophosphatase is included in the reaction; under those conditions, its products profile resembles that of *E. coli* TsaC. Because the reaction generates only substoichiometric amounts of AMP, Lauhon argued that TC-AMP formation may not require an ATP-activated bicarbonate intermediate. Instead, he proposed that the reaction proceeds through N-carboxy-L-threonine, or L-threonine carbamate, formed by the reaction of L-

threonine with CO_2 (Fig. 2-1). N-carboxy-L-threonine can then react directly with ATP to form TC-AMP and pyrophosphate (Fig. 2-1).

Several structural studies of Sua5 enzymes from *S. tokodaii* and *P. abyssi* (*St*Sua5 and *Pa*Sua5, respectively) have been reported. In the first *St*Sua5 structure, the bound ligand was initially modeled as AMP and was later remodeled as TC-AMP (PDB ID: 4E1B) (80). A second *St*Sua5 structure contained L-threonine and AMPPNP (PDB ID: 3AJE) (80, 81). Several *Pa*Sua5 structures have also been reported, revealing a fully ordered linker for the first time and showing the protein bound to threonine or to threonine and pyrophosphate (PPi) (82).

In this study, I use timed crystal soaking, X-ray crystallography, and SEC-SAXS (Size-Exclusion Chromatography coupled to Small-Angle X-ray Scattering) to elucidate the mechanism of the TsaC2-catalyzed reaction and to understand the roles of the SUA5 domain and linker in catalysis.

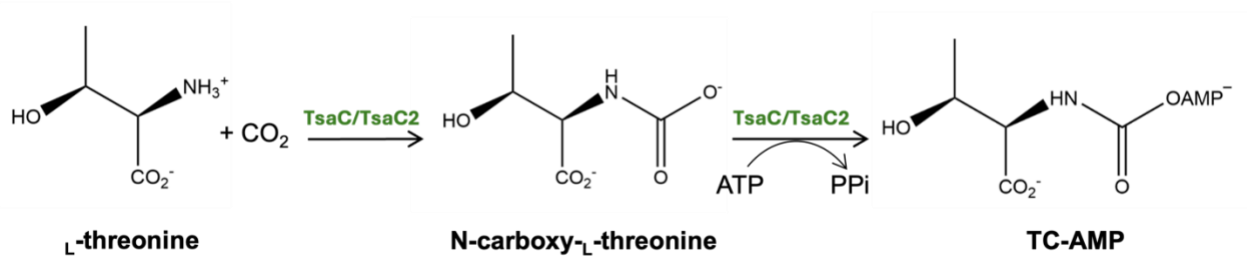

Figure 2-1: The TC-AMP biosynthesis reaction as proposed by Lauhon (42).

2.2. Methods

2.2.1. Preparation of wild-type and mutant *T. maritima* TsaC2

Cloning of the *T. maritima tsa*C2 gene (NCBI accession number AGL49779) into a pET-28a expression vector with the N-terminal His_6 tag followed by a thrombin cleavage site (construct pET28a-tsaC2) was described previously (53). *Tm*TsaC2 wild-type and mutant

proteins were purified as described previously with minor modifications (53). Briefly, *Tm*TsaC2 was overexpressed in *E. coli* C41 cells. The clarified lysate was heated at 60ºC for 30 minutes. The first purification step was performed by Ni-NTA affinity chromatography. After overnight thrombin digestion to remove the His_6 tag, the protein was further purified by size-exclusion chromatography (SEC) using an ENrich™ SEC 650 column (10 × 300 mm; Bio-Rad Laboratories) equilibrated in 50 mM Tris-HCl, pH 7.5, 50 mM KCl, and 1 mM DTT. The protein was stored at -80ºC and protein purity was verified by SDS-PAGE (sodium dodecyl sulfate–polyacrylamide gel electrophoresis). The purified *Tm*TsaC2 samples were heated at 60ºC for 30 minutes before use to eliminate any *E. coli* protease contamination.

Point mutagenesis was performed using the Q5® Site-Directed Mutagenesis Kit (NEW ENGLAND Biolabs Inc.). Nucleotide sequences were confirmed by sequencing (Genewiz, Inc., South Plainfield, NJ). Mutant proteins were overexpressed and purified using the same procedures used for the wild type enzyme.

2.2.2. Crystallization and structural determination

*Tm*TsaC2 crystals were grown at 20 ºC in a Cryschem M 24-well sitting drop plates by mixing 1.5 µl protein with 1.5 µl reservoir solution and equilibrating the drops against 500 µl reservoir solution. In all experiments, the protein stock contained 25 mg/mL *Tm*TsaC2 (660 µM), 10 mM L-threonine, 50 mM Tris-HCl, pH 7.5, 50 mM KCl and 1 mM DTT. The reservoir solution only for the *Tm*TsaC2/Thr-ATP crystal contained 80 mM sodium cacodylate, pH 6.5, 160 mM calcium acetate, 14% polyethylene glycol 8000 (PEG8000), 20% glycerol. The reservoir solution for all other crystals contained 80 mM sodium cacodylate, pH 7.5, 130-230 mM sodium acetate, 13-14% PEG 8000, 20% glycerol.

For the structure in complex with L-threonine only (*Tm*TsaC2/Thr), the crystal was directly cryoprotected in mother liquor supplemented with 20% glycerol and flash-cooled in

liquid nitrogen. All the other crystals were soaked in a solution containing 10 mM L-threonine, 10 mM ATP, 10 mM magnesium chloride, 30 mM sodium bicarbonate; for the *Tm*TsaC2/TC-AMP-PPi crystal, 0.11 unit/µl inorganic pyrophosphatase was also added. The soaking buffer for the *Tm*TsaC2/Thr-ATP crystal contained 80 mM sodium cacodylate, pH 6.5, 160 mM calcium acetate, 14.4% PEG8000 and 40% glycerol. After a 10-minute soak, the crystal was immediately frozen in liquid nitrogen. The soaking buffer for the other crystals contained 80 mM sodium cacodylate, pH 7.5, 160 mM sodium acetate, 14.4% PEG8000, and 20% glycerol. The crystals were then cryoprotected in mother liquor supplemented with 20% glycerol and flash-frozen in liquid nitrogen. Soaking conditions, data collection and structure refinement statistics are summarized in the Table 2-1.

X-ray diffraction data were collected at the Stanford Synchrotron Radiation Lightsource (SSRL, Menlo Park, CA) beamlines 12-2 or 14-1, equipped with Pilatus CCD detectors; or at the National Synchrotron Light Source II (NSLSII, Long Island, NY) 17-ID-1 AMX beamline, equipped with Eiger 9M detector; or the Advanced Light Source (ALS, Berkeley, CA) beamline 5.0.2, equipped with Pilatus 6M detector. Data were processed using the HKL3000 program suite (83) or XDS (84).

The structure of *Tm*TsaC2 was determined by molecular replacement using Phenix Phaser (85) and an AlphaFold3 (78) model for search. Local remodeling of the linker region, ligand and solvent fitting, and structure refinement were done in Coot (86) and Refmac5 (87).

Table 2-1: X-ray data collection and structural refinement statistics.

Structure	***Tm*TsaC2/ Thr/ATP**	**TmTsaC2/ CT/ATP**	***Tm*TsaC2/ TC-AMP/ PPi**	***Tm*TsaC2/ CT/PPi**	***Tm*TsaC2 /Thr**
PDB ID	9DG5	9DSV	9DSQ	9D3H	9DSW
Ligands present in crystallization	10 mM L-threonine	10 mM threonine, 30 mM $NaHCO_3$.	10 mM L-threonine	10 mM each L-threonine, ATP and $MgCl_2$	10 mM L-threonine
Crystal soaking time with 10 mM each L-threonine, ATP and $MgCl_2$, 30 mM $NaHCO_3$.	10 min at pH 6.5.	30 min	60 min with pyrophosphatase.	90 min	N/A
Bound ligands	L-Threonine, ATP	Monomer A: CT, ATP. Monomer B: mixture of CT, ATP & TC-AMP,PPi.	TC-AMP, PPi	CT, PPi	L-Threonine
Data Collection					
Beamline, detector	SSRL BL14-1, Pilatus 3M	ALS BL5.0.2, Pilatus 6M	ALS BL5.0.2, Pilatus 6M	NSLSII 17-ID-1 AMX, Eiger 9M	SSRL BL14-1, Pilatus3 2M
Space group	$P3_121$				
Matthew's coefficient ($Å^3$/Da)	3.89	3.87	3.87	3.90	3.86
Solvent content (%)	68.4	68.1	68.3	68.5	68.2
Monomers/AU	2	2	2	2	2
Unit cell a=b, c (Å)	153.76, 87.21	153.59, 86.55	153.83, 86.89	154.04, 87.24	153.67. 86.73
Wavelength (Å)	1.19499	0.97741	1.00004	0.92010	1.19499
Resolution (Å)[1]	50.00-2.25 (2.29-2.25)	44.34-2.01 (2.05-2.01)	44.41-1.99 (2.03-1.99)	34.09-2.277 (2.317-2.277)	44.5-2.05 (2.09-2.05)
Measured reflections	1,110,952 (84,602)	1,242,956 (71,594)	1,509,843 (84,700)	697,037 (34,797)	1,282,439
Unique reflections	56,743 (2,809)	78,278 (4,436)	81,174 (4,420)	54,251 (2,696)	73,986 (3,656)

[1]Highest-resolution shell information in parentheses. [2] R_{free} was calculated with 5% of the data excluded from the refinement. CT: N-carboxy-L-threonine, TC-AMP: Threonylcarbamoyl adenylate.

Table 2-1: X-ray data collection and structural refinement statistics, continued.

Structure	***Tm*TsaC2/ Thr/ATP**	**TmTsaC2/ CT/ATP**	***Tm*TsaC2/ TC-AMP/ PPi**	***Tm*TsaC2/ CT/PPi**	***Tm*TsaC2 /Thr**
Completeness (%)	99.9 (100.0)	100.0 (100.0)	100.0 (100.0)	99.1 (100.0)	91.2
Multiplicity	19.6 (16.3)	15.9 (16.1)	18.6 (19.2)	12.8 (12.9)	
R-merge	0.503(2.799)	0.236 (3.912)	0.271 (5.124)	0.37(3.685)	0.24
R-meas	0.556 (1.806)	0.252 (4.175)	0.279 (5.263)	0.390 (3.836)	0.247
R-pim	0.124 (0.446)	0.063 (1.032)	0.064 (1.197)	0.108 (1.060)	0.04 (0.247)
$CC_{1/2}$	0.953(0.642)	0.998(0.308)	0.997(0.322)	0.994 (0.419)	0.999 (0.366)
$\langle I/\sigma(I) \rangle$	6.6 (1.3)	10.7 (0.8)	7.9 (0.7)	7.7 (1.1)	
Structure refinement					
Resolution range (Å)	44.43-2.25	44.34-2.01	44.41-1.99	34.09-2.28	44.40-2.05
No. of reflections (working/free)	45,571 / 2,356	74,298 / 3,941	76,961 / 4,176	51,476 / 2,724	64,297 (3,283)
No. of atoms in the asymmetric unit	5,550	5,656	5,553	5,672	5,434
Protein residues	645	646	646	671	646
Water	188	212	195	151	227
ATP	2	1	0	0	0
N-carboxy-L-threonine	0	1	0	2	0
TC-AMP	0	1	2	0	0
PPi	0	1	2	2	0
L-Threonine	2	0	0	0	2
Magnesium ions	2	2	2	2	0
No. of TLS bodies	2	1	2	2	2
R_{cryst}/R_{free}[2]	0.1849 / 0.2189	0.1945 / 0.2165	0.1909 / 0.2052	0.1887 / 0.2125	0.198 / 0.208
Deviation from ideality					
Bond length (Å)	0.008	0.004	0.004	0.009	0.009
Bond angles (°)	1.586	1.270	1.370	1.659	1.495
Ramachandran plot					
Favored & allowed (%)	99.51	99.16	99.33	99.7	99.8
Outliers (%)	0.49	0.84	0.67	0.3	0.2
Mean B factor (Å^2)	47.4	45.0	48.7	38.0	31.7

[1]Highest-resolution shell information in parentheses. [2] R_{free} was calculated with 5% of the data excluded from the refinement. CT: N-carboxy-L-threonine, TC-AMP: Threonylcarbamoyl adenylate.

2.2.2. Size-exclusion Chromatography-coupled Small-Angle X-ray Scattering analysis (SEC-SAXS)

SEC-SAXS data were collected on the SIBYLS beamline 12.3.1 at the Lawrence Berkeley National Laboratory's Advanced Light Source (ALS) (88, 89), using an incident beam wavelength (λ) set at 1.127 Å and a sample-to-detector distance of 2.1 m. This combination gives scattering vectors (q) ranging from 0.01 $Å^{-1}$ to 0.4 $Å^{-1}$, where $q = 4\pi\sin\theta/\lambda$ and 2θ is the measured scattering angle. Samples were injected on a Shodex 802.5 or 803 analytical SEC column in line with the X-ray beam and run using an Agilent 1260 Infinity HPLC system at a flow rate of 0.65 ml/min. For analysis of the apo enzyme, the sample contained 10 mg/ml (264 μM) *Tm*TsaC2, 30 mM KCl, 20 mM Tris pH 7.5 and 2 mM TCEP. For analysis of the enzyme in the presence of substrates, the sample additionally contained 1 mM L-threonine, 0.5 mM each ATP and $MgCl_2$, and 50 mM sodium bicarbonate. In each experiment, the SEC column was equilibrated and run with a buffer identical in composition to the corresponding sample buffer, including the presence or absence of substrates. The eluate was also subjected to in-line multiangle light scattering (MALS), quasi-elastic light scattering (QELS), UV absorption and refractive index analyses. MALS data were collected on an 18-angle DAWN HELEOS II light scattering detector connected to an Optilab refractive index concentration detector (Wyatt) and analyzed using the Wyatt Astra 8 software package. SAXS data were collected continuously using 2-second exposures per frame during a 25-min elution, and buffer scattering was subtracted from each frame before analysis. The data were processed in BioXTAS RAW (90). The radius of gyration (R_g) for each buffer-subtracted frame was calculated using the Guinier approximation $I(q) = I(0)\exp(-q^2R_g^2/3)$ with the limit $qRg < 1.3$. Sample homogeneity was confirmed by the uniform R_g values across the elution peak, complemented by the MALS, UV

and differential refractive index data. Final merged SAXS profiles, derived by integrating multiple frames at the elution peak, were used for further analysis. Pair distribution functions (P(*r*)) were calculated using the program GNOM (91). Porod volumes were calculated using PRIMUS in the ATSAS package (92). Molecular masses were determined using the methods Shape & Size (25) and SAXS- MoW 2.0 (93). Theoretical scattering curves were computed from various structural models and compared to the experimental scattering curves using the program FoXS (94). To fit SAXS data of *Tm*TsaC2 in the presence of substrates, a structural model derived directly from the Thr-bound crystal structure was used. To fit the SAXS data collected in the absence of substrates, the crystal structure was subjected to conformational sampling, covering 10,000 accessible conformations and followed by iterative multi-state model enumeration in MultiFoXs (94).

2.2.3. Initial velocity assays of various *Tm*TsaC2 mutants in the production of t^6A modified tRNA

Initial rates of t^6A-modified tRNA formation by wild-type and mutant *Tm*TsaC2 proteins were determined using 100 µL reactions. Reactions contained tri-buffer, pH 8.0, consisting of 80 mM MES, 80 mM HEPES, and 160 mM diethanolamine, supplemented with 300 mM KCl, 5 mM DTT, 5 mM $NaHCO_3$, 20 mM $MgCl_2$, 2 mM ATP, 250 µM L-[U-^{14}C]-threonine (17.5 µCi/µmol), 20 µM *Tm*$tRNA^{Thr}CGU$ *in vitro* transcript, 2.5 µM TCT complex, and 0.1 µM wild-type or mutant *Tm*TsaC2. Reactions were started by adding ATP and L-threonine and incubated at 60°C. Aliquots of 30 µL were collected after 5, 10, and 15 min and quenched in 300 µL cold 10% TCA. After incubation on ice for at least 15 min, precipitated tRNA was captured on Whatman GF/C filters. Reaction tubes were washed three times with cold 10% TCA, and filters were washed with cold 10% TCA followed by cold 95% ethanol. Dried filters were placed in 5 mL Econo-safe liquid scintillation cocktail, and radioactivity was measured using a Beckman LS

6500 multi-purpose scintillation counter. Assays were performed in duplicate across three independent trials.

2.3. Results

2.3.1. Time-course crystal soaking captures sequential steps of the TsaC2-catalyzed reaction and provides direct evidence of the reaction intermediate N-carboxy-L-threonine.

I conducted a series of timed soaking experiments in which *Tm*TsaC2 crystals, grown in the presence of L-Threonine, were soaked for increasing periods of time in buffer containing all reaction substrates: L-Threonine, sodium bicarbonate, and Mg-ATP. These experiments yielded five *Tm*TsaC2 crystal structures, at resolutions of 1.99-2.28 Å, with unambiguous density for reaction substrates, an intermediate and products (Fig. 2-2A, B). The structures are referred to here as *Tm*TsaC2/Thr, *Tm*TsaC2/Thr/ATP, *Tm*TsaC2/CT/ATP, *Tm*TsaC2/TC-AMP/PPi, and *Tm*TsaC2/CT/PPi, corresponding to structures bound to L-threonine, L-threonine/ATP, N-carboxy-L-threonine/ATP, TC-AMP/pyrophosphate, and N-carboxy-L-threonine/pyrophosphate, respectively (Table 2-1). The crystal asymmetric unit contains two *Tm*TsaC2 monomers, A and B, which exhibit identical structures and can be superimposed with an r.m.s.d. of 0.3 Å over 335 C_α atoms. In all structures except *Tm*TsaC2/CT/ATP, both monomers contain the same ligands. In *Tm*TsaC2/CT/ATP, the active site of monomer A is occupied by N-carboxy-L-threonine and ATP, whereas monomer B exhibits a mixture of two states, one bound to N-carboxy-L-threonine/ATP and the other bound to TC-AMP/pyrophosphate.

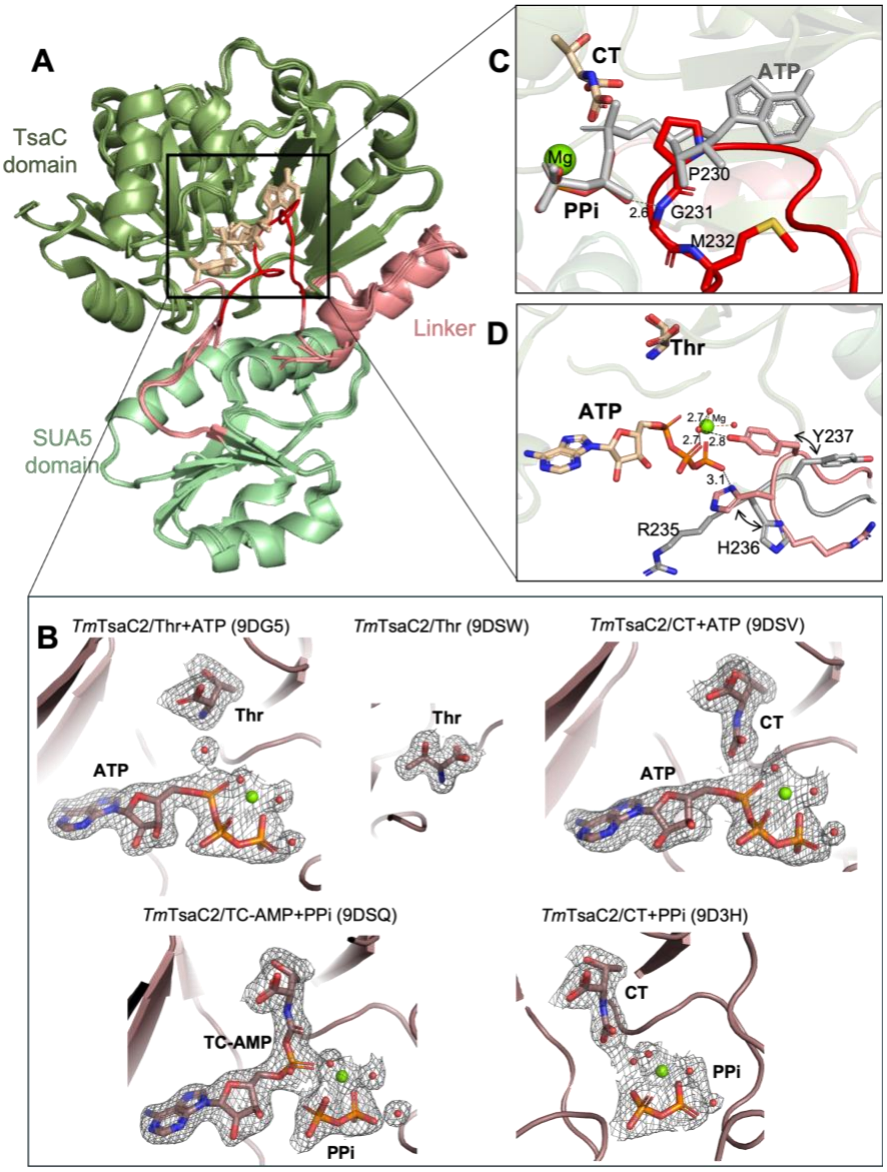

Figure 2-2: *Tm*TsaC2 structures.
A) Superposition of all structures. The catalytic domain is shown in dark green, the SUA5 domain in light green, the linker region in salmon, the linker loop found ordered only in *Tm*TsaC2/CT/PPi in red, and the ligands in wheat. **B)** 2Fo-Fc map around the bound ligands in the different structures, contoured at 1.0 σ. PDB IDs are shown in parentheses. CT is N-carboxy-L-threonine. **C)** The active site of *Tm*TsaC2/CT/PPi structure showing the ordered linker loop (red). Superposed on this figure is the Mg-ATP molecule bound in the active site of the *Tm*TsaC2/Thr/ATP structure. The superposition highlights that in the absence of nucleotide, the tip of the linker loop inserts into the active site, with Pro230 occupying the binding site of the ATP ribose. **D)** Orientation of linker residues 235-237 as seen in the *Tm*TsaC2/Thr/ATP structure (in color), versus in the *Tm*TsaC2/Thr structure (gray), highlighting conformational changes associated with Mg-ATP binding.

Overall, the *Tm*TsaC2 structures are similar to TsaC2/Sua5 structures from *S. tokodaii* and *P. abyssi* (PDB IDs 6F8Y and 6F87, respectively). Structural superposition of the three enzymes yields r.m.s.d. values of 0.69-1.1Å. Structure-based alignment of the three enzymes shows overall sequence identities of 43%, 42% and 20% in their N-terminal domains, linker regions and SUA5 domains, respectively (Supplementary Fig. 2-1).

In *Tm*TsaC2, the catalytic N-terminal domain is composed of nine β-strands and seven α-helices folded into a compact α/β twisted open-sheet structure, whereas the SUA5 domain adopts a Rossmann fold consisting of a central five-stranded β-sheet surrounded by three α-helices. The two domains are connected by a flexible linker comprising residues Pro199-Pro242.

Although all *Tm*TsaC2 structures are highly similar overall, differences are observed in the linker region (Fig. 2-2C and D). In all structures except *Tm*TsaC2/CT/PPi, the linker loop comprising residues 223-235 is disordered and lacks interpretable density, similar to the corresponding loop in the TC-AMP-bound *St*Sua5 structure (residues 215-233 in *S. tokodaii* numbers, PDB ID 4E1B). In the *Tm*TsaC2/CT/PPi structure, the loop is ordered, with its highly conserved Pro230-Gly231-Met232 motif at its tip inserted into the active site. Pro230 sits in the position otherwise occupied by the ribose of ATP or TC-AMP, and the backbone nitrogen of Gly231 forms a hydrogen bond with a pyrophosphate oxygen atom. This linker arrangement was previously observed in the *Pa*Sua5 structure bound to L-threonine/PPi or L-threonine alone, where triple mutation of the PGM motif to alanine significantly reduced t^6A and ATPase activity (82). Intriguingly, the linker is not ordered in my L-threonine-bound structure.

In *Tm*TsaC2 structures, linker residues Arg235, His 236 and Tyr237 change their orientations in response to ligand binding (Fig. 2-2D). When only L-threonine is bound, these residues face away from the active site. Upon binding ATP or PPi, a rotation of the polypeptide

backbone reorients both residues toward the active site. In this conformation, His236 forms a hydrogen bond with a γ-phosphate oxygen atom, whereas Tyr237 forms a water-mediated hydrogen bond with the β-phosphate of ATP or with PPi. Consistent with the importance of this interaction, the *Tm*TsaC2^{Y237A} mutant is essentially inactive in the t^6A synthesis assay (Fig. 2-3E). This trend is not observed in the Thr-bound and Thr/PPi-bound *Pa*Sua5 structures where the corresponding His234 and Tyr235 face the active site in both structures. In the absence of bound PPi, His234 instead interacts with one of two water molecules occupying the PPi binding site.

All other ligand interactions are mediated by conserved residues of the N-terminal domain of *Tm*TsaC2 (Fig. 2-3). Alanine substitutions of ligand binding residues either abolish or significantly reduces t^6A activity (Fig. 2-3D, E). Unlike the linker, this domain is relatively rigid, and the positions of active-site residues do not change significantly between the different structures. All protein-ligand interactions are summarized in the Table 2-2.

The *Tm*TsaC2/Thr-ATP structure is the first TsaC2/Sua5 structure in which the true ATP substrate, as opposed to a non-hydrolyzable analog, is bound. (Fig. 2-3A). In this structure, L-threonine interacts with five conserved residues and a water molecule located at the position where the CO_2/HCO_3^- substrate is likely to bind during the reaction. The side-chain hydroxyl group of threonine hydrogen bonds with His68 and Arg122, while the backbone carboxylate moiety forms a network of hydrogen bonds with Thr36, Ser182 and Arg196. Arg196 also interacts with the 5′-O of ATP. The ATP phosphate groups engage the side chains of Arg59, Ser144, Lys57, Ser148, Gly149, His236 and Asn63. In addition, Asn63 forms a hydrogen bond via its side chain O with the 3′-OH of the ribose. The adenine base is inserted into a conserved hydrophobic pocket (shown for TC-AMP in Fig. 2-3C) and forms a single hydrogen bond via its exocyclic amino group with Thr118.

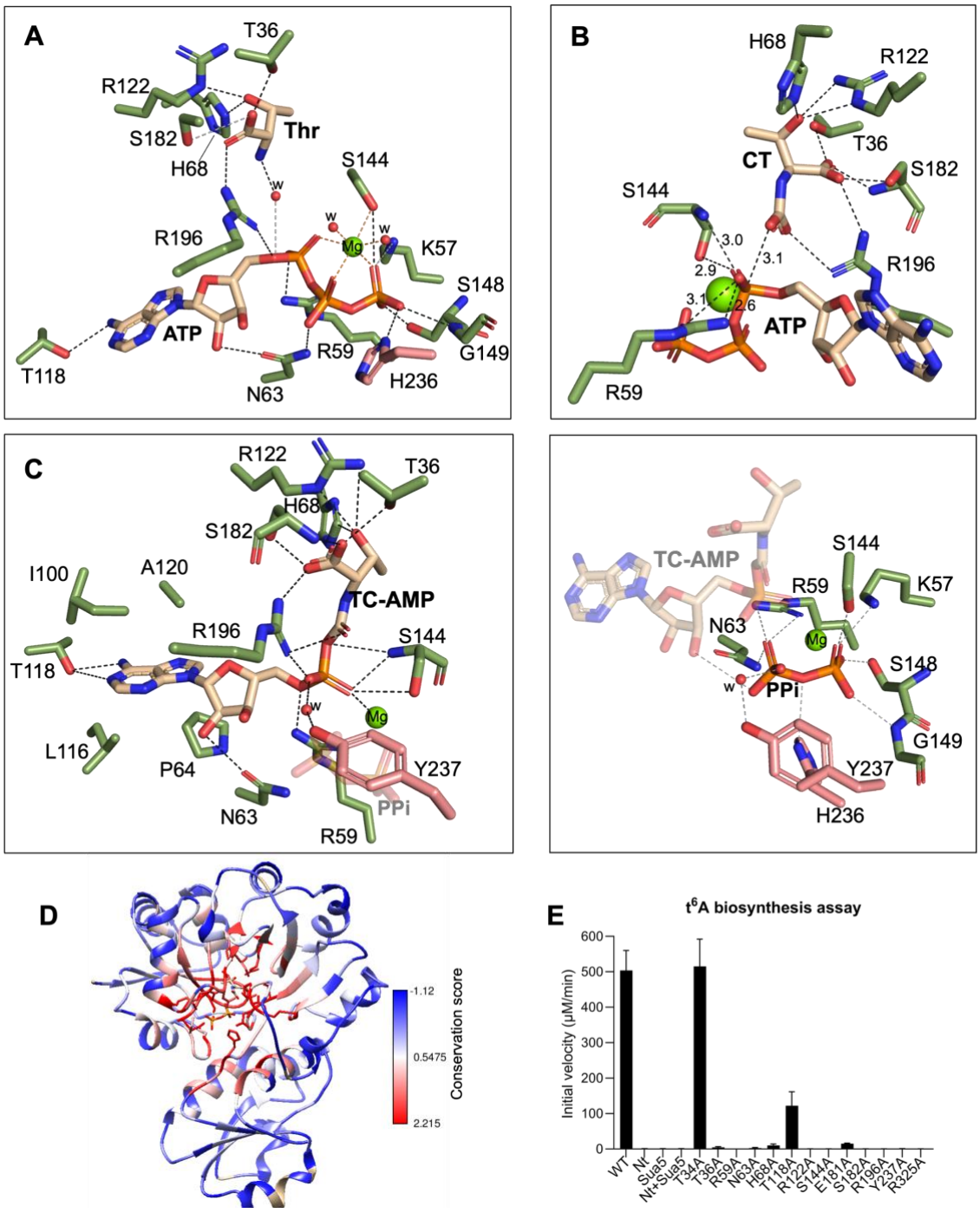

Figure 2-3: TsaC2 interactions with the substrates, intermediate and products.
A-C: *Tm*TsaC2 interactions with **A)** substrates ATP and L-threonine, **B)** intermediate N-carboxy-L-threonine and ATP, **C)** products TC-AMP (left) and PPi (right). Distances 3.3Å or less are shown as dashed lines. **D)** Conservation of residues in *Tm*TsaC2. **E)** Initial velocity measured for *Tm*TsaC2 mutants and constructs in the t^6A biosynthesis assay. *Tm*TsaC2^{Nt} is the N-terminal domain (residues 2-221), *Tm*TsaC2^{SUA5} is the SUA5 domain (residues 222-335).

The conformation and interactions of ATP in my structure differ from those previously observed for AMPPNP bound to *St*Sua5 (Supplementary Fig. 2-2A-C). In the *St*Sua5 structure (PDB ID 3AJE), due to rotation of the triphosphate moiety relative to the ribose, Asn63 coordinates the ribose 2′-OH and does not engage the α-phosphate. Lys57 and His236 are far removed from the nucleotide binding site and do not make any contacts with it. Instead, Tyr237 makes a direct hydrogen bond with the β-phosphate, and Glu181 is positioned only 2.4 Å away from the γ-phosphate, which appears highly unusual unless it is protonated. This structure likely does not accurately represent the substrate-binding mode, as the γ-phosphate lacks 2Fo-Fc density and strong negative Fo-Fc density is observed even at contour level of 5 (Supplementary Fig. 2-2D). Additionally, AMPPNP is not coordinated to a metal ion.

Most of the enzyme-ligand interactions observed in the Thr/ATP-bound structure are also present in the other liganded *Tm*TsaC2 structures (Fig. 2-3B and C). In addition to its role in coordinating the L-Thr and ATP substrates, Arg196 also coordinates the C=O moiety of the N-carboxy-L-threonine intermediate and of TC-AMP in the *Tm*TsaC2/CT/ATP and *Tm*TsaC2/TC-AMP/PPi structures, respectively. This suggests that Arg196 also engages CO_2/HCO_3^- during the reaction, explaining why enzyme activity is completely abolished in the *Tm*TsaC2^{R196A} mutant (Fig. 2-3E).

The *Tm*TsaC2/CT/ATP structure provides the first direct evidence of the proposed reaction intermediate N-carboxy-L-threonine, and offers insight into this stage of the reaction. Intriguingly, only monomer A in the crystal is bound to N-carboxy-L-threonine and ATP, whereas monomer B contains a mixture of N-carboxy-L-threonine/ATP (the intermediate-bound state) and TC-AMP/PPi (the products-bound state). In monomer A, the negative charge of the ATP α-phosphate is stabilized by interactions with the Arg59 side chain, hydrogen bonds with

the Ser144 side chain and backbone, and coordination by the magnesium cation. One carbamate oxygen of N-carboxy-L-threonine forms a salt bridge with Arg196, while the other one is 3.1 Å from the α-phosphorus atom of ATP, which appears to be in a favorable position for nucleophilic attack. It is unclear how the reaction is fully trapped at the intermediate stage in monomer A. Possibly, local crystal packing constrains the conformational flexibility of monomer A, thereby slowing down the reaction.

The *Tm*TsaC2/CT/PPi structure also contains N-carboxy-L-threonine, but with pyrophosphate, instead of ATP. This structure was obtained from the longest crystal soak, 90 minutes. As reported previously, TC-AMP degrades in solution into AMP and equivalent amounts of L-threonine or oxazolidinone, a dehydrated and cyclized form of N-carboxy-L-threonine (42). It is possible that after long soak, TC-AMP degraded and AMP was released into solution, while CT and PPi stayed bound in the active site.

2.3.2. SEC-SAXS reveals substrate-induced closure of *Tm*TsaC2.

To examine how substrates affect *Tm*TsaC2 structure and dynamics, SEC-SAXS was performed in the absence and presence of the following substrates in the mobile phase: 1 mM L-threonine, 0.5 mM ATP, 0.5 mM magnesium chloride and 50 mM sodium bicarbonate (Fig. 2-4A, B). Structural parameters derived from the SAXS data are summarized in Table 2-3. In the absence of substrates, the crystal structure, referred to as the 'closed model', gave a relatively poor fit to the SAXS data ($\chi^2 = 3.20$). To improve the fit, the MultiFoXs program was used to identify the appropriate conformation by subjecting the crystal structure to conformational sampling while allowing flexibility in the linker region (94). This generated an open model in which the SUA5 domain and linker peptide are positioned away from the active site. The fit improved to χ^2=1.45. However, the best fit was obtained from a multi-state model in which 74%

of protein population adopts the open conformation and only 26% is in the closed conformation (χ^2 = 1.19). This suggests that *Tm*TsaC2 is conformationally flexible in solution in the absence of ligands. In contrast, in the SEC-SAXS experiment conducted in the presence of the substrates, the best fit to the SAXS data was obtained using the closed model alone (χ^2 = 1.14), or a multi-state model where 94% of the protein population adopts the closed conformation (χ^2 = 1.11).

Overall, these results show that *Tm*TsaC2 is conformationally flexible in solution in the absence of substrates. Once substrates bind and the reaction begins, the protein assumes the closed, compact conformation observed in the crystal structures. This is consistent with the observation that crystals could not be obtained without at least threonine being present in the crystallization buffer.

Previous enzymatic studies established that the SUA5 domain is required for catalysis in *Tm*TsaC2 (Fig. 2-4C) (unpublished data). Studies on *Pa*Sua5 also provided evidence that some linker residues contribute to catalytic activity (82). Arg325 is the most conserved residue in the SUA5 domain of *Tm*TsaC2, and this basic residue forms a salt bridge with Glu181 in the catalytic domain (Fig. 2-4D). Although neither residue interacts with any of the substrates, their alanine substitutions result in loss of t^6A synthesis activity (Fig. 2.4C), suggesting a role for the salt bridge in stabilizing a catalytically productive protein conformation. This could explain why these residues are essential for catalysis.

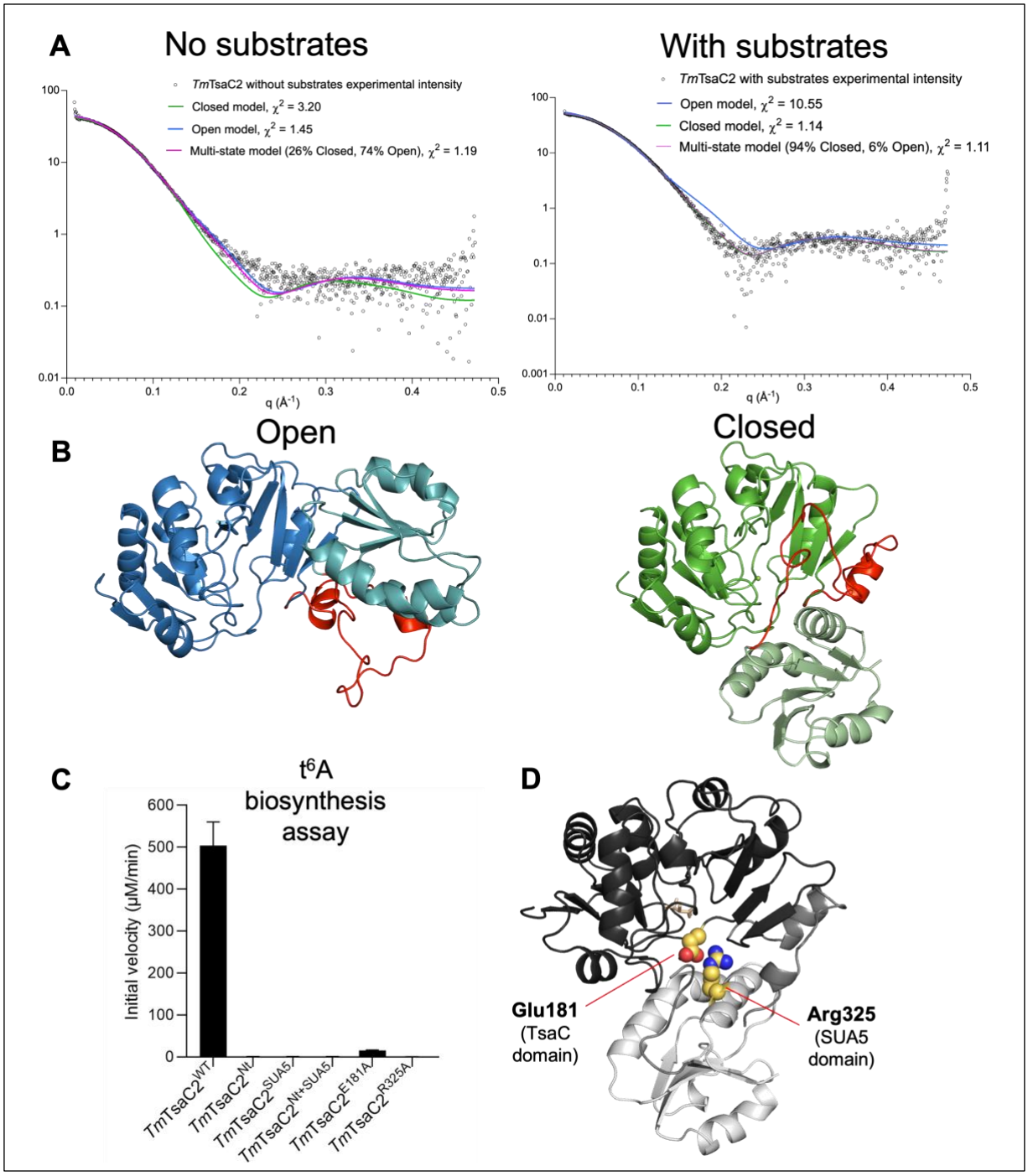

Figure 2-4: Conformational flexibility of *Tm*TsaC2 in solution as revealed by SEC-SAXS analysis.
A) Comparison of the experimental SAXS intensity (black circles) with theoretical scattering curves calculated from various structural models (colored lines) for the apo enzyme (left) and for the enzyme in the presence of all substrates (right). **B)** The open (left) and closed (right) structural models used for fitting the SAXS data. **C)** t^6A biosynthesis assay for related *Tm*TsaC2 constructs and mutants. *Tm*TsaC2^{Nt} is N-terminal domain (residues 2-221), *Tm*TsaC2^{SUA5} is the SUA5 domain (residues 222-335). **D)** Location of the E181-R325 salt bridge in *Tm*TsaC2.

Table 2-2: Interactions between specific *Tm*TsaC2 residues and bound ligands.

Residues in *Tm*TsaC2: interacting ligand	**Interactions with the ligands and distances(Å)**				**% Conservation in TsaC2s**	**Ala mutant t^6A activity (% relative to wild type)**
	Thr+ATP	CT+ATP	TC-AMP +PPi	CT+PPi		
Thr36-OH: Thr/Thr moiety in CT or TC-AMP	Carboxyl **O1**	Carboxyl **O1**	Carboxyl **O1**	Carboxyl **O1**	100	0.9
Lys57-NZ: ATP/PPi	γP**O1**	γP**O1**, γP**O2**	P2-**O1**, P2-**O2**	P2-**O1**, P2-**O2**	100	-
Arg59-NH1: ATP/TC-AMP/ PPi	αP**O2**	αP**O2**	P**O3** (TC-AMP), P1-**O3** (PPi)	P1-**O3**	100	0.2
Arg59-NH2: ATP/PPi	αP-**O**-βP, γP**O2**	αP-**O**-βP, γP**O2**	P1-**O3** P2-**O2**	P1-**O3** P2-**O2**		
Asn63-ND2: ATP/PPi	β-P**O2**	β-P**O2**	P1-**O2**	P1-**O2**	99.8 (0.2% Asp)	0.5
Asn63-OD1: ATP/TC-AMP	Ribose 2′-O**H**	Ribose 2′-O**H**	Ribose 2′-O**H**	water		
His68-NE2: Thr/ Thr moiety in CT or TC-AMP	Hydroxyl **-OH**	Hydroxyl **-OH**	Hydroxyl **-OH**	Hydroxyl **-OH**	99.8 (0.2% Thr)	2
T118-OH: ATP/TC-AMP	**N6** of adenine	**N6** of adenine	**N6** of adenine	-	83.5 (13.8% Ser)	24
Arg122 - NE&NH2: Thr/ Thr moiety in CT or TC-AMP	Hydroxyl **-O**H	Hydroxyl **-O**H	Hydroxyl-**O**H	Hydroxyl **-O**H	100	0.1

* Interacting atoms from ligands are bolded. CT is N-carboxy-L-threonine. Relative positions of Pyrophosphate P1 and P2 in TsaC2 correspond to positions of ATP β-phosphate and γ-phosphate, respectively. Conservation of protein residues and the effects of alanine mutations on t^6A biosynthesis are shown in the right columns.

Table 2-2: Interactions between specific *Tm*TsaC2 residues and bound ligands, continued.

Residues in *Tm*TsaC2: interacting ligand	**Interactions with the ligands and distances(Å)**				**% Conservation in TsaC2s**	**Ala mutant t^6A activity (% relative to wild type)**
	Thr+ATP	CT+ATP	TC-AMP +PPi	CT+PPi		
Ser144-OH: Mg&ATP/PPi	Mg, αP**O1**, γP**O1**	Mg, αP**O1**, γP**O1**	Mg, P2-**O1** (PPi), P**O1** (TC-AMP)	Mg, P2-**O1**	100	0.1
Ser144-NH: ATP/TC-AMP	αP**O1**	αP**O1**	P**O1**, C-**O**-P	-		
Ser148-OH: ATP/PPi	γP**O2**	γP**O2**	P2-**O2**	P2-**O2**	94.8 (4.7% Ala)	-
Gly149-NH: ATP/PPi	γP**O2**	γP**O2**	P2-**O3**	P2-**O3**	97.3 (2.4% Thr)	-
Ser182-OH: Thr/ Thr moiety in CT or TC-AMP	Carboxyl **O1**	Carboxyl **O1**	Carboxyl **O1**	Carboxyl **O1**	100	0.1
Ser182-NH: Thr/ Thr moiety in CT or TC-AMP	Carboxyl **O2**	Carboxyl **O2**	Carboxyl **O2**	Carboxyl **O2**		
Arg196-NH1: Thr/ Thr moiety in CT or TC-AMP	Carboxyl **O2**	Carboxyl **O2**	Carboxyl **O2**	Carboxyl **O2**	100	0.08
Arg196-NH2: ATP/TC-AMP & CT	Ribose 5′-**O**	ribose 5′-**O** carbamate **O**	ribose 5′-**O,** Carbamoyl **O**	carbamate **O**		
Gly231-NH: PPi	-			P1-**O2**	100	-
His236-NE2: ATP/PPi	β-P**O2**	β-P**O2** βP-**O**-γP	P1-**O2,** P1-**O**-P2	P1-**O2**, P1-**O**-P2	100	-
Tyr237-OH: water	H-bonds with water that interacts with βPO4/P2-O4 and magnesium coordinating water				100	1

* Interacting atoms from ligands are bolded. CT is N-carboxy-L-threonine. Relative positions of Pyrophosphate P1 and P2 in TsaC2 correspond to positions of ATP β-phosphate and γ-phosphate, respectively. Conservation of protein residues and the effects of alanine mutations on t^6A biosynthesis are shown in the right columns.

Table 2-3: Parameters calculated from SAXS and MALS data of *Tm*TsaC2 in the absence and presence of substrates.

	Apo enzyme	**With all substrates**
Structural parameters		
Porod volume, Vp ($Å^3$)	44,689	39,939
R_g from Guinier plot (Å)	21.86 ± 0.29	21.2 ± 0.14
R_g from P(r) (Å)	22.28 ± 0.05	21.35 ± 0.04
D_{max} from GNOM (Å)	69	69
Molecular mass (kDa)		
MALS [b]	47.9	38.5
Theoretical from sequence	38.3	

2.4. Discussion

2.4.1. Proposal for the TsaC2-catalyzed reaction mechanism

The *Tm*TsaC2/TC-ATP structure provides the first direct evidence for the reaction intermediate, N-carboxy-L-threonine. In this structure, one carbamate oxygen is stabilized by Arg196, while the other is positioned near the ATP α-phosphorus, consistent with a favorable geometry for nucleophilic attack. Thus, this structure supports the previously proposed reaction mechanism in which N-carboxy-L-threonine is formed from L-threonine and CO_2, which subsequently attacks ATP to generate TC-AMP and pyrophosphate (42).

In the first step of this proposed mechanism, L-threonine must react with CO_2 to form N-carboxy-L-threonine. Free L-threonine exists predominantly as a zwitterion, with a protonated amino group; therefore, its amino group must be deprotonated or otherwise activated before it can act as an efficient nucleophile. The *Tm*TsaC2/Thr-ATP structure suggests a possible route

for this activation. A water molecule located at the position proposed to be occupied by CO_2/HCO_3^- hydrogen bonds with the threonine amino group and lies 3.2 Å from the ATP 5′ oxygen. By donating a hydrogen bond to ATP, this water molecule may be positioned favorably to accept a proton from L-threonine, either directly or as part of a broader proton-transfer network that promotes threonine activation. Alternatively, His68 or Glu181 could contribute to proton transfer, although both residues are positioned approximately 4–6 Å from the threonine amino group in the observed structures and would require either conformational adjustment or involvement of an intervening water.

The second reactant in this step is likely CO_2 rather than bicarbonate. CO_2 is a better electrophile than bicarbonate and can react directly with the threonine amino group without requiring loss of a hydroxide group. In contrast, direct reaction with bicarbonate would require a less favorable substitution process. This proposed first step is chemically plausible, as amino acids, including threonine, have been shown to react with CO_2 to form carbamates in solution; however, such reactions generally require high amino acid concentrations and alkaline pH values of approximately 8.5–12 (42, 95). Therefore, the role of TsaC2 may be to make this chemistry favorable under physiological conditions by concentrating L-threonine and CO_2 in the active site and creating an environment that promotes deprotonation of the threonine amino group.

Once N-carboxy-L-threonine is formed, the active site appears preorganized for reaction with ATP. In the *Tm*TsaC2/CT-ATP structure, one carbamate oxygen is stabilized by Arg196, while the ATP α-phosphate is stabilized by multiple electrostatic and hydrogen-bonding interactions with Arg59, Ser144, and the magnesium ion. These interactions likely increase the electrophilicity of the α-phosphorus and position ATP for attack by the carbamate oxygen of N-carboxy-L-threonine. The observed distance between the carbamate oxygen and the α-phosphorus

is consistent with a catalytically competent arrangement. Thus, formation of N-carboxy-L-threonine places the reactive carbamate oxygen in position to attack ATP, ultimately, resulting in formation of TC-AMP and pyrophosphate.

2.4.2. Role of the linker and SUA5 domain in TsaC2 catalysis

The data presented here, together with previously published studies, show that alanine substitution of His236, Tyr237, or the PGM motif compromises t^6A activity (82). Our structures provide a structural explanation for these effects. His236 directly engages ATP or pyrophosphate, while Tyr237 contributes indirectly by stabilizing a water molecule that bridges the ligand and the surrounding active-site environment. In the absence of ATP, the linker can become ordered, allowing the conserved P230-G231-M232 motif to insert into the active site and enabling the backbone nitrogen of Gly231 to interact with pyrophosphate. Thus, at least part of the linker appears to contribute directly to ligand binding and stabilization.

The linker may also have broader roles in regulating active-site dynamics. Because the linker changes conformation depending on the ligand state, it could help control substrate access, product release, or stabilization of specific catalytic states. However, the data presented here do not directly establish such regulatory functions. Therefore, this possibility remains speculative and will require additional experiments to test whether linker movement affects ligand exchange or product release during catalysis.

The role of the SUA5 domain is less direct but appears to be essential for organizing the catalytically competent state of TsaC2. Unlike the catalytic N-terminal domain, the SUA5 domain contains few conserved residues. The most conserved residue is Arg325, which forms an interdomain salt bridge with Glu181. Mutation of either residue abolishes catalytic activity, even though neither Glu181 nor Arg325 directly contacts the substrates. A second interdomain salt

bridge, formed between Arg298 and Asp162, may also help stabilize the protein, as alanine mutation of the corresponding arginine significantly reduced t^6A activity in *Pa*Sua5 (82). Together, these observations suggest that interdomain contacts, rather than direct substrate interactions, are critical for SUA5-dependent catalysis.

Our SEC-SAXS data provide a possible explanation for this requirement. In the absence of substrates, *Tm*TsaC2 samples open conformations in which the SUA5 domain is positioned away from the catalytic domain. In the presence of reaction substrates, however, the enzyme predominantly adopts a closed conformation similar to that observed in the crystal structures. This closed conformation is likely stabilized, at least in part, by the Glu181–Arg325 and Asp162-Arg298 salt bridges. The key question is why this closed conformation is favored during catalysis. One possibility is that this closed conformation positions the flexible linker near the active site, allowing His236, Tyr237, and the PGM motif to participate in ligand binding and stabilization. Thus, the essential role of the SUA5 domain may be to organize the architecture of TsaC2 during the reaction. By stabilizing the closed state, the SUA5 domain may help position the linker and maintain an active-site environment competent for TC-AMP formation. This hypothesis provides an explanation for why mutations in interdomain salt bridges abolish activity despite the absence of direct ligand contacts by the SUA5 domain.

2.4.3. Possible differences between TsaC and TsaC2

The structures presented here can also help interpret previously observed biochemical differences between TsaC and TsaC2 enzymes. Lauhon showed that *E. coli* TsaC and *B. subtilis* TsaC2 behave differently when supplied with L-threonine, bicarbonate, and ATP. Under these conditions, TsaC continuously synthesizes TC-AMP, whereas TsaC2 initially produces TC-AMP but releases a larger amount of AMP in the absence of inorganic pyrophosphatase. Addition of

pyrophosphatase restores TC-AMP production by TsaC2, making its behavior more similar to that of *E. coli* TsaC.

Our structures support the idea that AMP formation is unlikely to be a required step in the TsaC2-catalyzed reaction. Therefore, the excess AMP observed in TsaC2 reactions is more likely to arise from subsequent TC-AMP degradation or hydrolysis rather than from the main catalytic pathway. This interpretation is consistent with the *Tm*TsaC2/CT-PPi structure, which contains N-carboxy-L-threonine and pyrophosphate after the longest crystal soak. One possible explanation is that TC-AMP formed in the active site degraded during the extended soak, releasing AMP into solution while N-carboxy-L-threonine and PPi remained bound. In this state, the linker becomes ordered and inserts into the active site, with Pro230 occupying the ribose-binding position and Gly231 interacting with pyrophosphate. This arrangement may stabilize the CT/PPi-bound state after AMP release.

The question then becomes why this behavior is more pronounced for TsaC2 than for TsaC. The *Tm*TsaC2 structures show that ATP, PPi, and the associated magnesium ion are surrounded by a water network stabilized by TsaC2-specific residues, including Glu181, Ser152, and Tyr237 (Supplementary Fig. 2-3). These residues likely help organize water molecules around ATP/PPi and magnesium. Because ligand-bound structures of TsaC are not available, I generated an AlphaFold3 model of *E. coli* TsaC bound to ATP to account for ligand-induced conformational changes. This model suggests that TsaC lacks several of the interactions observed in TsaC2: Tyr237 is absent, and Glu181 and Ser152 are replaced by proline residues, which cannot stabilize the water network in the same way.

These differences may explain why TsaC2 is more sensitive to PPi accumulation. In the absence of pyrophosphatase, elevated PPi levels may favor retention of PPi and magnesium in

the TsaC2 active site. Retained magnesium and associated water molecules could facilitate TC-AMP hydrolysis, producing AMP and N-carboxy-L-threonine. This is consistent with the observation that increased magnesium concentration promotes TC-AMP degradation in solution (35). After AMP release, the linker may adopt the ordered conformation observed in the *Tm*TsaC2/TC-PPi structure. When pyrophosphatase is present, PPi would be depleted from solution, reducing stabilization of this state and allowing TsaC2 to behave more like TsaC.

Thus, the apparent difference between TsaC and TsaC2 may not reflect a fundamentally different chemical route to TC-AMP formation. Instead, both enzymes may form TC-AMP through N-carboxy-L-threonine, while TsaC2-specific linker and SUA5-associated interactions alter the fate of TC-AMP after it is formed. In particular, TsaC2 may be more prone to trapping PPi- and magnesium-bound states that promote TC-AMP degradation and AMP release under *in vitro* conditions. However, it remains unclear whether this behavior has biological relevance or instead reflects nonphysiological accumulation of PPi during *in vitro* reactions.

2.5. Supplementary figures

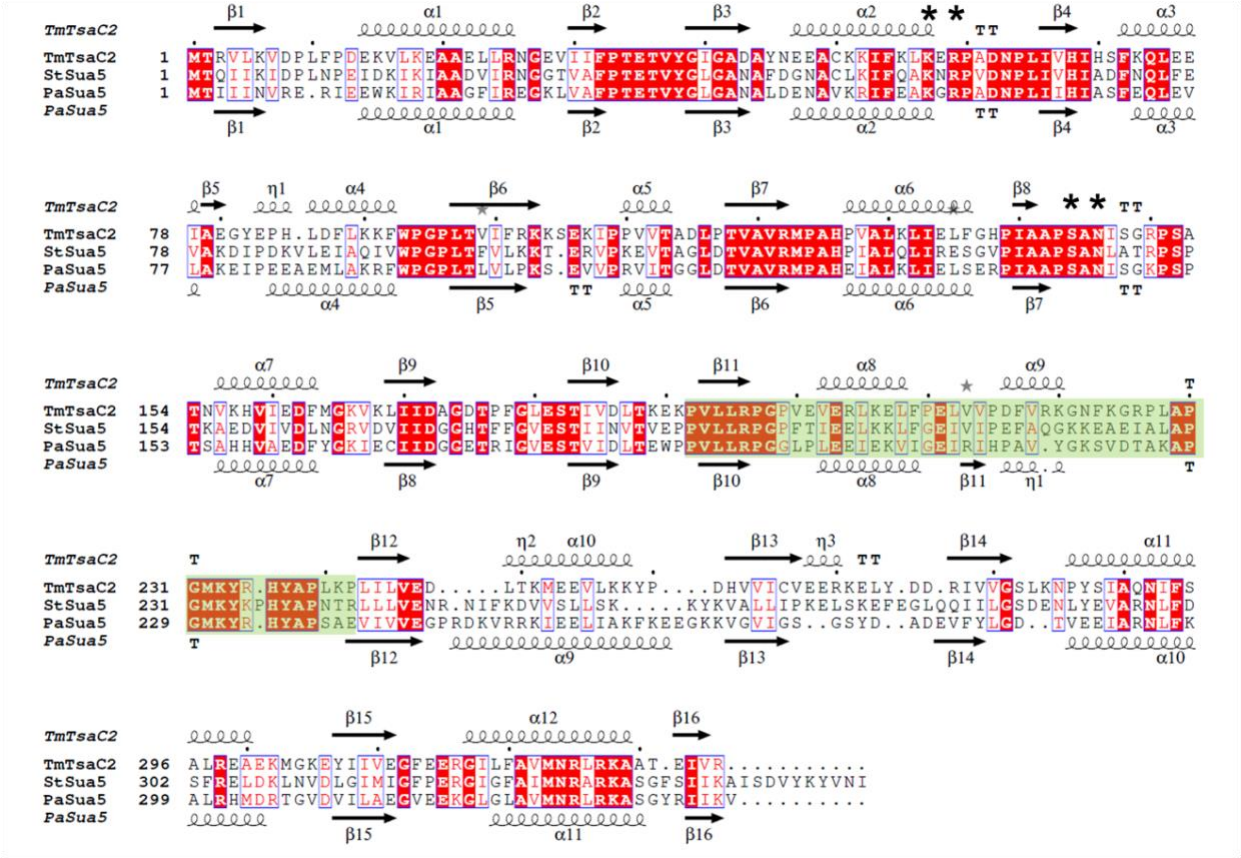

Supplementary figure 2-1: Structure-based multisequence alignment of characterized TsaC2/Sua5 enzymes.
Conserved residues are highlighted in red. The linker region is shaded in green. The KxR/SxN tetrad is marked with asterisks. Secondary structure elements derived from the crystal structures of *Tm*TsaC2 and *Pa*Sua5 are shown above and below the sequences, respectively. *Tm*, *Thermotoga maritima; St*, *Sulfolobus tokodaii*; *Pa*, *Pyrococcus abyssi.*

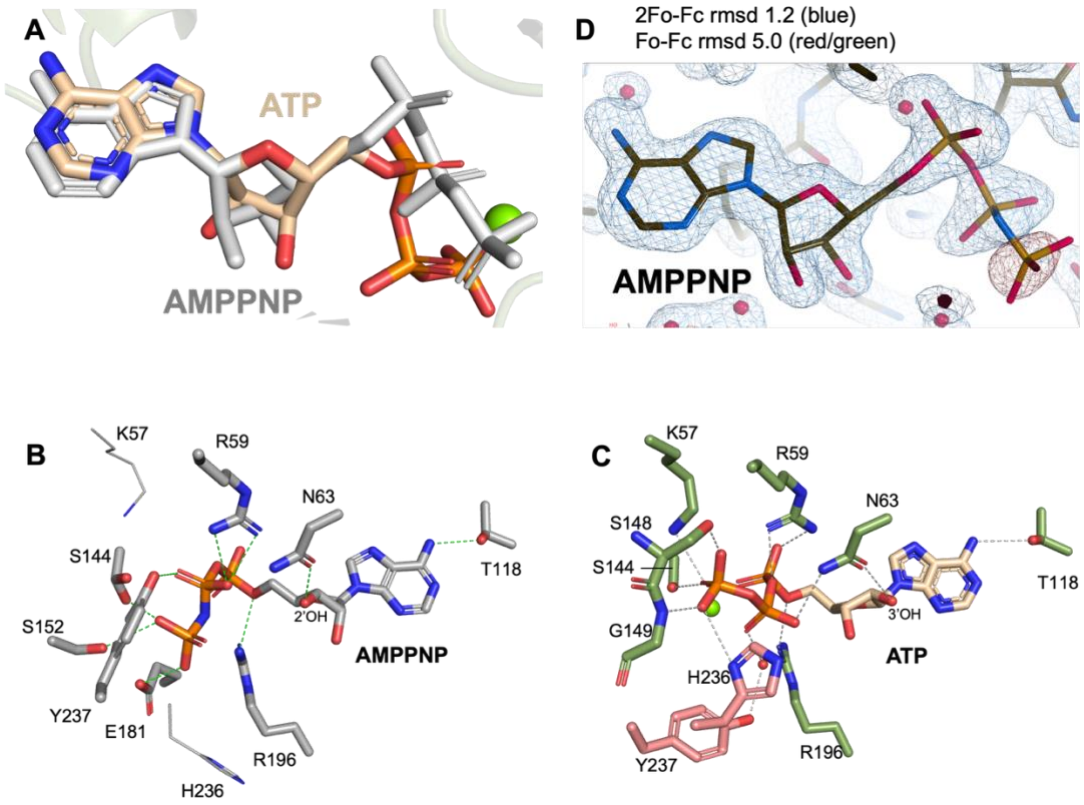

Supplementary figure 2-2: A) Comparison of ATP (in color) and AMPPNP (in gray) conformations in *Tm*TsaC2 and *St*Sua5 active sites, respectively (PDB ID: 3AJE). **B)** Interaction with AMPPNP in *St*Sua5 structure**. C)** Interactions with ATP in *Tm*TsaC2 structure. **D)** Electron density for AMPPNP in *St*Sua5 structure.

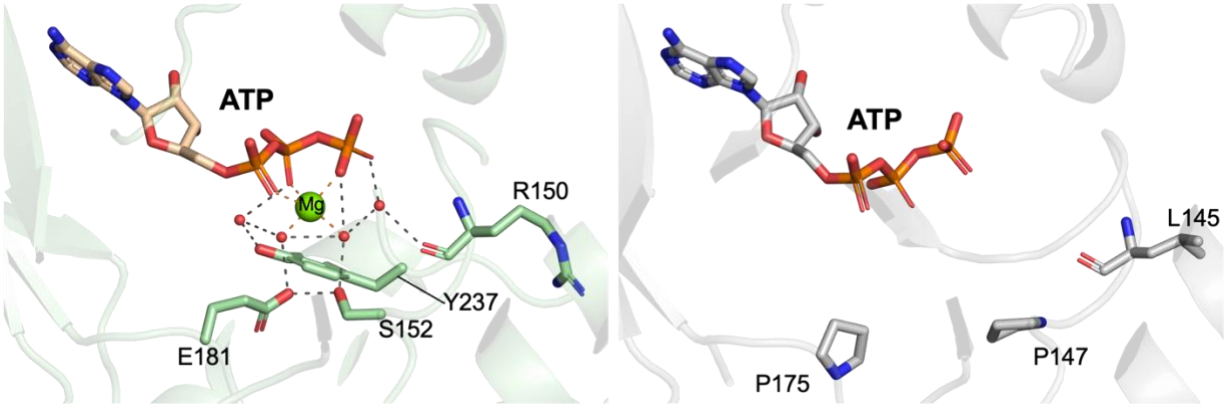

Supplementary figure 2-3: Water network around ATP and magnesium in *Tm*TsaC2 (left) and corresponding residues in *E.coli* TsaC (AlphaFold3 model of *E.coli* TsaC bound to ATP).

2.6. Acknowledgements

Chapter 2, in part is currently being prepared for submission for publication of the material. Kutchuashvili, A., Wood, E., Scheleen, E., Luthra, A., Sankaran, B., Iwata-Reuyl, D., Swairjo, M.A. “Structure–Function Analysis of the *Thermotoga maritima* t^6A Biosynthesis Enzyme TsaC2”. The dissertation author was the primary researcher and author of this material.

Chapter 3: Anticodon loop remodeling and D-stem shape drive the specific recognition of ANN-decoding tRNAs for t^6A modification

3.1. Introduction

As described in Chapter 1, N^6-threonylcarbamoyladenosine (t^6A) is installed at position 37 of ANN-decoding tRNAs and is essential for accurate and efficient translation. The modification is formed in two steps: synthesis of the TC-AMP intermediate by TsaC/TsaC2 enzymes, followed by transfer of the threonylcarbamoyl (TC) moiety onto A37 of substrate tRNAs. In bacteria, the second step is catalyzed by the threonylcarbamoyl transfer complex, composed of TsaB, TsaD, and TsaE (2, 41, 42). In *Thermotoga maritima*, TsaB and TsaD form a $TsaB_2D_2$ complex that binds one tRNA molecule at a time and catalyzes one round of t^6A formation, while TsaE and its ATPase activity are required for multiple reaction cycles.

Although the enzymes responsible for t^6A biosynthesis have been identified and characterized biochemically, the molecular basis of substrate tRNA recognition has remained unclear. Previous *in vivo* and *in vitro* studies showed that only full-length tRNAs are competent substrates and that the presence of other tRNA modifications is not strictly required for t^6A37 formation (30, 41, 96, 97). The most important and universal determinant is the anticodon-loop sequence 36-UAA-38, which defines ANN-decoding tRNAs with A at position 38 as substrates for t^6A modification (28, 30, 96, 98-100). Additional determinants have also been identified at positions 32 and 33, although their importance varies among organisms (30, 99). Outside the anticodon loop, specific D-stem base pairs contribute to recognition by archaeal and eukaryotic KEOPS (30, 101, 102). The requirement for the 3′ CCA end differs among systems; it is essential for *M. jannaschii* and human KEOPS but dispensable for yeast, *Drosophila* and *A. thaliana* KEOPS (30, 98, 103).

Despite these biochemical data, how the t^6A biosynthesis machinery recognizes the 36-UAA-38 motif has remained unknown. Recent cryo-EM structures of tRNA-bound KEOPS provided important insight into tRNA engagement by archaeal and eukaryotic systems, but either lacked well-resolved density for the anticodon loop or captured tRNA outside the active site. Therefore, the structural basis for the strict specificity of t^6A modification toward ANN-decoding tRNAs remained unresolved.

In this chapter, I report cryo-EM structures of *T. maritima* $TsaB_2D_2$ bound to unmodified substrate tRNA and to t^6A-modified tRNA. These structures reveal how the *Tm*$TsaB_2D_2$ complex productively engages substrate tRNAs, remodels the anticodon loop, positions A37 in the active site, and recognizes the universal U36 and A38 determinants. Together, the structures provide a molecular explanation for how bacterial t^6A biosynthesis selectively targets substrate tRNAs.

3.2. Materials and Methods

3.2.1. Preparation of *Tm*$TsaB_2D_2$ for cryo-EM

Recombinant wild-type *T. maritima* TsaB and TsaD proteins (*Tm*TsaB and *Tm*TsaD, respectively) were overexpressed in *E. coli* Overexpress™ C41 (DE3) cells and purified by Ni-NTA chromatography, followed by size exclusion chromatography (SEC), as described previously (53). Protein purity was verified by Sodium Dodecyl Sulfate–Polyacrylamide Gel Electrophoresis (SDS-PAGE) analysis (Supplementary fig. 3-1A). The *Tm*$TsaB_2D_2$ complex was prepared by mixing 26 mM each *Tm*TsaB and *Tm*TsaD in buffer containing 50 mM Tris-HCl (pH 7.5), 50 mM KCl, 1 mM dithiothreitol (DTT), followed by SEC purification of the complex on an XK 16/70 column packed with 130 mL of Superdex 200 prep-grade resin (Cytiva) and equilibrated in the same buffer. The complex eluted as a single, symmetric peak and SDS-PAGE analysis of peak fractions showed the expected relative amounts of *Tm*TsaB and *Tm*TsaD

(Supplementary Fig. 3-1B). The final complex was concentrated to 3.5 mg/mL using a centrifugal filtration device, flash-cooled in liquid nitrogen and stored at -80 °C until use.

3.2.2. Preparation of tRNA for cryo-EM

E. coli $tRNA^{Thr}_{CGU}$, cloned in pEXT20 plasmid, was expressed in *E. coli* MRE600 cells as described previously (104). Cells from a 1.0 L culture were harvested and suspended in 40 mL lysis buffer (0.5 M sodium acetate, pH 5.2, 10 mM EDTA), followed by extraction with an equal volume of acid phenol-chloroform (pH 4.5) on a rocker for 2 h at room temperature. The mixture was centrifuged at 33,000 x g for 30 min, and the aqueous phase was extracted twice more with phenol-chloroform (15 min each), followed by a final wash with chloroform and centrifugation. The tRNA-containing aqueous layer was collected and subjected to anion exchange chromatography as described by Spears *et al.* (105). Briefly, the aqueous layer was pH-adjusted by adding MOPS (pH 7.0) to a final concentration of 0.1 M and applied to a Qiagen-tip 2500 anion-exchange column pre-equilibrated with 50 mM MOPS (pH 7.0), 15% isopropanol and 1% Triton X-100. The column was washed with buffer containing 50 mM MOPS (pH 7.0) and 0.2 M NaCl, and the RNA was eluted with 30 mL of 50 mM MOPS (pH 7.0), 0.75 M NaCl and 15% ethanol. The pooled RNA was further purified by reversed-phase chromatography using an XBridge Protein BEH C4 column (300 Å, 5 µm, 10 x 250 mm) connected to a Bio-Rad NGC Quest 10 Plus system. RNA was resuspended in buffer A (20 mM sodium acetate, 20 mM ammonium acetate, 380 mM NaCl, 10 mM $MgCl_2$, pH 5.2) to a final concentration of 40 mg/mL, and incubated at 75 °C for 10 min. A 25 µl aliquot was injected onto the column and eluted at 2 mL/min using the linear gradient: 0-5 min, 0% buffer B; 5-66 min, 0-11% buffer B; 66-86 min, 100% buffer B (buffer B: buffer A supplemented with 50% methanol). The two

fractions comprising the major tRNA peak were checked on a 10% denaturing polyacrylamide gel (Supplementary fig. 3-1C), then pooled and precipitated with 70% ethanol at -20 °C, and air dried. The purified tRNA was folded by suspending in 7 mM $MgCl_2$ and 1x RNAsecureTM (Thermo Fisher Scientific), heating to 75 °C for 10 min in a thermocycler, and gradually cooling to 12 °C over 75 min. Final tRNA quality was assessed by microfluidic capillary electrophoresis using an Agilent 2100 Bioanalyzer (Small RNA Kit), which revealed a single sharp peak within the expected tRNA size range (60–80 nt) and no detectable smaller or larger RNA species, indicating high sample integrity (Supplementary fig. 3-1D).

Synthetic RNA carrying the sequence of *T. maritima* $tRNA^{Lys}_{CUU}$ (Supplementary fig. 3-1E) was purchased from IDT, dissolved in water, precipitated in 70% ethanol, resuspended in 1x RNAsecureTM and folded as described for *Ec*$tRNA^{Thr}_{CGU}$. Binding of these tRNAs to *Tm*$TsaB_2D_2$ was assessed by electrophoretic mobility shift assays (EMSA) and the apparent affinities are K_d = 0.2 µM and 0.16 µM for *in vivo*-produced *Ec*$tRNA^{Thr}_{CGU}$ and synthetic *Tm*$tRNA^{Lys}_{CUU}$, respectively (Supplementary fig. 3-1F and G). Surprisingly, in t^6A synthesis assays the *in vivo*-produced *Ec*$tRNA^{Thr}_{CGU}$ exhibited ~30% of the activity observed with the *Ec*$tRNA^{Thr}_{CGU}$ *in vitro* transcript (prepared as described below), consistent with the presence of a fraction of unmodified species (Supplementary fig. 3-1H).

3.2.3. Validation of tRNA identity and modification status of purified *E. coli* $tRNA^{Thr}_{CGU}$ by chromatography-coupled mass spectrometry

To confirm the identity of the *in vivo* expressed *E. coli* $tRNA^{Thr}_{CGU}$ and map its modifications, liquid-chromatography tandem mass spectrometry LC-MS/MS was performed. The RNA (200 ng) was digested in a 10 µL reaction containing 10 mM ammonium formate (pH 7), 1 mM EDTA, and 200 U RNase T1 (a G-specific RNase), and incubated at 37 °C for 10 min, followed by 50 °C for 2 min, and then 37 °C for 5 min. The sample was dried under SpeedVac,

reconstituted in 1 µL butylamine-acetic acid buffer (pH 8.0), and analyzed by reversed-phase ion-pair liquid chromatography on an Agilent 1200 Nanoflow LC system. Separation was performed on a homemade 0.15 mm × 150 mm C18 column using 10 mM butylamine-acetic acid buffer in water (pH 8) as eluent A, and methanol as eluent B, with a 15–40% B gradient at a flow rate of 1 µL/min. Data-dependent MS/MS (ddMS^2) characterization was performed on an Agilent 6550 Q-TOF system equipped with an Agilent nano spray source and operated in negative ion mode. MS^1 spectra were collected over *m/z* 250–2000 at a scan rate of 2 spectra/s. The three most intense species in the first quadrupole were selected for fragmentation using a formulated collision engine (slope 1.4, offset 14). MS^2 spectra were acquired at 2 spectra/s with active exclusion after three spectra from the same MS^1. MS^1 signals in the 250–400 *m/z* range were excluded from MS^2 analysis. Data were processed using ProteoWizard msConvert (106), and analyzed with NucleicAcidSearchEngine (NASE) within OpenMS (106-108) against *E. coli* K-12 MG1655 mature tRNA sequences downloaded from GtRNAdb (109) (https://gtrnadb.org) as the reference library. The full list of fragment ion types (a-B, a, b, c, d, w, x, y, z) was considered for peak matching. Precursor and fragment mass tolerance were both set to 10 ppm. Apart from common fragments such as the 3′-terminal "CACCA", which are shared by tRNA$^{Thr}_{CGU}$ and many other tRNAs, several fragments matched to sequences shared by tRNA$^{Thr}_{CGU}$ 1-1 and tRNA$^{Thr}_{CGU}$ 2-1 (GtRNAdb nomenclature), and one fragment matched to a region shared by tRNA$^{Thr}_{CGU}$ 1-1 and tRNA$^{Thr}_{GGU}$ 1-1. No detected fragments mapped uniquely to tRNAs other than tRNA$^{Thr}_{CGU}$ 1-1. Six distinct modifications were assigned to six positions on this tRNA: s^{4}U at position 8, D at positions 16 and 17, t^{6}A/ct^{6}A at position 37, m^{7}G at position 46, and m^{5}U at position 54 (Supplementary fig. 3-2A). Dihydrouridine at position 20, which is known to occur in this tRNA (60), was not detected. Since pseudouridine cannot be

differentiated from uridine by mass spectrometry, the presence of pseudouridine at positions 39 and 55 (Ψ39 and Ψ55) was not confirmed. The annotated MS^2 spectra of "U[t^6A]AUG" and "U[ct^6A]AUG," together with the annotated peak of the free t^6A and ct^6A bases, confirm the presence of both modifications at position 37 (Supplementary fig. 3-2B and C). Altogether, these data confirm the identity of the enriched species as *E. coli* $tRNA^{Thr}_{CGU}$ 1-1, with t^6A and ct^6A detected at position 37. Other tRNA species, if present, are below the detection limit of this assay.

3.2.4. Complex assembly and cryo-EM grid preparation

Complexes of *Tm*$TsaB_2D_2$ with *Tm*$tRNA^{Lys}_{CUU}$ or with *Ec*$tRNA^{Thr}_{CGU}$ were prepared following the same protocol. Folded tRNA was mixed with pre-formed and SEC-purified *Tm*$TsaB_2D_2$ in equimolar amounts to a final complex concentration of 2 µM (~10-fold above the apparent K_d, as measured by EMSA, Supplementary fig. 3-1D and E) in buffer containing 50 mM Tris (pH 7.5), 50 mM KCl, 5 mM $MgCl_2$ and 1 mM DTT, and incubated on ice for 1 hr. Cryo-EM grids were prepared using a Leica EM GP2 automated plunge freezer. A 3-µl aliquot of the complex was applied to a glow-discharged 300-mesh gold flat grid (Electron Microscopy Sciences Au-flat 1.2 µm/1.3 µm) treated at 15 mA for 45 s. Sample application and blotting were performed in a chamber maintained at 21 °C at 99% relative humidity. Grids were blotted for 5 s and immediately plunged into liquid ethane.

3.2.5. Cryo-EM data collection and processing

For each structure, cryo-EM data were collected from a single grid on a 300 kV Titan Krios transmission electron microscope equipped with a Gatan K3 direct electron detector. Images were acquired at 105,000X nominal magnification in super-resolution mode, a physical pixel size of 0.8266 Å (super resolution pixel size is 0.4133 Å), and defocus range -0.8 to -2.2

μm. Movies were collected at a 37° stage tilt using SerialEM v4.1.2, at a dose rate of 18 e^-/pixel/s, with a total electron dose of 50 $e^-/Å^2$ applied over 50 frames. Data processing was performed using cryoSPARC v4.5.3 (110). Raw movies were motion corrected using Patch Motion Correction and binned-2-fold to the physical pixel size 0.8266 Å for all subsequent processing. Following Patch CTF Estimation and junk detection, micrographs were curated manually.

3.2.5.1 Processing of the *Tm*TsaB$_2$D$_2$/*Ec*tRNA$^{Thr}_{CGU}$ dataset.

Particles were initially picked on a subset of 1200 micrographs using the automated Blob Picker with a Gaussian template (35-160 Å diameter). 2D classification, *ab initio* 3D reconstruction, and heterogeneous refinement into four 3D classes identified one class (73 K particles) with clear features of the ribonucleoprotein complex. This subset was subjected to homogeneous refinement and non-uniform refinement, yielding an initial consensus map at 4.4 Å resolution. 2D templates generated from this map were used for template-based particle picking across the full dataset. The resulting particles were classified by two rounds of 2D classification, and selected particles generated five ab initio volumes, which served as references for heterogeneous refinement. Particles corresponding to classes representing the ribonucleoprotein complex were pooled and further curated by 3D classification to improve compositional and conformational homogeneity. Per-particle defocus and global aberrations (beam tilt, trefoil and anisotropic magnification) were refined, followed by reference-based motion correction. Particles were then refined by non-uniform refinement and masked local refinement using a mask encompassing TsaB$_2$/TsaD/tRNA. The final 3D reconstruction reached a resolution of 3.2 Å (gold-standard FSC 0.143), with a 3D-FSC sphericity of 0.947, indicating near-isotropic resolution.

3.2.5.2 Processing of the *Tm*TsaB$_2$D$_2$/*Tm*tRNA$^{Lys}_{CUU}$ dataset.

Particles were initially picked with the automated Blob Picker with a Gaussian template (35-175 Å) and were directly used for ab initio 3D reconstruction into six 3D volumes, followed by heterogeneous refinement. One 3D volume (~535 K particles) exhibited features of the ribonucleoprotein complex. Particles contributing to this volume were further curated by 2D classification, iterated with ab initio reconstruction and heterogeneous refinement into 3-5 classes, resulting in one good class (62 K particles) for subsequent homogeneous and non-uniform refinement to generate a 4.3 Å consensus map. 2D templates generated from this map were used for template-based picking. Following the same cleanup procedure described above, ~51 K template-picked particle images were curated. Particles from blob picking and template picking were combined and duplicates removed. The particle stack was further cleaned by 3D classification to remove low-quality images. Following local and global CTF refinement, and reference-based motion correction, particles were refined by non-uniform refinement, then masked local refinement using a mask encompassing TsaB$_2$/TsaD/tRNA. The final 3D reconstruction reached a resolution of 3.2 Å (gold-standard FSC 0.143) with a 3D-FSC sphericity of 0.95, indicating near isotropic resolution. Local resolution maps were calculated using CryoSPARC's Local Resolution Estimation tool, and 3D-FSC was calculated using the 3dfsc.salk.edu server (111). All data collection and processing details are included in Supplementary Table 3-1. The final reconstructions were uploaded to the Electron Microscopy Data Bank (EMDB).

3.2.6. Atomic model building and refinement

The maps were locally sharpened using DeepEMhancer (112) prior to model building. The starting model for *Ec*tRNA$^{Thr}_{CGU}$ was extracted from its published crystal structure bound to threonyl-tRNA synthetase (PDB ID 1qf6) (113). The starting model for *Tm*tRNA$^{Lys}_{CUU}$ was generated in AlphaFold 3 (114). The previously reported crystal structure of *T. maritima* $TsaB_2D_2E_2$ (PDB ID 6n9a) (2) served as a starting model for the protein, with the TsaE subunits removed. For each structure, the initial models were rigid-body docked into the cryo-EM map using phenix.dock_in_map (115) and manually adjusted in Coot (86). In addition to global adjustments, the tRNA anticodon loop, the lever arm of TsaD, and the C-terminal tail of TsaB were remodeled to fit the experimental density. For the modified *Ec*tRNA$^{Thr}_{CGU}$, since the final map does not provide unambiguous density for most base modifications, the tRNA was modeled using canonical nucleotides except at position A37 where additional density extending from the adenine N^6 atom consistent with a threonylcarbamoyl substituent was visible, hence t^6A_{37} was modeled in the conformation most compatible with the density. Likewise, the CCA end and D-loop nucleotides D16 and D17 lacked density and were not modeled. The final models were refined using phenix.real_space_refine (116) with secondary-structure restraints applied, and validated using PHENIX validation tools and the wwPDB online validation server (117).

3.2.7. Preparation of mutant proteins

Point mutagenesis was carried out on *Tm*TsaB and *Tm*TsaD using the Q5® Site-Directed Mutagenesis Kit (NEW ENGLAND Biolabs Inc.) and the primers listed in Supplementary Table 3-2. All mutations were verified by sequencing. The mutant proteins were overexpressed in *E.*

coli and purified as described for the wild-type protein, and their purity verified by SDS-PAGE analysis (Supplementary fig. 3-1A).

3.2.8. Preparation of *E. coli* $tRNA^{Thr}_{CGU}$ *in vitro* transcript for t^6A assays

DNA templates for in vitro transcription of the WT and mutant sequences of *Ec*$tRNA^{Thr}_{CGU}$ were produced as described previously (118). Transcription reactions were incubated at 37 °C for 5 hr in 100 mM HEPES (pH 7.5), 2.0 mM spermidine, 25 mM $MgCl_2$, 40 mM DTT, 0.01% Triton X-100, 5.0 mM NTPs, 0.15 pM DNA template, 0.5 U/mL inorganic pyrophosphatase, and 80 µg/mL of the Δ(172-173) variant of the T7 RNA polymerase (119). After transcription, a phenol-chloroform extraction was performed. The tRNA transcripts were then precipitated by the addition of 1/15 volume of 7.5 M ammonium acetate and 2.5 volumes of 100% ethanol, and cooling at -20 °C for 2 hr or overnight. RNA was collected by centrifugation at 16,000 g for 30 min at 4 °C and resuspended in 1X TE buffer (pH 7.5). The solution was mixed 1:1 with formamide and heated at 95 °C for 5 min. The RNA was purified via gel electrophoresis on a 12% polyacrylamide gel containing 7 M urea. RNA was visualized via UV-shadow and extracted from the gel by crush and soak. The eluate was precipitated as described above and resuspended in 1 mM citrate buffer (pH 6.4), and folded by addition of 7 mM $MgCl_2$, heating to 75 °C for 10 min, and gradual cooling to 12 °C over 75 min.

3.2.9. Determination of *Tm*TsaC2 concentration for initial velocity assays

Assays to test the *Tm*TsaC2 concentration at which TC-transfer kinetics dominate in the production of t^6A-modified tRNA were performed in reaction volumes of 35 µL. Each assay contained 50 mM Tris-HCl at pH 8.00, 100 mM KCl, 5 mM DTT, 5 mM $NaHCO_3$, 10 mM $MgCl_2$, 2 mM ATP, 250 µM L-[U-^{14}C]-threonine (30 µCi/µmol), 10 µM *Ec*$tRNA^{Thr}_{CGU}$ transcript, 0.2 µM *Tm*TsaB, 0.2 µM *Tm*TsaD, 0.2 µM *Tm*TsaE, and 0.0313, 0.0625, 0.125, 0.25,

0.5, 1, 2, or 4 μM *Tm*TsaC2. Reactions were incubated at 60 °C, and quenched after 2 minutes in 350 μL of cold 10% TCA. The tRNA was allowed to precipitate on ice for at least 15 minutes, and then was transferred to Whatman GF/C filters, and the reaction tubes were washed three times with cold 10% TCA. The filters were then washed with cold 10% TCA followed by cold 95% ethanol. After the filters were dried, they were submerged in 5 mL of Econo-safe^{TM} liquid scintillation counting cocktail, and radioactivity was measured with liquid scintillation counting using a Beckman LS 6500 multi-purpose scintillation counter. All assays were carried out in duplicate, and the results represent at least three independent trials.

3.2.10. t^6A activity assays

t^6A activity assays were performed under initial velocity conditions in 100 μL reactions containing 50 mM Tris-HCl at pH 8.00, 100 mM KCl, 5 mM DTT, 5 mM $NaHCO_3$, 10 mM $MgCl_2$, 2 mM ATP, 250 μM L-[U-^{14}C]-threonine (30 μCi/μmol), 10 μM *Ec*tRNA$^{Thr}_{CGU}$ transcript (WT and mutants), 0.2 μM *Tm*TsaB$^{WT/Mutant}$, 0.2 μM *Tm*TsaD$^{WT/Mutant}$, 0.2 μM *Tm*TsaE^{WT}, and 1 μM *Tm*TsaC2^{WT}. Reactions were incubated at 60 °C, and 30 μL aliquots were taken at 1, 2, and 3 minutes after reaction initiation with ATP and $_L$-threonine. Each aliquot was quenched in 350 μL of cold 10% TCA, and tRNA was allowed to precipitate on ice for at least 15 minutes. tRNA was then transferred to Whatman GF/C filters, and the reaction tubes were washed three times with cold 10% TCA. The filters were then washed with cold 10% TCA followed by cold 95% ethanol. After the filters were dried, they were submerged in 5 mL of Econo-safeTM liquid scintillation counting cocktail, and radioactivity was measured with liquid scintillation counting using a Beckman LS 6500 multi-purpose scintillation counter. All assays were carried out in duplicate, and the results represent at least three independent trials.

3.2.11. Sequence alignments

Structure-based multi-sequence alignments of bacterial TsaB and TsaD proteins were conducted in PROMALS3D (120) using all published crystal structures of these proteins and AlphaFold models of select orthologs and 540 TsaD or 550 TsaB non-redundant sequences obtained from UniProt (https://www.uniprot.org/), and the alignments were used to generate sequence logos. For tRNA, 3631 sequences for bacterial $tRNA^{Arg}_{CCU}$, $tRNA^{Arg}_{UCU}$, $tRNA^{Asn}_{GUU}$, $tRNA^{Ile}_{GAU}$, $tRNA^{Lys}_{CUU}$, $tRNA^{Lys}_{UUU}$, $tRNA^{Met}_{CAU}$, $tRNA^{Ser}_{GCU}$, $tRNA^{Thr}_{AGU}$, $tRNA^{Thr}_{GGU}$, $tRNA^{Thr}_{CGU}$ and $tRNA^{Thr}_{UGU}$ were obtained from the GtRNAdb website (https://gtrnadb.ucsc.edu/) (109) and aligned in ClustalW. Logos were generated using the WebLogo v.3.7.9 online tool (https://weblogo.berkeley.edu/logo.cgi). The sequence logo for non t^6A-accepting bacterial tRNAs was likewise generated using sequences for $tRNA^{Phe}G_{AA}$, $tRNA^{Ala}_{GGC}$, $tRNA^{Ala}_{UGC}$, $tRNA^{iMet}_{CAU}$, $tRNA^{Asp}_{GUC}$, $tRNA^{Glu}_{UUC}$, $tRNA^{Gln}_{UUG}$, $tRNA^{Gln}_{CUG}$, $tRNA^{Gly}_{CCC}$, $tRNA^{Gly}_{GCC}$, $tRNA^{Gly}_{UCC}$, $tRNA^{His}_{GUG}$, $tRNA^{Arg5}_{CCG}$, $tRNA^{Ser3}_{GGA}$, $tRNA^{Val1,2}_{GAC}$, $tRNA^{Tyr}_{GUA}$, $tRNA^{Trp}_{CCA}$, $tRNA^{Cys}_{GCA}$, $tRNA^{Leu}_{CAG}$, $tRNA^{Leu}_{GAA}$, $tRNA^{Leu}_{UAG}$, $tRNA^{Leu}_{GAG}$, $tRNA^{Leu}_{UAA}$, $tRNA^{Pro}_{UGG}$, $tRNA^{Pro}_{GGG}$ and $tRNA^{Pro}_{CGG}$.

3.3. Results

We determined cryo-EM structures of the *T. maritima* t^6A synthase bound to a modified *E. coli* $tRNA^{Thr}_{CGU}$ produced *in vivo*, and to an unmodified *T. maritima* $tRNA^{Lys}_{CUU}$ synthetic transcript. The two structures are highly similar, indicating that the mode of binding and recognition is not dependent on the tRNA modification state. The two tRNAs share 66% overall sequence identity, with complete sequence conservation in the D-stem. We have previously characterized the *Ec*$tRNA^{Thr}_{CGU}$ transcript as a competent substrate for the *T. maritima* TsaBDE

system (2, 104), and a high-resolution crystal structure is available (PDB ID 1qf6 (113)) to aid model building in the cryo-EM map. LC-MS/MS analysis of the purified *Ec*tRNA$^{Thr}_{CGU}$ identified both t^{6}A37 and ct^{6}A37 (Supplementary fig. 3-2A-C), indicating that the sample contains a mixture of modified species. Residual activity of this preparation in enzymatic assays further suggests the presence of a fraction of unmodified tRNA (Supplementary fig. 3-1H). The cryo-EM map shows density extending from the N^6 position of A37, with the shape and extent consistent with a threonylcarbamoyl moiety. At the achieved resolution of the cryo-EM reconstruction (3.2 Å), distinct modification states at A37 could not be resolved by focused 3D classification or 3D variability analysis, and among the possible modified species only t^{6}A can be modeled in the density without steric clashes. The observed density therefore likely reflects a tRNA population enriched in t^{6}A, as ct^{6}A is readily hydrolyzed to t^{6}A under the mildly alkaline conditions used for reconstitution of the protein-RNA complex (60). Accordingly, the *Ec*tRNA$^{Thr}_{CGU}$-bound structure is interpreted as representing a product-like state, whereas the *Tm*tRNA$^{Lys}_{CUU}$-bound structure represents a substrate-bound state.

3.3.1. Overall structure

Cryo-EM analysis of *Tm*TsaB$_2$D$_2$ bound to *E. coli* tRNA$^{Thr}_{CGU}$ or *T. maritima* tRNA$^{Lys}_{CUU}$ yielded 2D and 3D class averages exhibiting the expected butterfly shape of the multi-subunit protein, with one tRNA molecule bound to one protomer at the interface between the TsaD and TsaB subunits (see Supplementary fig. 3-3 and Supplementary fig. 3-4 for example 2D classes and data processing workflows). For both structures, the final reconstruction revealed interpretable density for the full-length tRNA, both TsaB subunits and one TsaD subunit. The TsaD′ subunit (in the unbound protomer) exhibited very weak density in its N-terminal domain and no density (denatured) for the C-terminal domain. Focused local refinement using a soft

mask that excluded TsaD′ improved the overall map quality and nominal resolution to 3.2 Å (Fig. 3-1A, Supplementary fig. 3-5A). Hence, the final maps and atomic models represent the *Tm*TsaB$_2$D/tRNA complex. A local resolution map indicates a resolution range of 3.0-3.4 Å in the active site and the tRNA anticodon stem-loop and D-stem regions (Fig. 3-1B), and 3.3-3.6 Å for the *Tm*tRNA$^{Lys}_{CUU}$-bound structure (Supplementary fig. 3-5B). The two structures are highly similar and superpose with r.m.s.d. 0.5 Å over 724 Cα atoms and 1.5 Å over 71 tRNA phosphates (Supplementary fig. 3-5C). The tRNA binds to a positively charged surface at the TsaD/TsaB interface (Fig. 3-1C), occupying much of the TsaE binding site observed in the crystal structure of the *Tm*TsaB$_2$D$_2$E$_2$ complex (2, 121), consistent with previous biochemical data indicating a shared binding site (53). The majority of the tRNA binding surface is contributed by the TsaD subunit, with the tRNA/TsaD and tRNA/TsaB interfaces burying 1064.7 Å^2 and 573.3 Å^2, respectively.

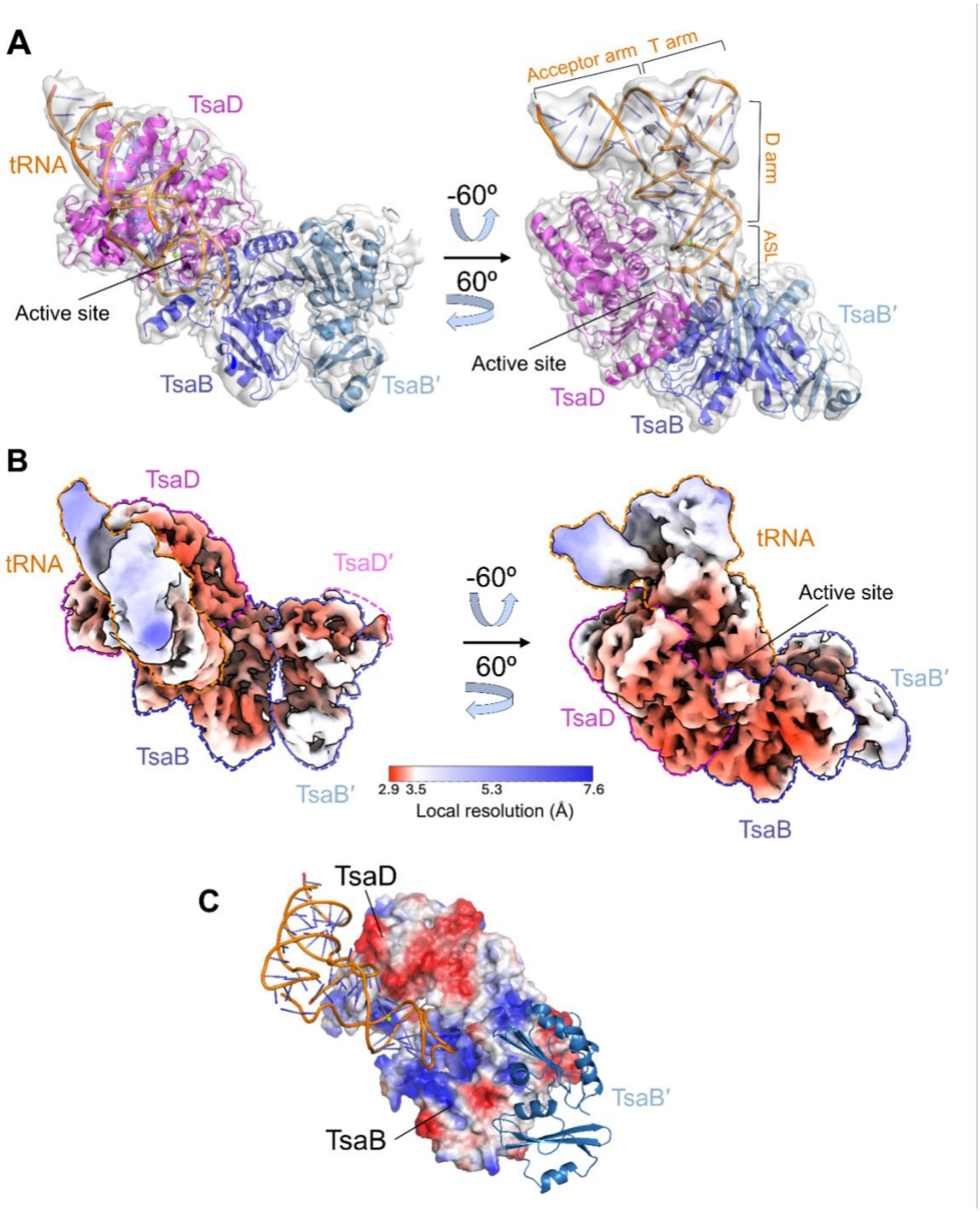

Figure 3-1: Overall structure of *T. maritima* $TsaB_2D$ in complex with *E. coli* $tRNA^{Thr}_{CGU}$. **A)** Unsharpened cryo-EM density map (overall resolution 3.2 Å) and fitted model. ASL: Anticodon stem-loop. **B)** Local resolution map, calculated at FSC 0.5 (1), showing highest resolution around the active site and anticodon loop regions. The individual subunits and tRNA are encircled with dashed lines. **C)** Electrostatic surface of the tRNA-bound protomer showing accommodation of the tRNA on the positively charged surface at the interface between the TsaB and TsaD subunits.

3.3.2. Mode of tRNA binding and conformational changes relative to the TsaE-bound state.

The enzyme recognizes the tRNA substrate via contact with the D-stem and the anticodon loop (Fig. 3-2), while no contact is made with the acceptor stem or T arm. The D-stem is contacted primarily by helix α7 of the TsaD subunit (residues Ala210-Glu223 in *Tm*TsaD numbers, Supplementary fig. 3-6), which lies along the major groove. The anticodon loop is anchored at the TsaD/B interface by the α1-α2 helical hairpin of TsaD and the C-terminal helix of TsaB (Fig. 3-2A). Deletion of the TsaB C-terminal helix (residues I195–R205) was previously shown to eliminate tRNA binding (2), consistent with its role in stabilizing the anticodon loop at this interface. The TsaD helical hairpin, comprising residues Ser31-His50 and previously referred to as the "lever arm," was shown to undergo partial unfolding and a dramatic hinged displacement away from the TsaD active site upon binding of TsaE to TsaBD (2). In the tRNA-bound structure, the hairpin is fully ordered and adopts a conformation hinged 87° toward the active site relative to its position in the TsaE-bound state (Fig. 3-2B), resembling its orientation in the absence of TsaE, as observed in the crystal structures of *E. coli, A. aeolicus* and *S. typhimurium* TsaBD (PDB IDs 6z81 (122), 8ifx (54) and 3zeu (52), respectively; Supplementary fig. 3-7A). The C-terminal helix of TsaB also swings by ~34° toward the active site relative to its position in the TsaE-bound structure. Lastly, the C-terminal helical domain of TsaD rotates toward the N-terminal domain by 28°. These movements essentially compact the enzyme and result in closing on the tRNA, trapping the anticodon loop and insertion of A37 in the active site (Fig. 3-2C and D).

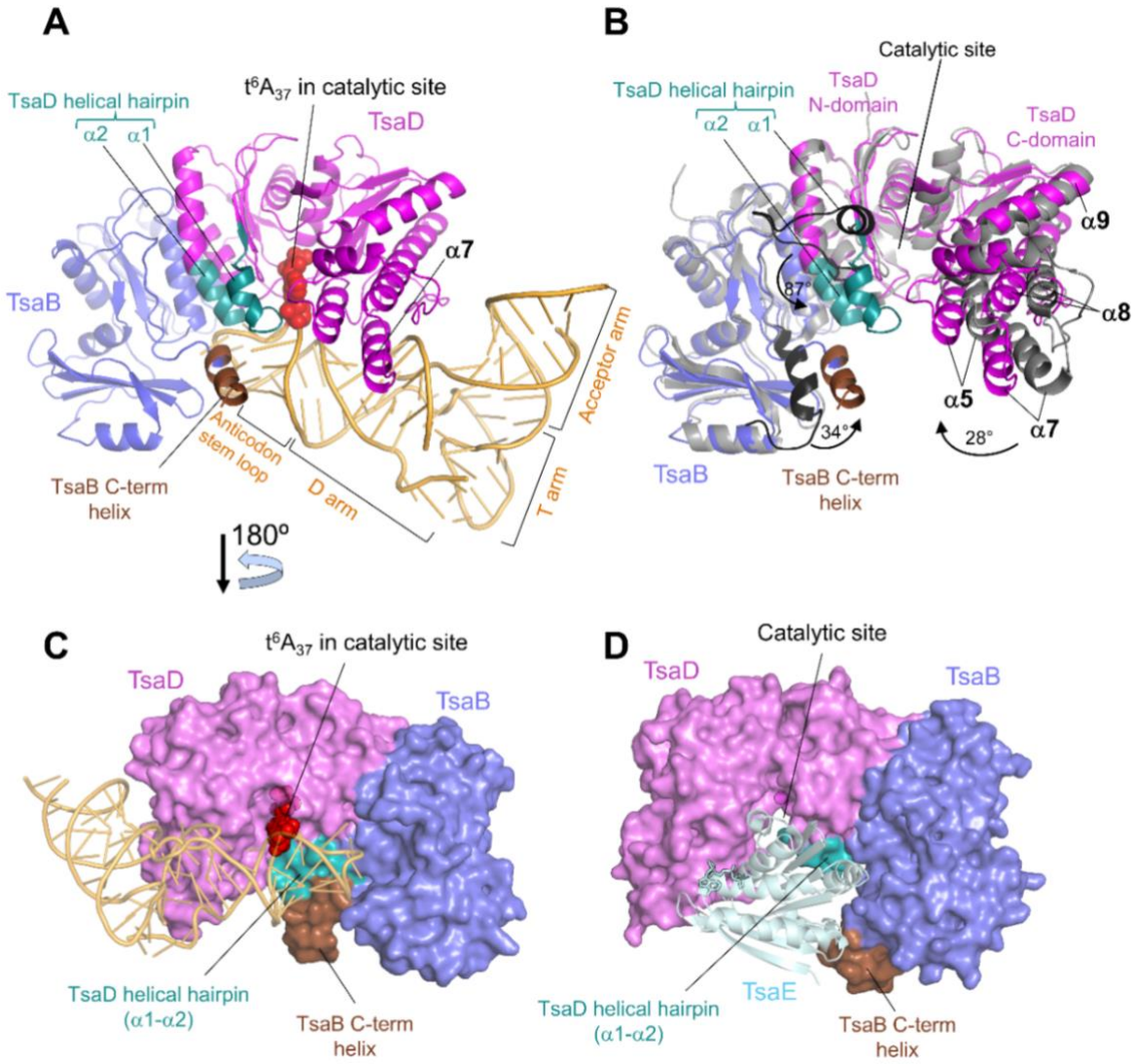

Figure 3-2: Recognition of the tRNA D-stem and anticodon loop by *Tm*TsaB$_2$D.
A) Front view of the tRNA-bound protomer of the *Tm*TsaB$_2$D/*Ec*tRNA$^{Thr}_{CGU}$ complex showing recognition of the D-stem via helix α7 in the C-terminal domain of TsaD, and trapping and bending of the anticodon loop by the α1- α2 helical hairpin (teal color) of TsaD and the C-terminal helix of TsaB (brown color). t^{6}A37 lodged in the active site of TsaD is shown in red. **B)** Superposition of the *Tm*TsaBD protomer in the tRNA-bound state (colored) onto the same protomer in the TsaE-bound state (extracted from the crystal structure of *Tm*TsaB$_2$D$_2$E$_2$, PDB ID 6n9a, gray). The comparison highlights the rotational shift in the C-terminal helical domain of TsaD, and hinge movements of the TsaD helical hairpin and the C-terminal helix of TsaB toward the active site in the tRNA-bound state. **C, D)** Back view and surface representation of the protomer in the tRNA-bound state **(C)** versus the TsaE-bound state (PDB ID 6n9a) **(D)** highlighting closure on the tRNA anticodon loop.

3.3.3. 36-UAA-38 is a t^6A determinant sequence across phyla.

In addition to A37, the defining sequence features of t^6A substrate tRNAs include the flanking bases in the anticodon loop, namely U36 at the third anticodon position and A38. 36-UAA-38 has been shown to be a strict determinant for t^6A modification in the cytosols and mitochondria of eukaryotes (28, 96, 98, 100). Although this specificity has not been experimentally investigated in bacteria, it has been inferred from the conservation of 36-UAA-38 in bacterial t^6A tRNAs. Indeed, we conducted a large-scale sequence alignment of bacterial tRNAs which clearly reveals strict conservation of the 36-UAA-38 motif in ANN-decoding tRNAs (t^6A substrates), and its absence in non-ANN-decoding tRNAs (non-substrates, Fig. 3-3A), consistent with this motif serving as a determinant across phyla. The following observations in the structure of tRNA-bound TmTsaB2D explain this ancient and universal specificity.

3.3.4. Remodeling of the anticodon loop and structural basis for recognition of the 36-UAA-38 motif.

The anticodon loop, approached by the enzyme from the minor groove side, is sharply bent toward the major groove of the anticodon stem, and remodeled to accomplish positioning of A37 in the active site of TsaD (Fig. 3-4, Supplementary fig. 3-8). The tRNA backbone is kinked at nucleotides 32, 34, 36 and 38 such that the bases 32 to 38 adopt a zigzag pattern, alternating in orientation relative to the loop path (Fig. 3-3B, Supplementary fig. 3-8A). The kinks at 36 and 38 result in extrusion of the A37 base from the loop and into the active site, and this backbone conformation is further stabilized by an apparent hydrogen bond between O2′ of U36 and a non-bridging oxygen atom of phosphate 38. The first two anticodon bases C34 and G35 (U35 in *Tm*tRNA$^{Lys}_{CUU}$) sit in shallow surface pockets that do not impose base-specific contacts (Fig. 3-3C), explaining the indifference of t^6A biosynthesis to the base identities at these positions. U36 is flipped into the loop space, breaking the weak U32:A38 non-Watson-Crick interaction

normally found in the canonical U-turn conformation of the anticodon loop (Fig. 3-3D). This positions the Watson-Crick edge of U36 within distance to make 2 hydrogen bonds with the Hoogsteen edge of A38, with the pair in *Cis* glycosidic-bond orientation and a characteristic constricted C1′-C1′ distance of ~7.9 Å. The U32 base docks into the major groove side of the U36•A38 base pair within hydrogen bonding distance from both bases, thus forming a planar U32–U36•A38 base triple with all pairs in the triple in *Cis* glycosidic-bond orientation (Fig. 3-3C). The apparent hydrogen bonding network within the triple is as follows: N3 and O4 of U36 hydrogen bond with N6 and N7 of A38, respectively. N3 of U32 hydrogen bonds with O4 of U36, and O4 of U32 with N6 of A38. According to the Leontis-Westhof classification system (123), the base triple would be classified as cWH-cWH (or cHW-cHW), considering U36 as the central base. A search in the RNA Base Triples Database (123) returned no similar triples, so to our knowledge this is the first observation of a UUA base triple in this class. Likewise, the overall conformation of the anticodon loop is not observed in any tRNA structure in the PDB, whether in free form or bound to a protein (see example comparisons in Supplementary fig. 3-7B).

The U32–U36•A38 triple is accommodated by a markedly hydrophobic trough on the protein surface, approximately 23 Å long and 8 Å deep. The trough is formed by the interhelical loop of the α1-α2 helical hairpin of TsaD and the C-terminal helix of TsaB (Fig. 3-3C, left). On the opposite side, the U32–U36•A38 triple is further stabilized by base stacking interactions with the adjacent A31:U39 Watson-Crick base pair at the proximal end of the anticodon stem. Specifically, U39 stacks on the U36•A38 pair, and A31 stacks on U32 (Fig. 3-3C, right).

Figure 3-3: Remodeling of the anticodon loop and flipping of A37 into the active site. **A)** Sequence logo for the anticodon loop of bacterial t^6A substrate tRNAs versus non t^6A-accepting tRNAs, derived from ~3630 aligned sequences, showing complete conservation of the 36-UAA-38 sequence in substrate tRNAs. **B)** Unsharpened cryo-EM map and fitted model of the anticodon loop. The local map resolution is 3.08-3.36 Å at nucleotides 32-38. Left: view of the anticodon loop from the major groove side showing the zigzag pattern of bases. Right: view illustrating bending of the anticodon loop toward the major groove of the anticodon stem. **C)** Protein surface representation showing the binding trough for the U32–U36•A38 base triple, formed by the tip of the TsaD helical hairpin (teal) and the TsaB C-terminal helix (brown). Modified A37 is lodged in the TsaD active site, and C34 and G35 are accommodated in shallow surface pockets. Red dashed lines (distances < 3. 2 Å) highlight the hydrogen bond network within the base triple and the additional hydrogen bond between O2′ of U36 and the phosphate of A38. Right: side view showing stacking of U39 on the U36•A38 Hoogsteen pair and stacking of A31 on U32. Protein surface color code is as in Fig. 3-3. For clarity, A31 and U39 are not shown in the left panel, and A37 is not shown in the right panel. **D)** Schematic illustration of the remodeled anticodon loop and binding pockets on the enzyme for the protruding bases C34, G35 and A37. Hydrogen bonds within the base triple are represented by dashed red lines.

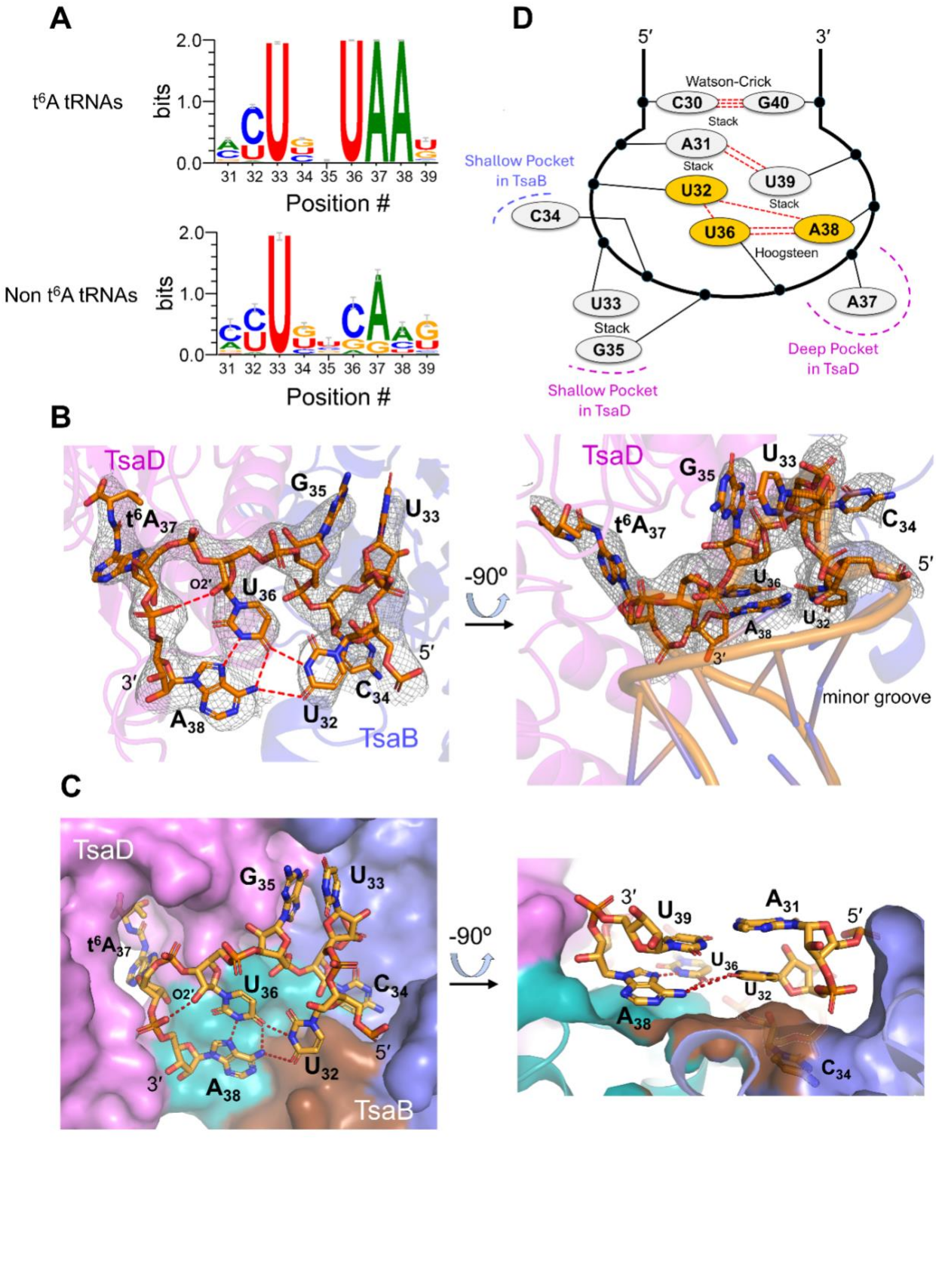
A
t6A tRNAs
bits
2.0
1.0
0.0
31 32 33 34 35 36 37 38 39
Position #
Non t6A tRNAs
bits
2.0
1.0
0.0
31 32 33 34 35 36 37 38 39
Position #
D
5′
3′
Watson-Crick
C30
G40
Stack
A31
Stack
U39
Shallow Pocket in TsaB
U32
Stack
C34
U36
A38
Hoogsteen
U33
A37
Stack
G35
Deep Pocket in TsaD
Shallow Pocket in TsaD
B
TsaD
G35
U33
t6A37
O2′
U36
5′
3′
C34
A38
U32
TsaB
-90°
TsaD
G35
U33
t6A37
C34
5′
U36
A38
U32
3′
minor groove
C
TsaD
G35
U33
t6A37
O2′
U36
C34
5′
3′
A38
U32
TsaB
-90°
3′
U39
A31
5′
U36
U32
A38
C34

The residues lining the hydrophobic trough for the base triple are Phe39, Val43, Pro44 and Leu82 from TsaD; and Ile195, Ala196 and Trp200 from TsaB, all of which are invariant or highly conserved residues in the respective protein family (Fig. 3-4A, Supplementary Fig. 3-8B, Supplementary Fig. 3-6 and Supplementary Fig. 3-9). A38 makes the most extensive stacking contacts with this trough, engaging side chains from both protein subunits, whereas U32 and U36 contact only TsaB and TsaD, respectively. U32 stacks directly against TsaB-Ile195. The U36 base and ribose rings stack against TsaD-Pro44 and TsaD-Leu82, respectively. The adenine ring of A38 stacks face-to-face against TsaD-Phe39, and edge-to-face against TsaB-Trp200, and is anchored by TsaD-Val43 and TsaB-Ala196 at the center of the trough, while its ribose O2′ makes a hydrogen bond with the backbone carbonyl oxygen of TsaD-Phe39.

The backbone phosphates of the anticodon loop receive numerous stabilizing salt-bridge interactions with basic side chains: the phosphate of U32 with TsaB-Arg114, and the A38 and U39 phosphates with Arg169 and Lys166, respectively, from helix α5 in the C-terminal domain of TsaD (Fig. 3-4A, Supplementary Fig. 3-8B). TsaD-Arg169 side chain also hydrogen bonds with the backbone carbonyl oxygen atom of TsaD-Gly40, which is part of the conserved Ω_{39}GGVVPE$_{45}$ motif (Ω is an aromatic residue) comprising the inter-helix loop of the α1-α2 helical hairpin of TsaD (Supplementary Fig. 3-6). Thus, Arg169 bridges the tip of the helical hairpin of TsaD to the phospho-ribose backbone of the anticodon loop. The functional importance of this conserved helical hairpin is further supported by prior observations that disrupting the α1 helix in *Aquifex aeolicus* TsaD nearly abolished activity (54).

Notably, the enzyme-induced sharp bend in the anticodon loop brings the phosphate of A38 into close proximity to the phosphate of A26 at the D-stem/anticodon-stem junction (Fig. 3-4B, Supplementary Fig. 3-8C). The resulting ~2.7 Å (~3.5 Å in *Tm*TsaB$_2$D/*Tm*tRNA$^{Lys}_{CUU}$

structure) separation between their non-bridging oxygen atoms is too constricted to accommodate a Mg^{2+} ion, but is consistent with hydrogen bonding. The conserved TsaD-Lys166 in contact with phosphate 38 may serve to protonate it (Fig. 3-4A and B, Supplementary Fig. 3-8C), and the cryo-EM map, reflecting the Coulomb potential, reveals intervening density consistent with a positive charge bridging these two phosphates, an observation plausible at the local resolution of 3.1 Å (124). In addition, the *Ec*tRNA$^{Thr}_{CGU}$-bound structure shows density consistent with a Mg^{2+} ion bridging phosphates 25 and 26, which would help neutralize local charge and stabilize this compact backbone arrangement, although comparable density is not observed at this position in the *Tm*tRNA$^{Lys}_{CUU}$-bound structure. Overall, the remodeling of the anticodon loop backbone and associated phosphate compaction, potential protonation and stabilization by conserved basic residues and possibly Mg^{2+} define a configuration with A37 positioned in the active site.

To validate the structure and probe the importance of these interactions in catalysis, we introduced amino acid substitutions at selected interacting residues and tested the activities of the resulting mutant proteins in the t^6A synthesis reaction (Fig. 3-4C). As the structure shows that the modified nucleosides in the tRNA body do not contact the enzyme or functional sites, their absence is not expected to affect binding or catalysis; accordingly, activity assays were performed using an *in vitro* transcribed *Ec*tRNA$^{Thr}_{CGU}$ as a substrate. This substrate has been used extensively in our prior work and provides a robust readout of t^6A synthesis (Supplementary Fig. 3-1G). Activity assays were carried out under initial velocity conditions with a molar stoichiometry of TsaC2:TsaBDE of 5:1 (10:1 TsaC2 to $TsaB_2D_2$) to ensure that TsaD catalyzed threonylcarbamoyl transferase kinetics dominated the observed rate of t^6A formation (Supplementary Fig. 3-10A and B). All mutants expressed well in *E. coli*, yielded

soluble proteins, and were purified to homogeneity (Supplementary Fig. 3-1A). The TsaD^{Pro44Ala}, TsaD^{Pro44Gly} and TsaD^{Phe39Ala} mutants – targeting residues involved in base triple stabilization – exhibited dramatically reduced t^6A synthesis activities (to 6%, 4% and 10% of wild-type levels, respectively). TsaB^{Arg114Ala} and TsaD^{Arg169Ala}, which disrupt anticodon loop backbone interactions, showed a reduction to 11% and 20% of wild-type activity, respectively. In addition to its putative role in stabilizing the anticodon loop, TsaD-Lys166 plays a previously established role in t^6A synthesis by coordinating the γ-phosphate of ATP at the TsaD/TsaE interface (2), essential for the ATPase activity of TsaBDE that drives multi-turnover t^6A synthesis. We have previously shown that *Tm*TsaB$_2$D$_2^{Lys166Ala}$ exhibits significantly reduced tRNA binding affinity, and that t^6A synthesis activity is reduced to below single-turnover levels (2), indicating a block at a step preceding ATP hydrolysis in the catalytic cycle, specifically the TC transfer step. This defect is consistent with the observed role of TsaD-Lys166 in stabilizing the anticodon loop on the enzyme.

In all tRNAs, bases at positions 32 and 38 form a universal, non-Watson-Crick pair that is essential for the formation of the canonical hairpin structure of the anticodon loop (125). They also provide loop flexibility for recognition by enzymes and for correct shaping and positioning of the anticodon triplet in the ribosome decoding center (126, 127). In the base triple observed here, this pairing pattern is reorganized such that the strictly conserved U36 and A38 form a two-hydrogen-bond pair, while the less conserved U32 contributes one interaction with each base in the pair. In bacterial t^6A tRNAs, position 32 displays a nearly equal proportion of U or C, and in rare cases an A (Fig. 3-4A). To probe the limits of tolerance at this position, we introduced the least conservative substitution, U32G, as G32 does not occur in t^6A tRNAs. The U32G tRNA mutant remains a competent substrate, exhibiting an initial velocity ~40% that of the wild-type

tRNA (Fig. 3-4D), indicating that base identity at position 32 is not a strict determinant of recognition. Modeling C32, A32 and even G32 in the structure suggests that they can all be accommodated within the base triple geometry (Supplementary Fig. 3-11), albeit with one fewer hydrogen bond relative to the observed U32–U36•A38 triple.

In contrast, substitution of U36 with C yields a tRNA mutant that fails to serve as an efficient substrate, exhibiting an initial velocity ~2% that of the wild-type tRNA (Fig. 3-4D), indicating that even a pyrimidine substitution at this position is not tolerated. This is consistent with the observed cWH geometry, as a C36•A38 pair would not satisfy the required hydrogen bonding pattern without protonation of C36, which is disfavored at physiological pH.

In summary, substrate recognition appears to be dictated by the shape and dimensions of the binding trough, together with the restrained geometry imposed on the RNA backbone by tertiary interactions with conserved basic residues of the TsaD/TsaB interface (TsaD-Lys166, TsaD-Arg169 and TsaB-Arg114), which restrict the conformational space available to the anticodon loop, confining it to a binding mode in which a structurally compatible base triple is formed. Within this framework, U36 and A38 appear to define a core pairing geometry of cWH, whereas the base at position 32 can vary while remaining compatible with that geometry and contributing to its stabilization. We propose that this structural constraint underlies the strict requirement for U36 and A38 in t^6A tRNAs and their role in defining tRNA identity for modification.

3.3.5. Shallow surface pockets for the anticodon wobble and central bases explain their "neutrality" for t^6A modification.

The tRNA wobble nucleotide C34 adopts a flipped-out conformation, rotated ~180° away from the adjacent bases U33 and G35 (Fig. 3-4E, Supplementary Fig. 3-8D). This allows U33 and G35 to stack against each other, a configuration enabled by a sharp kink in the intervening

sugar-phosphate backbone. C34 binds to a surface pocket on TsaB, with its ribose and phosphate moieties within hydrogen bonding distance from the side chains of TsaB-Thr68 and TsaB-Arg71, respectively (Fig. 3-4F, Supplementary Fig. 3-8E). Thr68 is a conserved Thr/Ser in TsaB proteins, and TsaB-Arg71 is invariant (Supplementary Fig. 3-9). The C34 nucleobase is held in a largely hydrophobic shallow pocket lined with TsaB-Leu67, TsaB-Ile195, TsaB-Ala113, TsaB-Tyr119 and the aliphatic part of TsaB-Arg114 side chain (Fig. 3-4F, Supplementary Fig. 3-8E), all of which are conserved in TsaB proteins (Supplementary Fig. 3-9). TsaB-Tyr119 is oriented for a potential, possibly water-mediated, hydrogen bond with the base (the side chain OH of Tyr119 is ~3.6 Å from the pyrimidine N4 of C34), but due to the modest map resolution in this region this interaction is not certain. We probed several of these interactions with mutagenesis. The TsaBThr68Ala mutant, targeting a backbone interaction with C34, reduced t6A synthesis to 50% of wild-type levels (Fig. 3-4C). The TsaBTyr119Ala and TsaBIle195Ala mutants, targeting the nucleobase binding pocket, reduced t6A synthesis to 70% and 58% of wild-type levels, respectively. These results are consistent with a minor contribution of the C34 pocket to anticodon loop recognition and productive binding.

In bacterial ANN-decoding tRNAs, position 34 can be U/C/G (Fig. 3-4A, Supplementary Fig. 3-12) and is often modified. An A at that position is rare because ANN codons ending with U are either rare or decoded by GNU anticodons via wobble pairing or by CNU anticodons wherein C is modified to lysidine (Supplementary Fig. 3-13). To better understand why t^6A modification is indifferent to the wobble base, we modeled U and G in place of C34 in the structure (Supplementary Fig. 3-14). The models suggest that, despite its conservation, the C34 binding pocket is large enough to accommodate a purine and can accommodate U/G with the same contacts observed for C.

The G35 nucleobase is bound in a shallow surface pocket defined primarily by TsaD-Ile83, a conserved hydrophobic residue in TsaD orthologs (Fig. 3-4G, Supplementary Fig. 3-8F, Supplementary Fig. 3-9). G35 stacks against TsaD-Ile83 on one face and against U33 on the other. The nucleobase functional groups of U33 and G35 are exposed to the solvent and neither base forms hydrogen bonds with the enzyme. The aliphatic side chain of nearby TsaB-Lys32 (a non-conserved residue) may provide an additional hydrophobic interaction with the C-H edge of U33. The lack of base-specific interactions in this pocket and its shallowness allows it to accommodate any canonical base, explaining the tolerance of t^6A modification to base identity at position 35 in substrate tRNAs. Notably, U33 is conserved in bacterial tRNAs and is unrelated to t^6A modification (Fig. 3-4A), reflecting instead its critical role in enforcing the U-turn conformation of the anticodon loop required for ribosome binding (128). Alanine substitution of TsaD-Ile83 reduced t^6A synthesis activity to 62% of wild-type levels (Fig. 3-4C), again indicating a minimal role of this binding pocket in recognition of the anticodon loop.

Figure 3-4: Recognition of the anticodon loop nucleotides.
Close-up views of the unsharpened cryo-EM map and fitted model in the individual binding pockets for anticodon-loop nucleotides. In all panels: the enzyme subunit contributing each residue is indicated in parentheses in the residue label. Color code for protein: Magenta, TsaD; teal, TsaD α1-α2 helical hairpin; blue, TsaB; brown, TsaB C-terminal helix. All distances consistent with hydrogen bonding interactions with the tRNA are < 3.3 Å (black dashed lines). **A)** Residues of the hydrophobic trough accommodating the U32–U36•A38 base triple and basic residues interacting with the triple's phospho-ribose backbone. The cryo-EM map illustrating fitness of the model is shown separately in the right panel. For clarity, only nucleotides of the base triple are displayed (transparent stick model), and the intervening RNA backbone as a ribbon. The local resolution range of the cryo-EM map in this region is 3.11-3.13 Å for TsaB residues, and 3.08-3.16 Å for TsaD residues. Red dashed lines highlight the geometry of the hydrogen bonding network within the base triple. **B)** The RNA backbone around A37 and the compacted phosphates of A38 and A26, stabilized by Mg^{2+} and the conserved TsaD basic residues Lys166 and Arg169. C25 is at the base of the D-stem. Dashed lines highlight potential interactions with distances < 3.4 Å. Mg^{2+} density in green mesh. **C)** t^6A biosynthesis activities of TsaB or TsaD mutant proteins harboring mutations in select residues interacting with the anticodon-loop, compared with wild-type activity. Assays contained mutant TsaD or mutant TsaB, all other wild-type Tsa proteins and *Ec*$tRNA^{Thr}_{CGU}$ *in vitro* transcript as substrate. Data represent duplicate measurements from at least three independent reactions. **D)** t^6A activity assay with tRNA mutants U36C and U32G. **E)** Flipped-out conformation of C34 and base stacking of U33 and G35. **F)** Residues lining the shallow hydrophobic binding pocket for the tRNA wobble base C34. Interactions consistent with hydrogen bonding are shown as dashed line. All pocket residues are from TsaB. Local resolution range in this region is 3.03-3.13 Å. **G)** The shallow surface pocket for G35, and its stacking with U33. The local resolution range in this region is 3.11-3.36 Å.

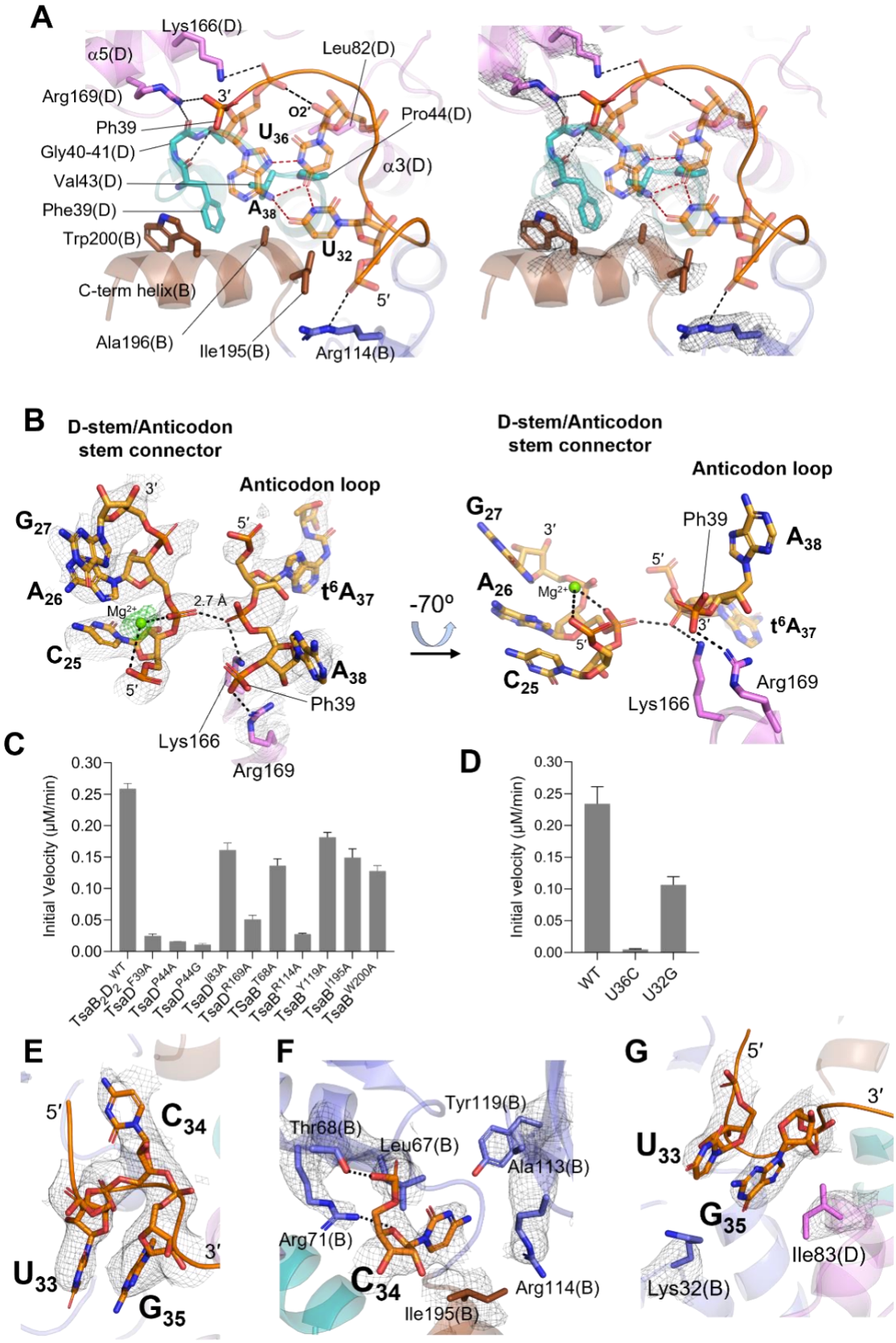
A
Lys166(D)
α5(D)
Leu82(D)
Arg169(D)
3′
O2′
Pro44(D)
Ph39
U36
Gly40-41(D)
α3(D)
Val43(D)
A38
Phe39(D)
Trp200(B)
U32
C-term helix(B)
5′
Ala196(B)
Ile195(B)
Arg114(B)
B
D-stem/Anticodon stem connector
Anticodon loop
G27
A26
Mg2+
2.7 Å
C25
t6A37
A38
Ph39
Lys166
Arg169
-70°
C
Initial Velocity (μM/min)
0.30
0.25
0.20
0.15
0.10
0.05
0.00
WT
TsaB2D2
TsaDF39A
TsaDP44A
TsaDP44G
TsaDI83A
TsaDR169A
TsaBT68A
TsaBR114A
TsaBY119A
TsaBI195A
TsaBW200A
D
Initial velocity (μM/min)
WT
U36C
U32G
E
C34
U33
G35
F
Tyr119(B)
Thr68(B)
Leu67(B)
Ala113(B)
Arg71(B)
C34
Arg114(B)
Ile195(B)
G
U33
G35
Ile83(D)
Lys32(B)

3.3.6. Accommodation of A37 and t^6A37 in the active site

The two structures, capturing A37 in the unmodified and t^6-modified forms, reveal the same configuration of the A37 binding pocket in the substrate- and product-bound states. In both structures, the adenine base is similarly lodged in a deep pocket in the active site of TsaD, lined on one side with the hydrophobic side chains TsaD-Cys10, TsaD-Leu82 and TsaD-Val42, and the glycine-rich beta-turn $S_{134}GGH_{137}$ on the other side, with the adenine ring directly stacking between Cys10 and Gly135-Gly136 (Fig. 3-5A and B). TsaD-Val42 in the inter-helical loop of the α1-α2 helical hairpin, and TsaD-Leu82 are conserved hydrophobic residues (Supplementary Fig. 3-6). TsaD-Cys10 is part of the conserved E_7-S/T-SCD_{11} sequence motif. Alanine substitutions of these residues resulted in significantly compromised t^6A biosynthesis activity: 8% and 26% of wild-type activity for TsaD-Cys10 or TsaD-Leu82, respectively (Fig. 3-5C). We also interrogated Glu162 with mutagenesis, due to its conservation and location in a well-defined helix in the vicinity of the ribose of A37, where it is potentially poised for interaction with the ribose 2′OH. Indeed, the TsaD-Glu162Ala mutant exhibits severely impaired t^6A activity (Fig. 3-5C).

In the *Ec*tRNA$^{Thr}_{CGU}$-bound structure, clear density is observed in the cryo-EM map for the threonylcarbamoyl (TC) moiety of t^6A37, which forms a network of interactions with active-site residues in the E_7-S/T-SCD_{11} and $S_{134}GGH_{137}$ motifs. Contacts in these motifs include the threonine moiety with the side chain of Ser9, and the carbonyl O with the side chain of Ser134 and the backbone amide of Gly135. We have previously shown a role for Ser134 in TC transfer, as its Ala substitution yields a mutant that supports ATP hydrolysis in the presence of TsaE but exhibits severely reduced t^6A synthesis activity to below single-turnover level, indicating a disruption specifically in the TC transfer step of the catalytic cycle (2).

TsaD proteins harbor a bound Zn^{2+} or Fe^{2+} ion in their active sites (2, 51, 54, 121, 122) that coordinates the carboxylate and phosphate moieties of TC-AMP (122) in addition to serving as a structural metal (2). Surprisingly, in both tRNA-bound structures, no metal density is observed in the cryo-EM map, although the coordination sphere residues His109, His113 and Asp296 are well defined (Fig. 3-5A and B). Instead, His109 and Asp296 side chains are within contact distance to coordinate the carboxylate group and the carbamoyl NH of the TC moiety of t^6A37, respectively (Fig. 3-5B). His137, located in an inter-strand loop in the TsaD C-terminal domain, is an additional Zn^{2+} ligand in *Tm*$TsaB_2D_2E_2$ (2), but is displaced from the zinc site in the tRNA-bound structures, as part of the global tRNA-induced closure of the C-terminal domain. The loss of metal is not explained simply by this rearrangement of the metal site, as other bacterial TsaBD structures with a similar coordination geometry retain bound metal (51, 54, 122). It is possible that the absence of metal density is due to radiation damage (129).

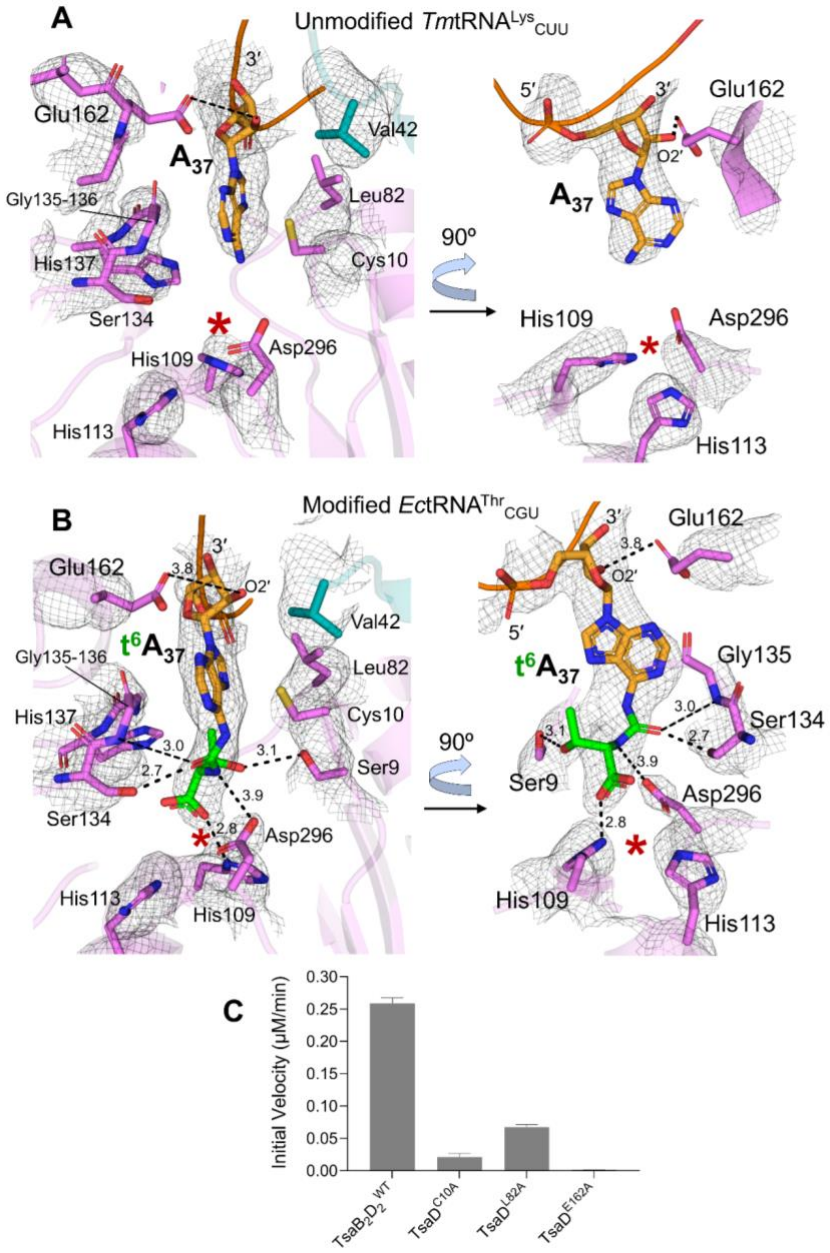

Figure 3-5: A37 binding pocket in the active site of TsaD.
A, B) Cryo-EM map, sharpened with DeepEMhancer, and fitted model shown for protein residues surrounding A37 in *Tm*TsaB$_2$D bound to unmodified *Tm*tRNA$^{Lys}_{CUU}$ **(A)** versus modified *Ec*tRNA$^{Thr}_{CGU}$ carrying the t^{6}A37 modification **(B)**. Maps show clear density for the zinc coordination residues but no bound metal. The red asterisk marks the would-be location of the metal ion. The local resolution in this region is 3.1-3.14 Å in panel A, and 3.5 Å in panel B. Val42 (teal color) is from the tip of the α1-α2 helical hairpin. Interactions within hydrogen bond distances in Å are indicated as dashed lines. **C)** t^{6}A biosynthesis activities of TsaD mutants harboring mutations in the A37 binding pocket, compared with the wild-type activity. Assays contained mutant TsaD, all other wild-type Tsa proteins and *Ec*tRNA$^{Thr}_{CGU}$ *in vitro* transcript as substrate. Data represent duplicate measurements from at least three independent reactions.

3.3.7. D-stem recognition via indirect readout

The enzyme contacts the minor groove of the D-stem via the TsaD subunit only (Fig. 3-6A). The D-stem base pairs G10:C25, C11:G24 and U12:A23 are contacted by conserved structural elements located in the C-terminal domain of TsaD (Fig. 3-6A, Supplementary Fig. 3-15). These elements are 1) the first turn of TsaD helix α7 and part of the preceding loop, together comprising the conserved sequence motif F_{207}SFSGLK$_{213}$ (Supplementary Fig. 3-6), and 2) the loop connecting strand β8 and helix α5, carrying the conserved sequence motif h$_{156}$DDs$_{159}$ (h and s are a hydrophobic and a small residue, respectively; Supplementary Fig. 3-6). The cryo-EM map and fitted model suggest a network of hydrogen bonding interactions between conserved side chains in these motifs and the N3 atoms of purines in each of the three base pairs, as well as with the ribose moieties of C25, C11 and U12. Base contacts with distances consistent with hydrogen bonds include: a network of hydrogen bonds between TsaD-Ser208, TsaD-Asp157 and the N3 atom of G10 in G10:C25 Fig. 3-6B, left; Supplementary Fig. 3-15, left); TsaD-Thr214 from helix α7 with the N3 atom of G24 in C11:G24 Fig. 3-6B, middle; Supplementary Fig. 3-15, middle); and TsaD-Tyr218 from helix α7 with N3 of A23 in U12:A23 Fig. 3-6B, right; Supplementary Fig. 3-15, right). The map and fitted model also suggest potential interactions with the RNA backbone. These include a network of hydrogen bonds between TsaD-Asp158, TsaD-Lys213 and O2′ of C25 Fig. 3-6B, left, Supplementary Fig. 3-15, left); TsaD-Ser208 with the O2′ of C11 Fig. 3-6B, middle; Supplementary Fig. 3-15, middle); and the carbonyl oxygen atom of TsaD-Gly211 with O2′ of U12 Fig. 3-6B, right; Supplementary Fig. 3-15, right). That these TsaD residues are important for the t^6A reaction is evidenced by the impact of their mutation; with the exception of Thr214 and Tyr218, which are not conserved, mutation to Ala virtually abolishes catalytic activity Fig. 3-6C). Note that Lys213 was previously

investigated (2) and, as with Lys166, was shown to serve dual roles in tRNA binding by *Tm*$TsaB_2D_2$ and in coordinating the phosphates of ATP at the TsaD/TsaE interface during the reset step of the catalytic cycle. Mutation to Ala resulted in loss of both tRNA binding and activity (2), consistent with these roles.

Despite the conservation of the D-stem sequence across bacterial t^6A substrates Fig. 3-6D, Supplementary Fig. 3-12), and the critical role of the D-stem protein contacts discussed above, $TsaB_2D_2$ is largely insensitive to the nucleotide sequence, as deduced by base-pair mutations Fig. 3-6E). Mutation of G10:C25 to A10:U25 resulted in the loss of only ~20% activity, and while flipping the base pair orientation to C10:G25 or U10:A25 resulted in a greater loss of activity, residual activity was still ~30%-40% of the wild-type activity. Similarly, mutation of C11:G24 to U11:A24, and U12:A23 to A12:U23, saw reductions in activity of only ~35%. Other D-stem mutants were not accessible to investigation because their sequences possessed alternative secondary structures of comparable stability to the tRNA cloverleaf (RNA secondary structure prediction program Mfold (130)). Together, these results indicate that although $TsaB_2D$ makes direct contacts with D-stem bases, these interactions do not mediate sequence-specific readout but instead suggest recognition through indirect readout of D-stem helix geometry and shape. Our structure adds to a growing number of examples in which α-helical elements contribute to substrate recognition through shape sensing of the tRNA D-stem. Examples include the mitochondrial tRNA methyltransferase TRMT10C (PDB ID 8cbk (131)), human Lysyl-tRNA synthetase (PDB ID 9dpl (77)), and the ELP3 subunit of the human Elongator complex (PDB ID 8ptx (132)).

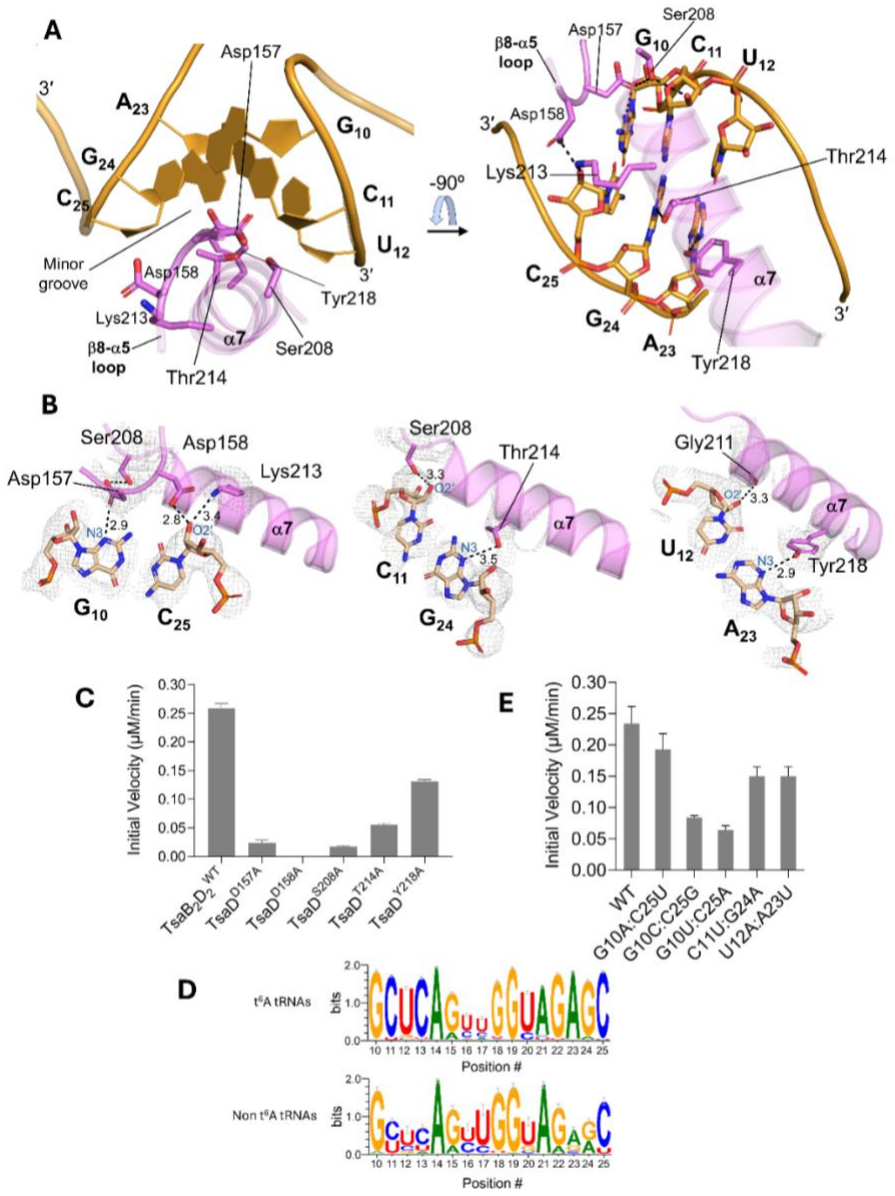

Figure 3-6: Recognition of the D-stem of tRNA.
A) Overall view of TsaD (magenta) helix α7 and the β8-α5 loop interactions with minor groove of the D-stem at base pairs G10•C25, C11•G24, U12•A23 (orange). **B)** Cryo-EM map and fitted model of individual D-stem base pairs and interacting TsaD side chains. The map local resolution in this region is 3.03-3.20 Å. Dashed lines highlight hydrogen bonding networks with distances indicated in Å. **C)** t^6A biosynthesis activity assays on *Ec*$tRNA^{Thr}_{CGU}$ *in vitro* transcript using TsaD mutant proteins harboring mutations in D-stem-interacting residues, compared with the wild-type activity. **D)** Sequence logos in the D-stem region of bacterial t^6A substrate tRNAs versus non-substrate tRNAs based on ~3630 aligned sequences. **E)** t^6A biosynthesis activities of *Tm*TsaBDE on mutant tRNAs harboring mutations in the D-stem. All activity data represent duplicate measurements from at least three independent reactions.

3.4. Discussion

We determined 3.2 Å cryo-EM structures of the *T. maritima* t^6A synthase $TsaB_2D$ in complex with two different ANN-decoding tRNA species, one unmodified and one natively modified, representing substrate- and product-bound complexes, respectively. Both structures reveal a well-ordered anticodon loop that is remodeled by the TsaB/D interface for specific recognition of the 36-UAA-38 motif and placement of A37 in the TsaD active site. The structures also offer insights into conserved and divergent features of recognition in KEOPS, as well as mechanistic insights, which we explore in the following sections.

3.4.1. Comparison with KEOPS suggests a universal mechanism for recognition of tRNA identity by t^6A biosynthesis systems.

The structures show no interaction between *Tm*$TsaB_2D$ and the CCA end of tRNA, consistent with previous findings that the CCA tail is dispensable for tRNA binding and t^6A biosynthesis by *E. coli* TsaBDE (103). This contrasts with archaeal/eukaryotic KEOPS, which requires CCA recognition via the Cgi121 subunit (103). Recently reported cryo-EM structures of archaeal KEOPS bound to $tRNA^{Lys}_{UUU}$ captured two states: one with an intact tRNA but unbound anticodon loop and A37 far from the active site, and another with a distorted tRNA in which the anticodon domain is unraveled and the anticodon loop unresolved (101, 102). Neither structure reveals the direct contacts with D-stem bases observed in the *Tm*$TsaB_2D$/tRNA complex, as the tRNA in those structures is positioned differently and the D-stem is displaced from helix α7 of TsaD (Supplementary Fig. 3-16). Nonetheless, base substitutions in the D-stem were shown to inhibit the t^6A modification activity of KEOPS (101, 102), although the substitutions tested did not maintain the Watson-Crick pairing (e.g. G9:C25 to G9:A25, or the double mutation C10:G24 to U10:G24 and U11:A12 to C11:A23 in *M. jannaschii* $tRNA^{Lys}_{UUU}$

numbers), and thus may have compromised the structural integrity of the D-stem rather than revealing base-specific recognition.

Further, in the distorted tRNA-bound KEOPS structure, G26 is flipped-out of the tRNA core and contacts a conserved arginine in the C-terminal tail of Bud32 (101, 102). In contrast, our structures show a canonical tRNA core and no flipped-out nucleotides in this region. The corresponding nucleotide in our structures is A26, whose backbone phosphate lies at the center of a network of interactions with conserved lysines and, in the *Ec*tRNA$^{Thr}_{CGU}$-bound structure, a Mg^{2+} ion that stabilize the local, highly constricted RNA backbone around A37. Further, changing G26 to C/U/A either increased or had no effect on the t^6A activity of KEOPS (101, 102), consistent with a role involving backbone remodeling rather than base-specific interaction. It is possible that the G26 protrusion observed in the distorted tRNA bound to KEOPS represents an intermediate state that occurs during loop remodeling by the enzyme.

Neither of the available KEOPS/tRNA complex structures reveals how the anticodon loop is recognized at the Kae1/Pcc1 interface. However, the TsaD recognition motifs observed in *Tm*TsaB$_2$D are conserved in Kae1 (as well as in the human ortholog OSGEP and the mitochondrial ortholog Qri7, Supplementary Fig. 3-17), suggesting a conserved mode of recognition. These include the $G_{40}GVVP_{44}$ motif at the tip of the α1-α2 helical hairpin, which forms the hydrophobic trough for the U32-A36•A38 base triple (Fig. 3-4A, Supplementary Fig. 3-8B). For example, TsaD-Pro44, on which U36 stacks, corresponds to Pro41 in *M. jannaschii* Kae1 (*Mj*Kae1), and the *Mj*Kae1^{Pro41Ala} mutation was shown to abolish the t^6A activity of KEOPS (101, 102). Also conserved are TsaD-Lys166 and TsaD-Arg169, which stabilize the anticodon loop backbone at the TsaD/TsaB interface (Fig. 3-4A and B, Supplementary Fig. 3-8B and C), and we showed that their alanine substitutions impair activity ((2) and Fig. 3-5C). The

equivalent *Mj*Kae1^{Gln160Asp} and *Mj*Kae1^{Arg163Glu} mutants were similarly shown to abolish t^6A activity of KEOPS (101-103). Likewise, the corresponding *S. cerevisiae* Qri7^{Arg207Ala} mutant failed to rescue the *kae1Δ* growth defect in yeast and is inactive *in vitro* (50).

The functional homology between TsaB and the KEOPS Pcc1 subunit with respect to anticodon loop binding is less obvious. The contribution of TsaB to anticodon loop binding is its C-terminal helix located in the C-terminal lobe, which is entirely missing in Pcc1. Pcc1 exhibits partial structural similarity to the N-terminal lobe of TsaB but lacks sequence homology. To explore how Pcc1 might engage the anticodon loop, we modeled the anticodon loop from the *Tm*TsaB$_2$D/*Ec*tRNA$^{Thr}_{CGU}$ structure (with similar results using the *Tm*tRNA$^{Lys}_{CUU}$-bound structure) onto the Kae1/Pcc1 complex (PDB ID 5jmv (133)), by superimposing the TsaD and Kae1 subunits (Fig. 3-7A). The model suggests that the N-terminal turns of Pcc1 helix α2 could serve the role of the TsaB C-terminal helix in trapping the anticodon loop. Further, Pcc1-Arg63 (*P. furiosus* numbering), an invariant residue essential for the t^6A activity of KEOPS (103), is positioned near phosphate 32, potentially mimicking the anticodon loop backbone stabilization provided by TsaB-Arg114. Notably, TsaB-Arg114 resides in the C-terminal lobe of TsaB, a region missing in Pcc1. The use of analogous arginines in different structural contexts illustrates a specific strategy by which these phylogenetically distinct proteins have achieved functional convergence for anticodon loop recognition.

3.4.2. Mechanistic insights into TC transfer from TC-AMP

To gain insight into the catalytic mechanism of t^6A formation we generated a docking model of TC-AMP and Zn^{2+} in the active site of *Tm*tRNA$^{Lys}_{CUU}$-bound TsaD (the substrate-bound complex) based on Zn^{2+} and the TC-AMP analog BK951 in the crystal structure of *Ec*TsaBD (Fig. 3-7B) (122). As noted above, His137 serves as a ligand to Zn^{2+} in the

Tm$TsaB_2D_2E_2$ structure (2), but in the tRNA-bound structure it has moved out of the coordination sphere. In the docking model it is similarly out of the way, which allows coordination by the carboxylate and phosphate oxygens of TC-AMP (Fig. 3-7B). In this arrangement TC-AMP is poised for TC transfer with N6 of A37 ~2.5 Å from the carbamoyl carbon of TC-AMP. Nucleophilic attack by N6 could be aided by proton transfer to Asp296, a Zn^{2+} ligand, which is ~4.5 Å from N6. The transient tetrahedral intermediate could then be stabilized by H-bond donation from Ser134, followed by intermediate collapse and cleavage of the bond to the phosphate oxygen of AMP. This latter step could be facilitated by proton transfer from Asp296 to the phosphate oxygen.

3.4.3. Overview of the catalytic cycle

Previous biochemical studies established that in the absence of TsaE/ATP, TsaBD supports a single turnover of t^6A synthesis, whereas TsaE-catalyzed ATP hydrolysis is required for multiple turnover. This led to a working model for the bacterial t^6A catalytic cycle in which TsaBD binds tRNA and TC-AMP, catalyzes TC transfer, and releases product tRNA without the involvement of TsaE, placing the role of TsaE after product release (Fig. 3-7C). The structures presented here define the tRNA-bound state in this cycle. Upon tRNA binding, the enzyme adopts a closed conformation in which the TsaD C-terminal domain encloses the tRNA and the α1–α2 helical hairpin of TsaD together with the C-terminal helix of TsaB pin the anticodon loop, positioning A37 in the TC-transfer site. Following product formation, the t^6A-modified tRNA is released, leaving the enzyme in a catalytically inactive state. TsaE-ATP binding induces an open, pre-reset conformation in which these structural elements are displaced from the active site, and subsequent ATP hydrolysis and TsaE release restores the closed conformation for the next cycle. In this model, several aspects remain unclear, including the basis of complex

inactivation, the role of TsaC/C2, if any, in delivering TC-AMP to the TC-transfer site and whether its binding is coordinated with tRNA. These questions await further investigation.

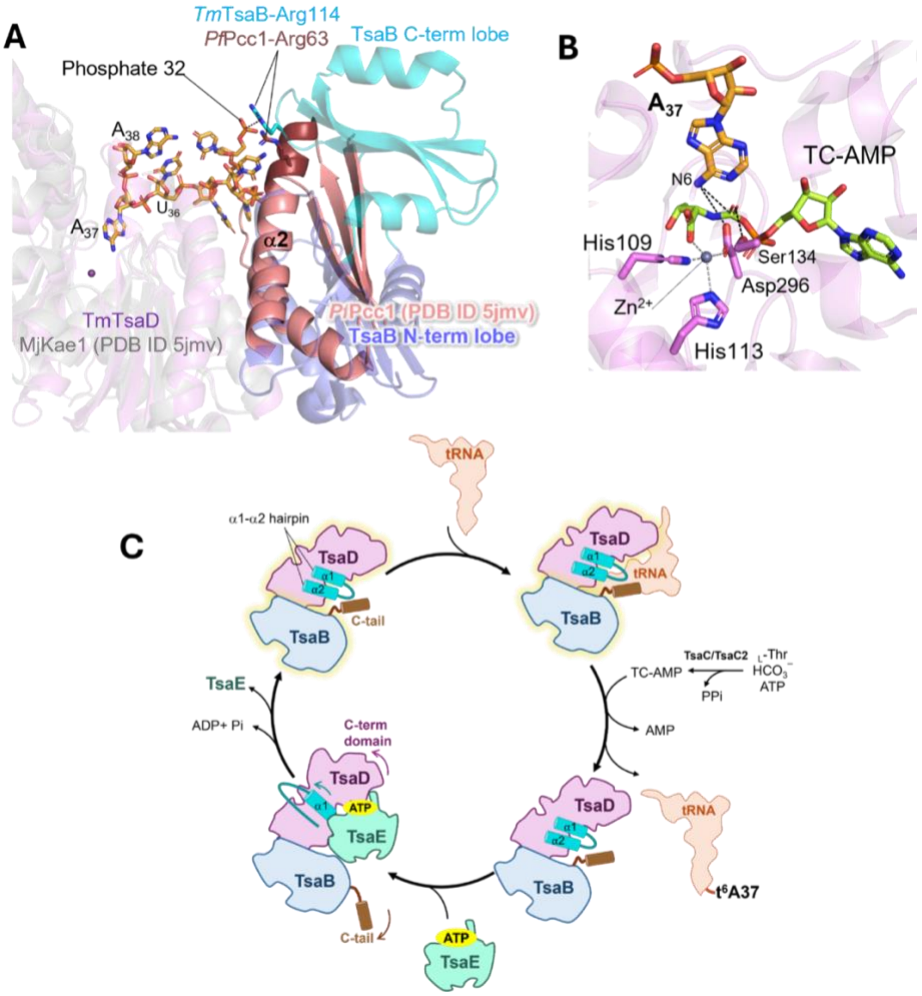

Figure 3-7: Comparison with KEOPS and mechanistic insights.
A) Superposition of the tRNA-bound *Tm*TsaBD protomer on the crystal structure of the archaeal Kae1/Pcc1 complex (PDB ID 5jmv). The view is focused on the anticodon loop binding interface, illustrating putatively similar accommodation of the zigzag conformation of the anticodon loop by Kae1/Pcc1. The conserved arginine from helix α2 of *Mj*Pcc1 is spatially analogous to Arg114 from the C-terminal lobe of TsaB, and positioned to make a similar contact with the backbone phosphate of anticodon loop nucleotide 32. For clarity, the C-terminal helix of TsaB is not shown. *Mj*: *M. jannaschii*. *Pf*: *Pyrococcus furiosus*. **B)** Docking model of TC-AMP (green) and Zn^{2+} (grey sphere) in the TC-transfer site from the *Tm*tRNA$^{Lys}_{CUU}$-bound structure, based on the positions of Zn^{2+} and the TC-AMP analog BK951 in *Ec*TsaBD (PDB ID 6z81). Putative contact network between N6 of A37, TC-AMP, Ser134 and zinc ligand Asp296 are indicated as black dashed lines. **C)** Proposed model of the bacterial t^6A biosynthesis cycle, shown for a general bacterial system (corresponding to one protomer in the *T. maritima* system), highlighting the closed, tRNA-bound, and open TsaE-ATP-bound conformational states of TsaBD along the cycle.

3.5. Supplementary material

Supplementary figure 3-1: Biochemical analysis of *T. maritima* Tsa proteins and tRNAs used in cryo-EM sample preparation and mutagenesis studies.
A) Purity check of *Tm*TsaB and *Tm*TsaD wild-type and mutant proteins by SDS-PAGE. Five µg protein were analyzed on 12% SDS-polyacrylamide gel at 150 V for 1 h. The gels were stained using Coomassie blue. **B)** Size exclusion chromatogram of *Tm*$TsaB_2D_2$ complex isolated on Superdex-200 column (left). Fractions were analyzed on 12% SDS-polyacrylamide gel (right). Fractions 7-11 (red box) were pooled and used for preparation of cryo-EM samples. **C)** Purity check of *in vivo*-produced *Ec*$tRNA^{Thr}_{CGU}$ and purified on C4 reversed-phase column. Column fractions used for cryo-EM sample preparation were analyzed on urea-polyacrylamide gel (7.0 M urea, 10% acrylamide, Tris-Borate-EDTA buffer, pH 8.3), electrophoresed for 1 h at 100 V and stained with SYBR Gold. **D)** Representative RNA electropherogram for the purified *Ec*$tRNA^{Thr}_{CGU}$ showing a single sharp peak within the expected tRNA size range (60 – 80 nt) and no peaks from smaller or larger RNA species, indicative of high sample integrity and minimal RNA degradation. **E)** sequence of *T. maritima* $tRNA^{Lys}_{CUU}$ used in cryo-EM sample preparation. **F, G)** EMSA titrations of *Tm*$TsaB_2D_2$ binding to *in vivo* produced *Ec*$tRNA^{Thr}_{CGU}$ **(F)** and synthetic *Tm*$tRNA^{Lys}_{CUU}$ **(G)** were carried out in 25 µl reactions containing 0–1.1 µM *Tm*$TsaB_2D_2$, 21 nM tRNA, 50 mM Tris–HCl (pH 7.5), 50 mM KCl, 5 mM $MgCl_2$, 5% glycerol, 3 mM DTT and 0.1 unit RNasin®. Complexes were run on 6% Tris-glycerol native polyacrylamide gel in a Tris-Glycine-EDTA native buffer (pH 8.3) for 1 h at 150 V, stained with SYBR Gold and imaged on a ChemiDoc imaging system. Band densities were quantified using ImageJ software, and the ratio of bound to total tRNA was calculated. The dissociation constant was calculated by plotting the percent tRNA bound versus protein concentration and fitting to the Hill equation using GraphPad Prism software version 11.0.0. **H)** t^6A biosynthesis activity of wild-type *Tm*TsaBDE with *in vitro* transcribed *E. coli* $tRNA^{Thr}_{CGU}$ and *in vivo*-produced *E. coli* $tRNA^{Thr}_{CGU}$, Activities were measured under initial velocity conditions using the ^{14}C-radiochemical incorporation assay as described in Materials and Methods.

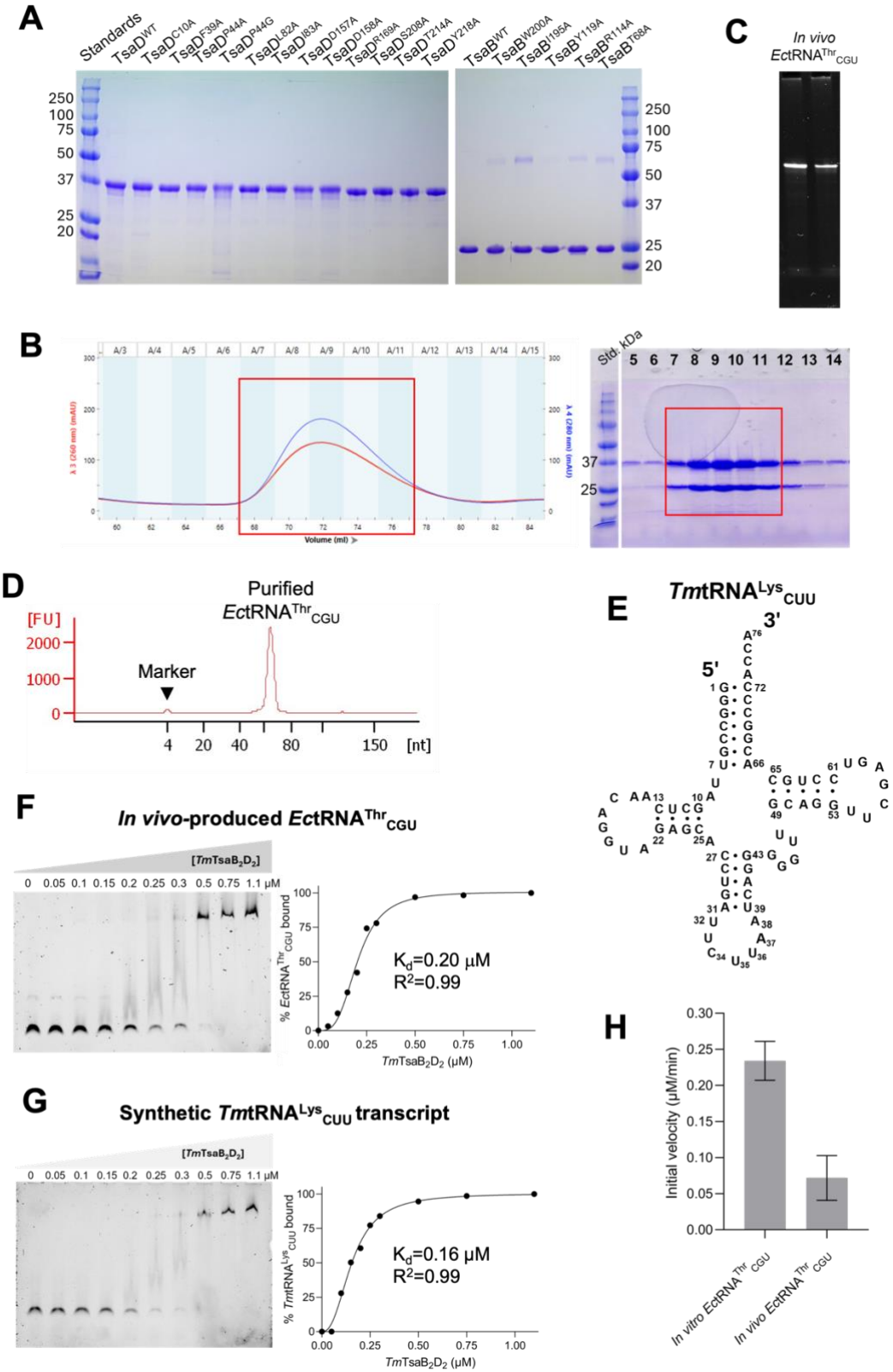
A
Standards
TsaD^WT
TsaD^C10A
TsaD^F39A
TsaD^P44A
TsaD^P44G
TsaD^L82A
TsaD^I83A
TsaD^D157A
TsaD^D158A
TsaD^R169A
TsaD^S208A
TsaD^T214A
TsaD^Y218A
TsaB^WT
TsaB^W200A
TsaB^I195A
TsaB^Y119A
TsaB^R114A
TsaB^T68A
250
100
75
50
37
25
20
C
In vivo
EctRNA^Thr_CGU
B
Std. kDa
5 6 7 8 9 10 11 12 13 14
37
25
Volume (ml)
D
Purified
EctRNA^Thr_CGU
[FU]
2000
1000
0
Marker
4 20 40 80 150 [nt]
E
TmtRNA^Lys_CUU
3'
5'
F
In vivo-produced EctRNA^Thr_CGU
[TmTsaB2D2]
0 0.05 0.1 0.15 0.2 0.25 0.3 0.5 0.75 1.1 µM
% EctRNA^Thr_CGU bound
Kd=0.20 µM
R2=0.99
TmTsaB2D2 (µM)
G
Synthetic TmtRNA^Lys_CUU transcript
[TmTsaB2D2]
0 0.05 0.1 0.15 0.2 0.25 0.3 0.5 0.75 1.1 µM
% TmtRNA^Lys_CUU bound
Kd=0.16 µM
R2=0.99
TmTsaB2D2 (µM)
H
Initial velocity (µM/min)
0.30
0.25
0.20
0.15
0.10
0.05
0.00
In vitro EctRNA^Thr_CGU
In vivo EctRNA^Thr_CGU

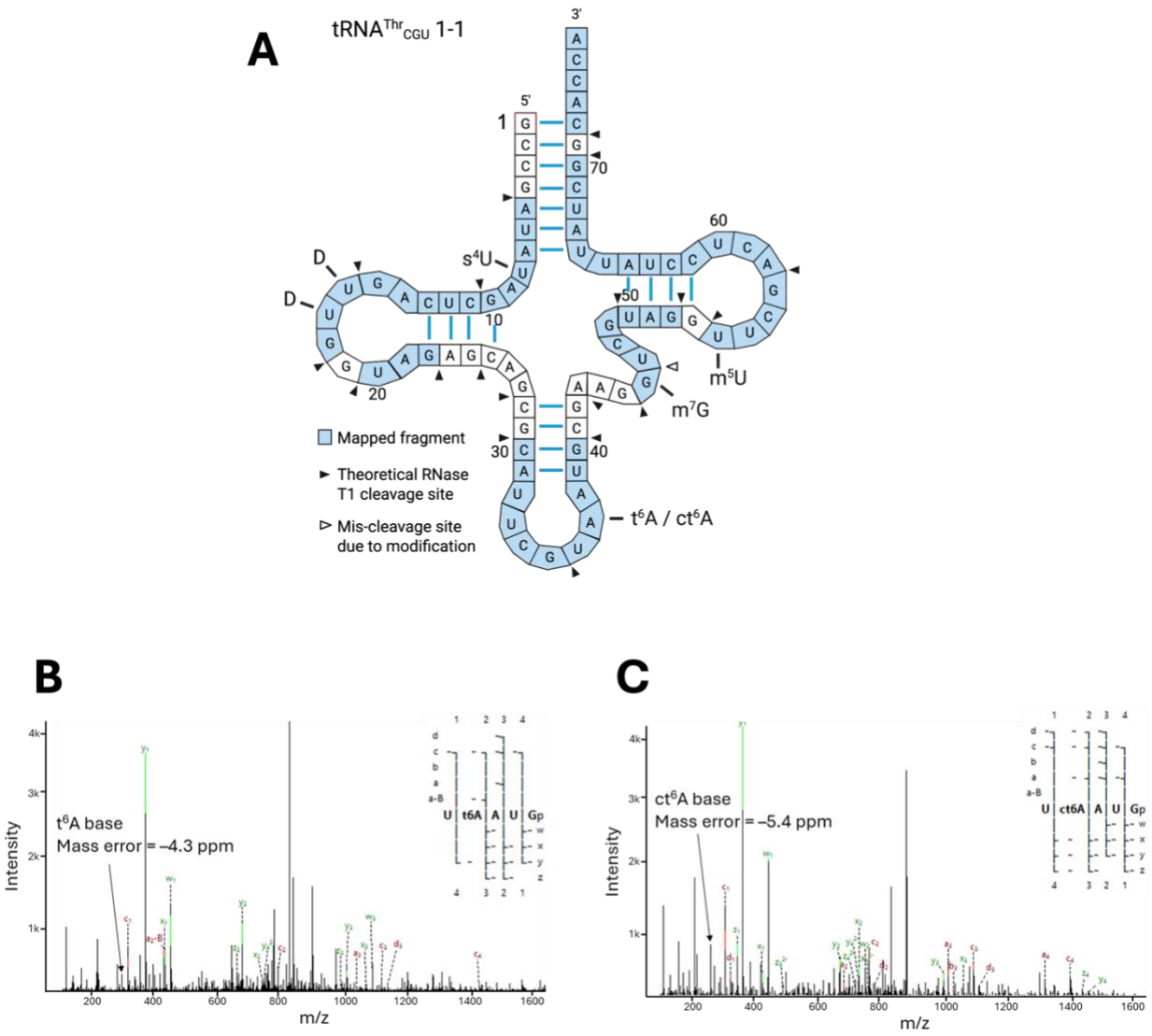

Supplementary figure 3-2: Modification mapping of the *in vivo* produced and purified *E. coli* $tRNA^{Thr}_{CGU}$ used in the cryo-EM sample for the *Tm*TsaB$_2$D/*Ec*$tRNA^{Thr}_{CGU}$ structure.
A) Schematic of *E.coli* $tRNA^{Thr}_{CGU}$ 1-1 showing the sequences identified by data-dependent LC-MS/MS analysis (light blue). Six distinct modifications are indicated at their respective positions. **B, C**) Annotated MS2 spectra of "U[t^6A]AUGp" **(B)** and "U[ct^6A]AUGp" **(C)**, with ions corresponding to the free t^6A/ct^6A bases highlighted.

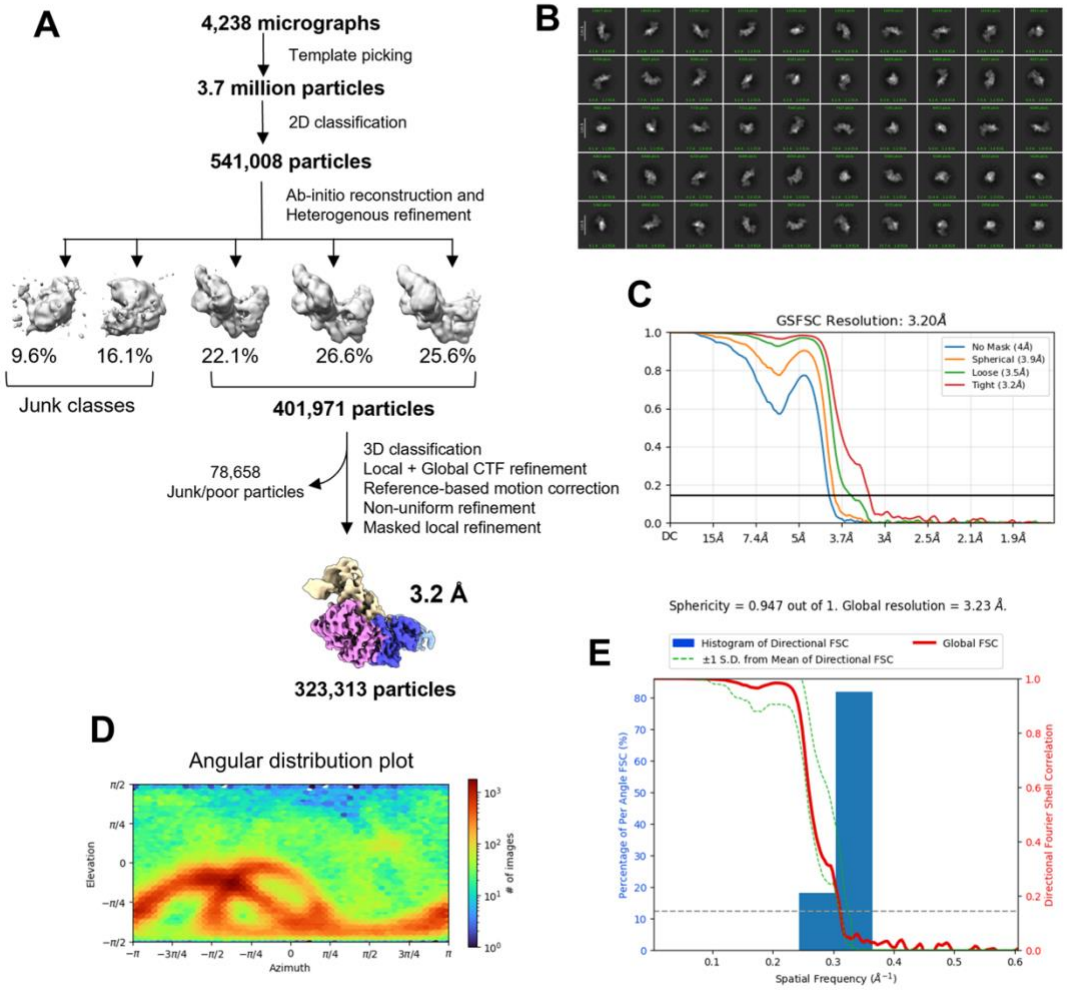

Supplementary figure 3-3: Cryo-EM data processing and map quality statistics for *Tm*TsaB$_2$D/*Ec*tRNA$^{Thr}_{CGU}$.
A) Image processing workflow chart. **B)** Example 2D classes for the final particle set. **C)** Gold-Standard Fourier Shell Correlation (GSFSC) plot generated from independently refined half-maps. **D)** Angular distribution plot showing the distribution of particle orientations contributing to the final reconstruction. **E)** 3D-FSC plot for the final reconstruction, showing mild directional resolution anisotropy (calculated using the 3dfsc.salk.edu server). The 3D-FSC was thresholded at 0.143, while sphericity was calculated by thresholding the 3D-FSC at 0.5. An overall sphericity of 0.947 shows that the global resolution of 3.2 Å is near-isotropic in three dimensions, with no significant anisotropy in the reconstruction.

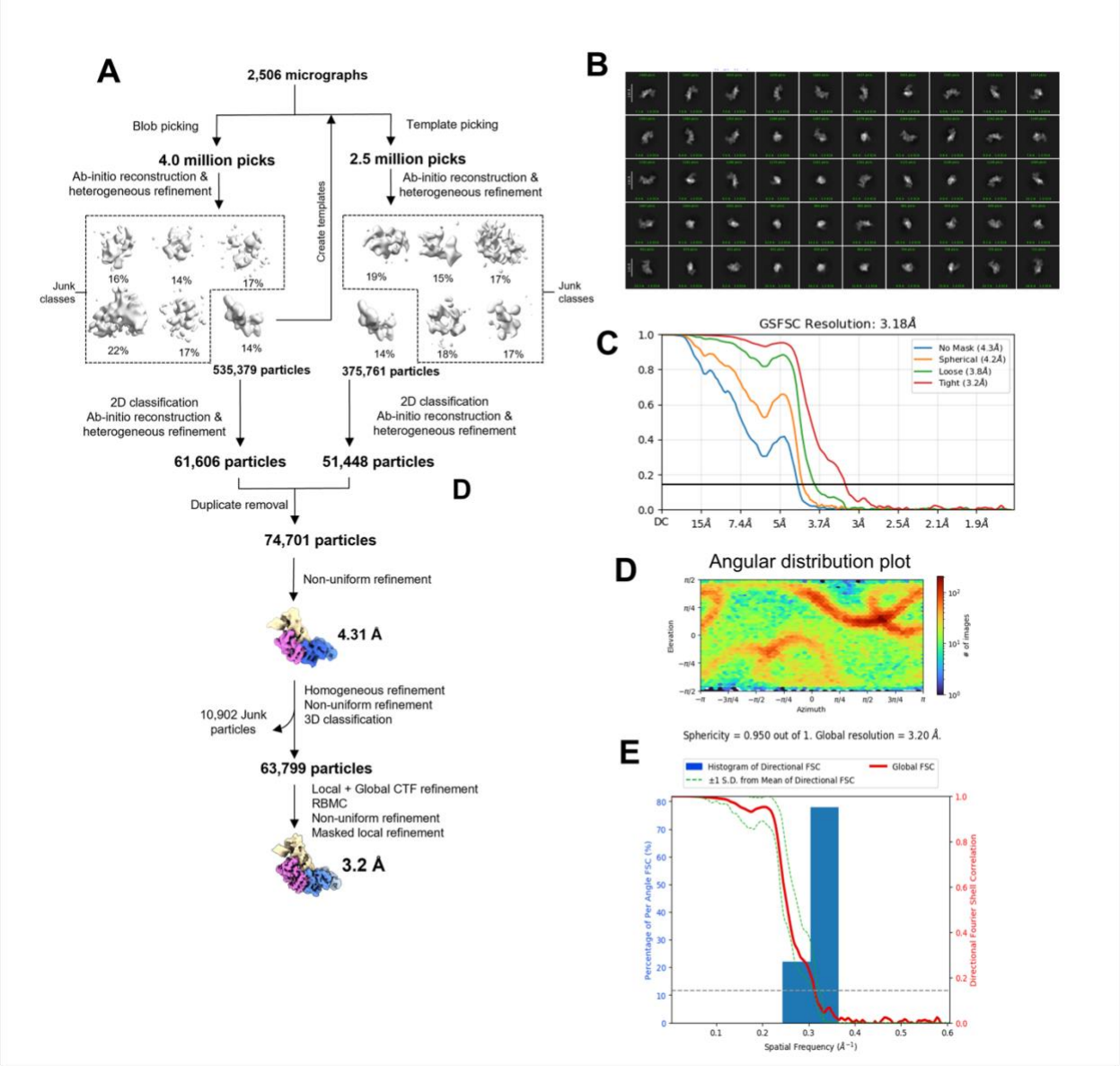

Supplementary figure 3-4: Cryo-EM data processing and map quality statistics for *Tm*TsaB$_2$D$_2$/*Tm*tRNA$^{Lys}_{CUU}$.
A) Image processing workflow chart. **B)** Example 2D classes for the final particle set. **C)** Gold-Standard Fourier Shell Correlation (GSFSC) plot generated from independently refined half-maps. **D)** Angular distribution plot showing the distribution of particle orientations contributing to the final reconstruction. **E)** 3D-FSC plot for the final reconstruction, showing mild directional resolution anisotropy (calculated using the 3dfsc.salk.edu server). The 3D-FSC was thresholded at 0.143, while sphericity was calculated by thresholding the 3D-FSC at 0.5. An overall sphericity of 0.95 shows that the global resolution of 3.2 Å is near-isotropic in three dimensions, with no significant anisotropy in the reconstruction.

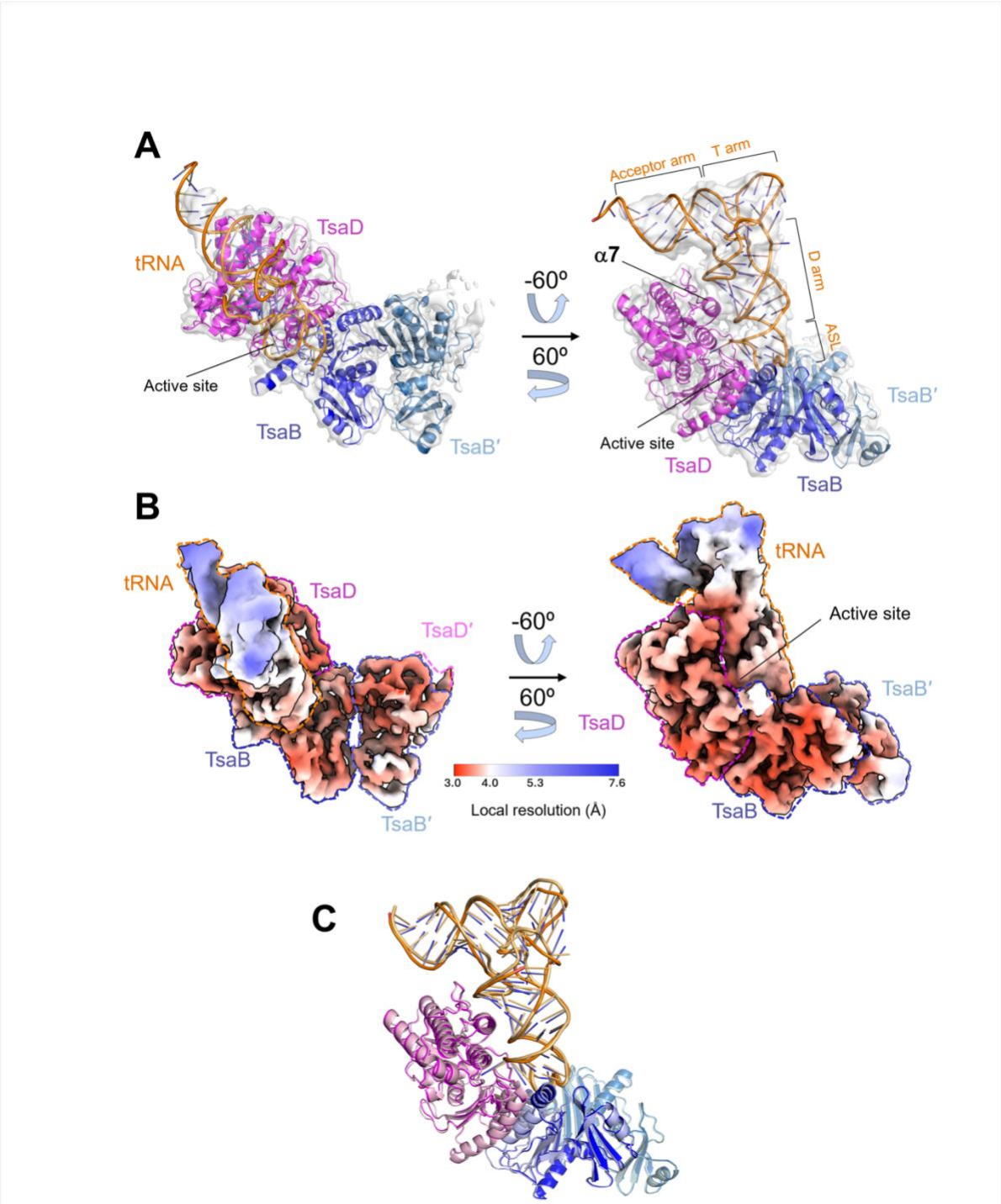

Supplementary figure 3-5: Overall structure of *Tm*TsaB$_2$D/*Tm*tRNA$^{Lys}_{CUU}$ complex. **A)** Unsharpened cryo-EM density map (overall resolution 3.2 Å) and fitted model. ASL: Anticodon stem-loop. **B)** Local resolution map, calculated at FSC 0.5, with the individual subunits encircled with dashed lines. **C)** Comparison of the final cryo-EM structural models for *Tm*TsaB$_2$D bound to *Ec*tRNA$^{Thr}_{CGU}$ (dark colors) versus *Tm*tRNA$^{Lys}_{CUU}$ (light colors), showing similar overall structure and tRNA binding mode.

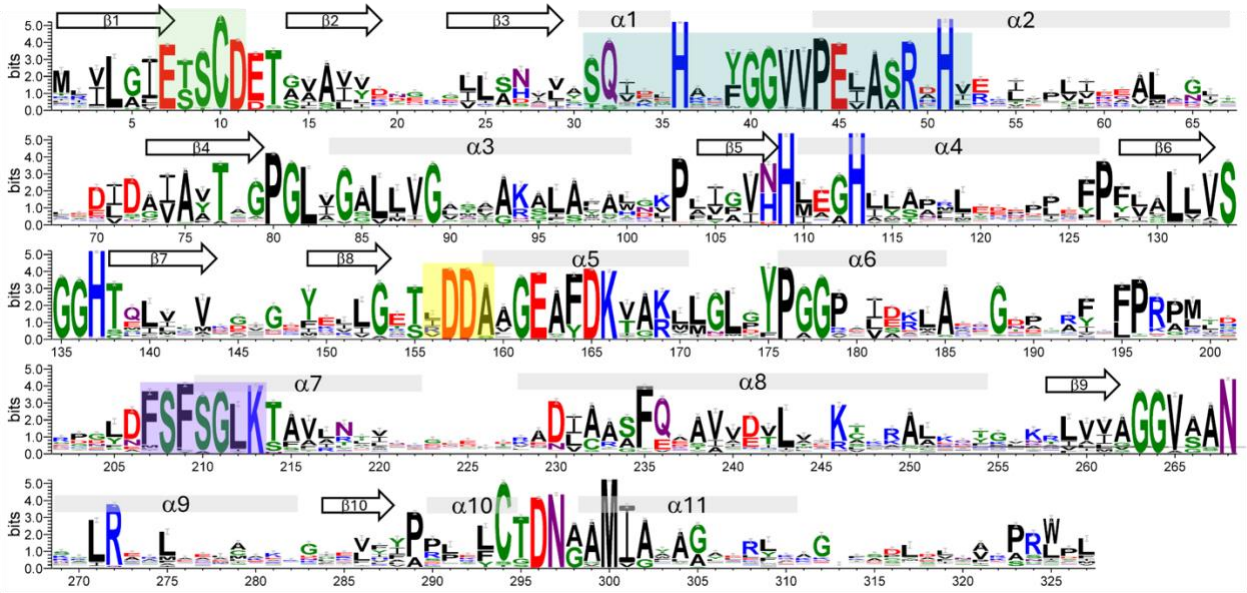

Supplementary figure 3-6: Sequence logo of TsaD proteins derived from a structure-guided alignment of 540 reviewed TsaD sequences obtained from the Uniprot database.
Position numbers correspond to residue numbers in *T. maritima* TsaD. Secondary structure elements derived from *Tm*TsaD in the present structure are indicated. Colored shades: green, E_{7}-S/T-SCD_{11} motif; teal, α1-α2 helical hairpin; yellow, $h_{156}DDs_{159}$ motif (h=hydrophobic, s=small residue); purple, $F_{207}SFSGLK_{213}$ motif. Red stars: A37 pocket. Blue stars: positive residues stabilizing backbone phosphates. Cyan stars: zinc binding. Black stars: TC-AMP binding. Letter color code: polar: green; neutral: purple; basic: blue; acidic: red; hydrophobic: black. The overall height of the stack indicates the sequence conservation at that position, while the height of symbols within the stack indicates the relative frequency of each residue at that position. Error bars indicate an approximate Bayesian 95% confidence interval.

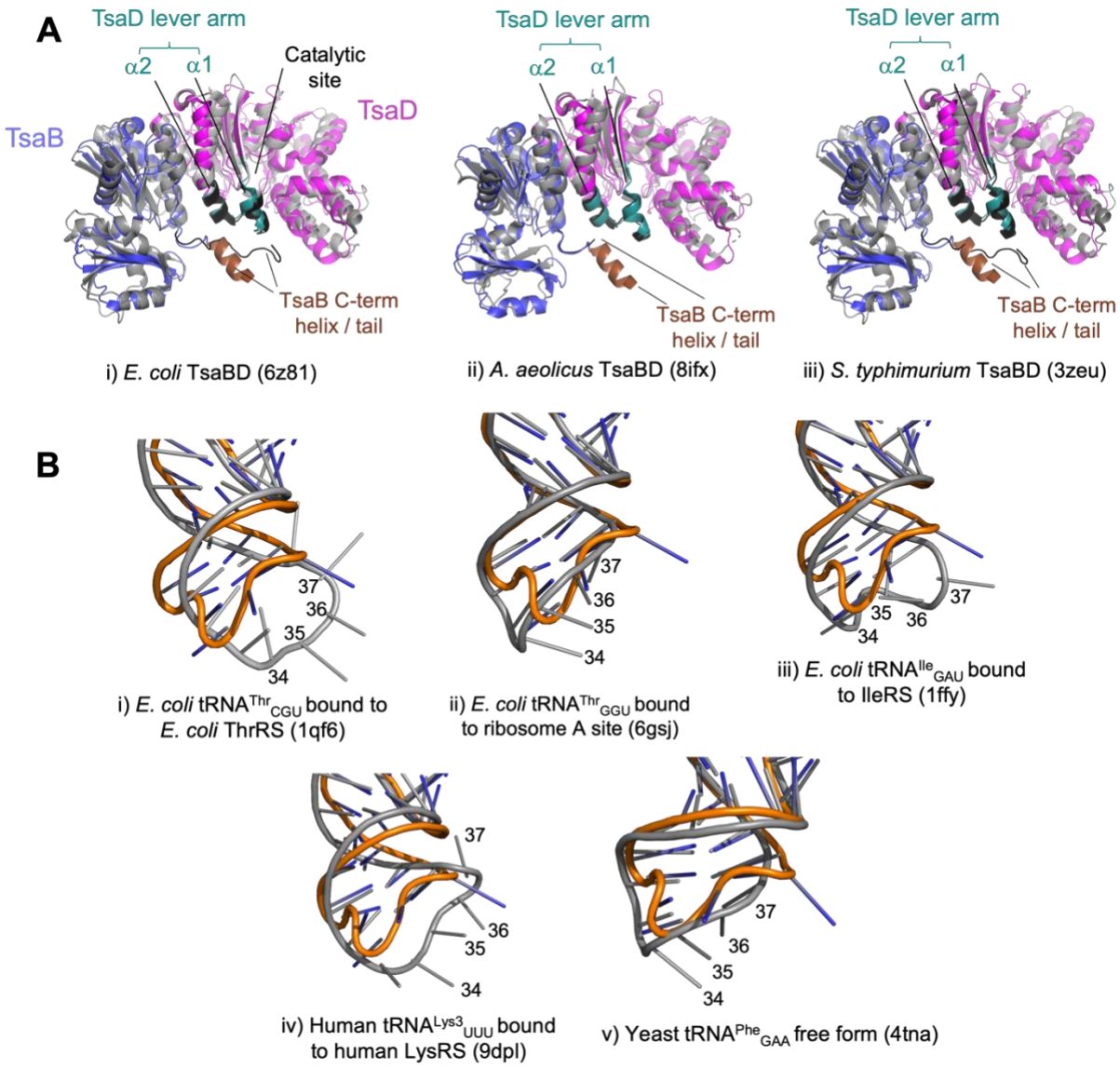

Supplementary figure 3-7: Comparisons.
A) Comparison of the *Tm*TsaBD protomer in the tRNA-bound state (present structures, colored, for clarity the tRNA is not shown) and in other apo TsaBD structures *(*in grey) showing the shared closed conformation of the lever arm of TsaD (teal and black, respectively), and the ordering of the C-terminal tail of TsaB into a 3-turn helix in the tRNA-bound state. (i) *E. coli* TsaBD bound to inhibitor, (ii) *A. aeolicus* TsaBD bound to ADP, (iii) *S. typhimurium* TsaBD bound to ATPγS. **B)** Examples of comparisons of the anticodon loop conformation in *E. coli* $tRNA^{Thr}_{CGU}$ bound to *Tm*$TsaB_2D$ (orange) to loop conformation in other tRNA structures (grey). The comparison is with (i) the same tRNA bound to *E. coli* threonyl-tRNA synthetase, (ii) *E. coli* $tRNA^{Thr}_{GGU}$ bound to the ribosome A site (1), (iii) *E. coli* $tRNA^{Ile}_{GAU}$ bound to isoleucyl-tRNA synthetase (2), iv) human cellular modified $tRNA^{Lys3}_{UUU}$ bound to human lysyl-tRNA synthetase (3), and v) unbound yeast $tRNA^{Phe}_{GAA}$ (4). Nucleotides 34-37 are labeled, and PDB IDs are in parentheses.

Supplementary figure 3-8: Remodeling of the anticodon loop in the *Tm*TsaB$_2$D/*Tm*tRNA$^{Lys}_{CUU}$ structure and flipping of A37 into the active site.
Color code for protein: Magenta, TsaD; teal, TsaD α1-α2 helical hairpin; blue, TsaB; brown, TsaB C-terminal helix. All distances consistent with hydrogen bonding interactions with the tRNA are < 3.3 Å (black dashed lines). **A)** Unsharpened cryo-EM map and fitted model of the anticodon loop. The local map resolution is 3.5-3.7 Å at nucleotides 32-38. Left: view of the anticodon loop from the major groove side showing the zigzag pattern of bases. Right: view illustrating bending of the anticodon loop toward the major groove of the anticodon stem. **B)** Residues of the hydrophobic trough, accommodating the U32–U36•A38 base triple and basic residues interacting with the triple's phospho-ribose backbone. The enzyme subunit contributing each residue is indicated in parentheses in the residue label. For clarity, only nucleotides of the base triple are displayed in stick model, and the intervening RNA backbone as a ribbon. The local resolution of the cryo-EM map in this region is approximately 3.5-3.7Å for TsaB residues, and 3.3-3.5 Å for TsaD residues. Red dashed lines highlight the geometry of the hydrogen bonding network within the base triple. **C)** The RNA backbone around A37 and the compacted phosphates of A38 and A26, stabilized by TsaD-Lys166. C25 is at the base of the D-stem. Dashed lines highlight interactions with distances <3.2 Å. **D)** Flipped-out conformation of C34 and base stacking of U33 and U35. **E)** Residues lining the shallow hydrophobic binding pocket for the tRNA wobble base C34. Interactions consistent with hydrogen bonding are shown as dashed line. All pocket residues are from TsaB. Local resolution range in this region is 3.28-3.53 Å. **F)** The shallow surface pocket for U35, and its stacking with U33. The local resolution in this region is 3.50 Å. Panels B-F display a DeepEMhancer-sharpened map.

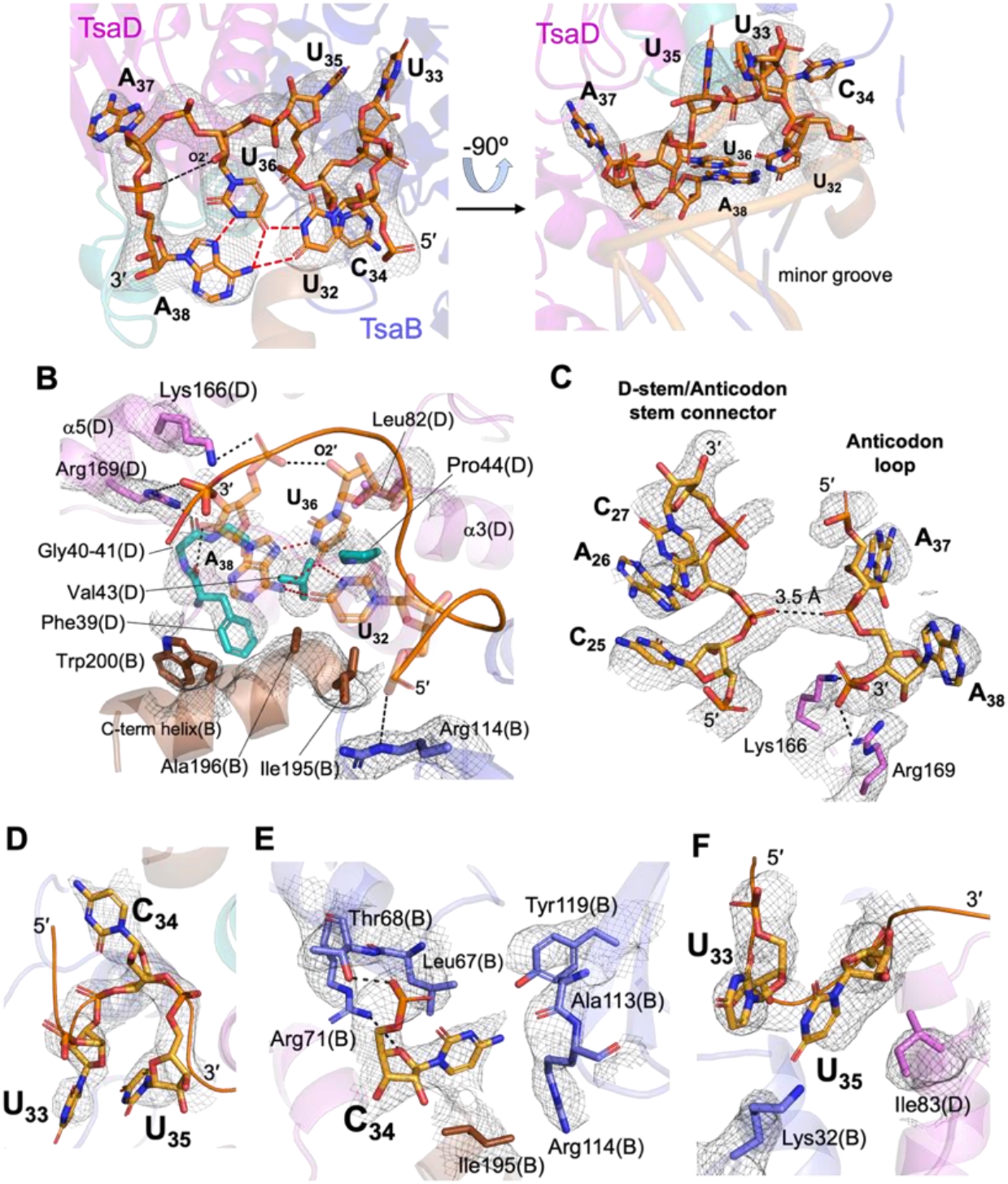
TsaD
A37
U35
U33
O2′
U36
5′
3′
C34
U32
A38
TsaB
-90°
TsaD
U35
U33
A37
C34
U36
U32
A38
minor groove
B
Lys166(D)
α5(D)
Leu82(D)
O2′
Arg169(D)
Pro44(D)
3′
U36
α3(D)
Gly40-41(D)
A38
Val43(D)
Phe39(D)
U32
Trp200(B)
5′
C-term helix(B)
Arg114(B)
Ala196(B)
Ile195(B)
C
D-stem/Anticodon
stem connector
Anticodon
loop
3′
5′
C27
A37
A26
3.5 Å
C25
3′
A38
5′
Lys166
Arg169
D
C34
5′
3′
U33
U35
E
Thr68(B)
Tyr119(B)
Leu67(B)
Ala113(B)
Arg71(B)
C34
Arg114(B)
Ile195(B)
F
5′
3′
U33
U35
Ile83(D)
Lys32(B)

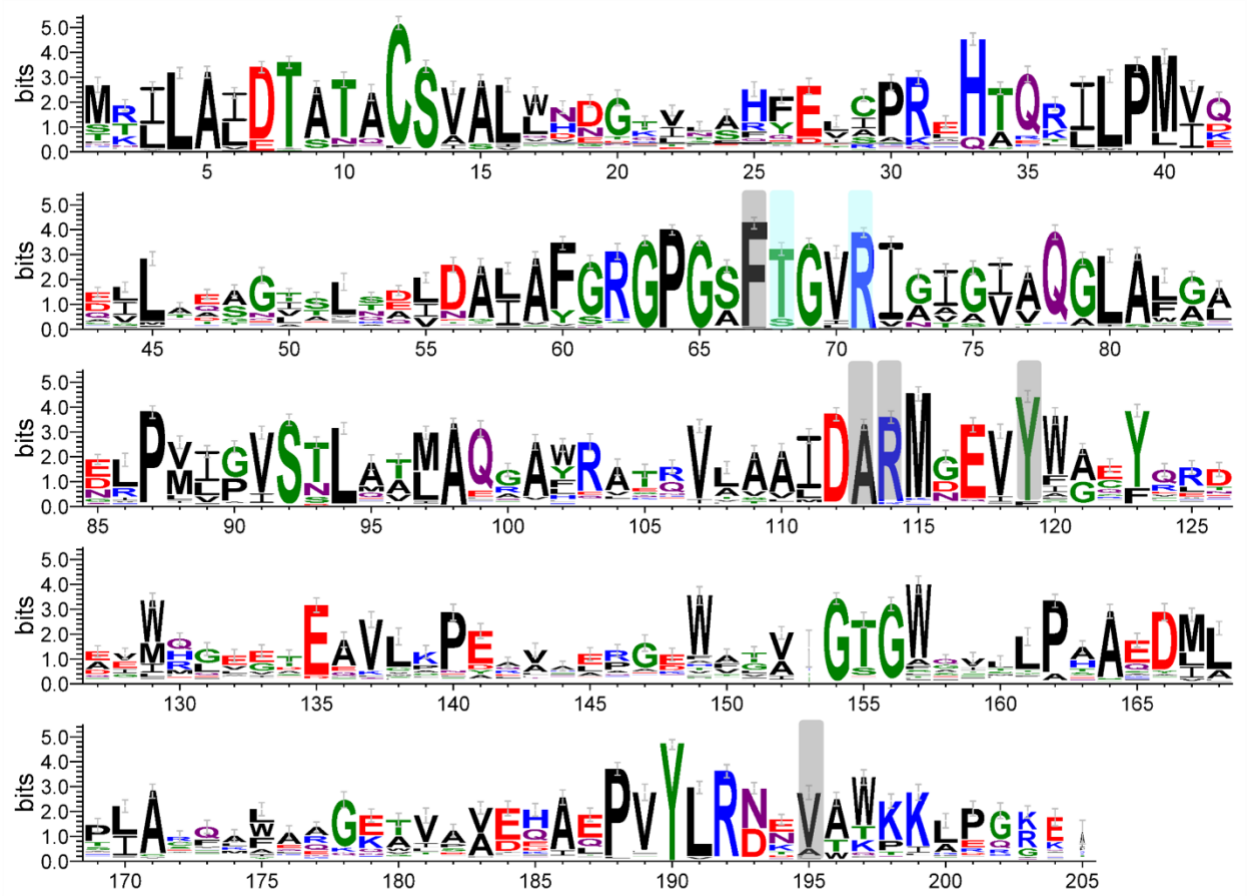

Supplementary figure 3-9: Sequence logo of TsaB derived from a structure-guided alignment of 550 reviewed TsaB sequences obtained from the Uniprot database.
Position numbers correspond to residue numbers in *T. maritima* TsaB. Colored shades: Grey, binding pocket for C34 base; cyan, residues interacting with C34 backbone. Letter color code: polar: green; neutral: purple; basic: blue; acidic: red; hydrophobic: black. The overall height of the stack indicates the sequence conservation at that position, while the height of symbols within the stack indicates the relative frequency of each nucleotide at that position. The width of the stack is proportional to the fraction of valid symbols in that position. Error bars indicate an approximate Bayesian 95% confidence interval.

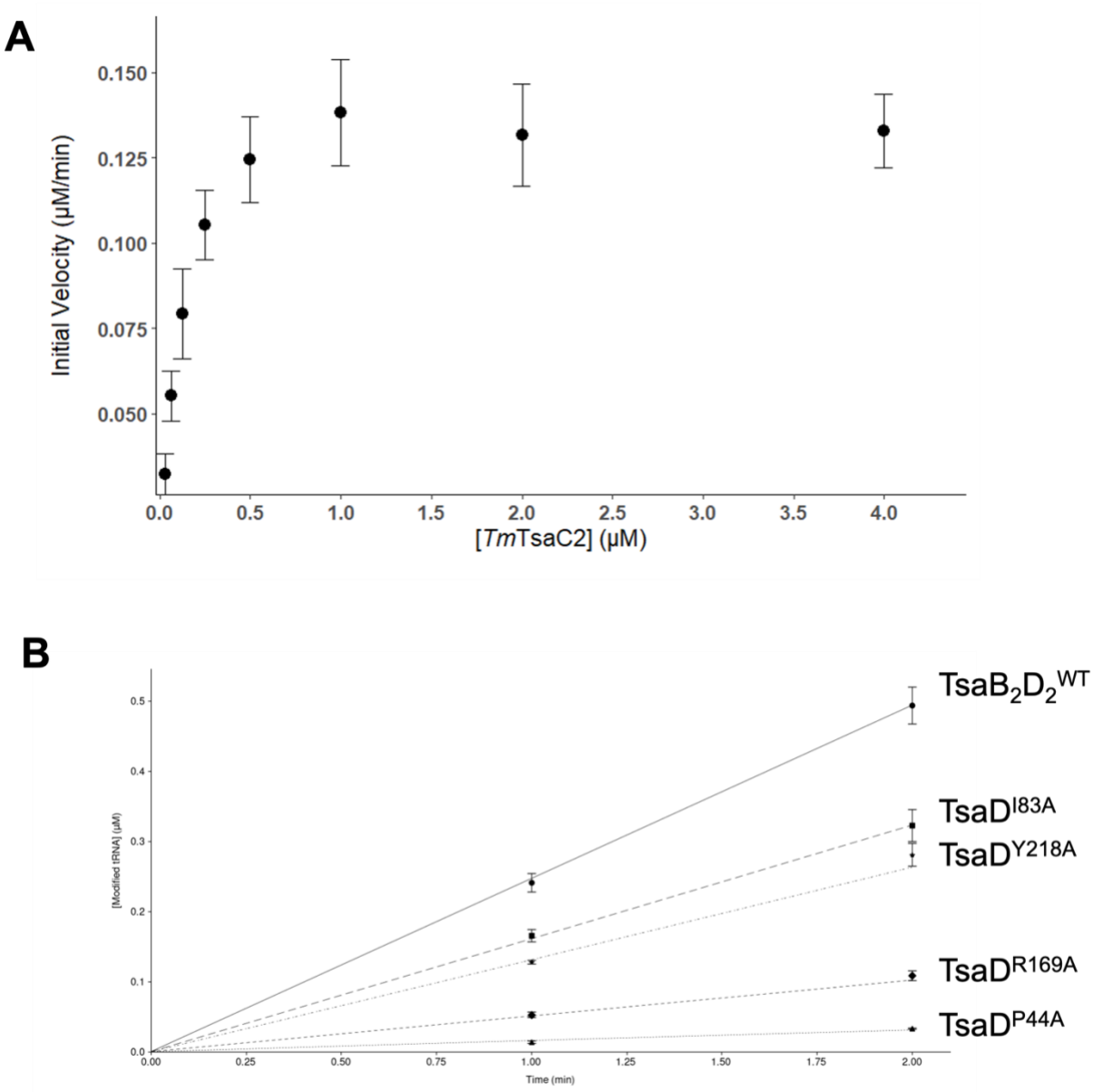

Supplementary figure 3-10: A) Determination of *Tm*TsaC2 concentration at which *Tm*TCT kinetics dominate. Standard t^6A radiochemical incorporation assays with *Ec*$tRNA^{Thr}_{CGU}$ transcript and varied *Tm*TsaC2 concentration of 0.031, 0.063, 0.13, 0.25, 0.50, 1.0, 2.0, 4.0 μM. **B)** Examples of time-course activity assays conducted under initial velocity conditions from which initial velocities were calculated.

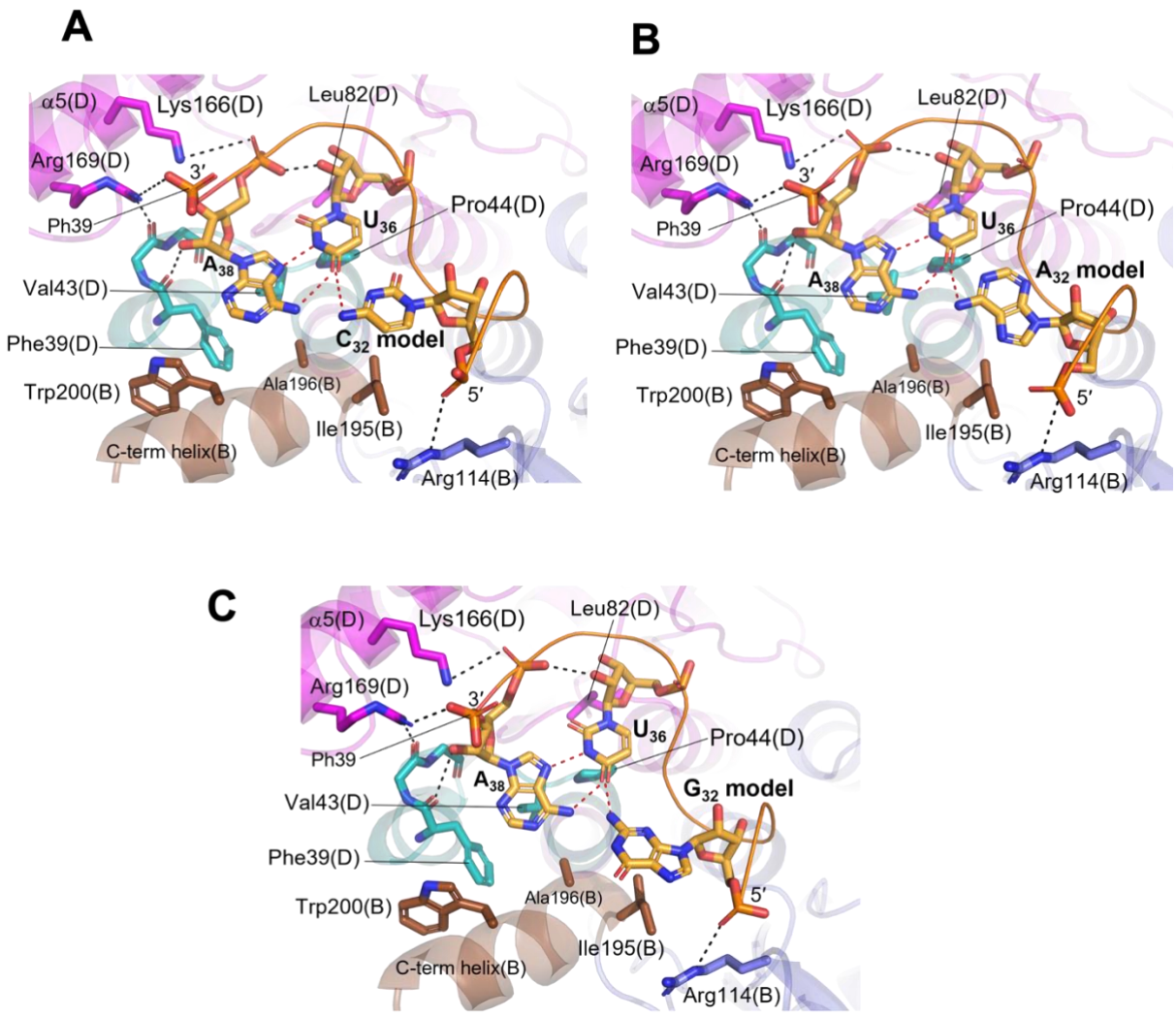

Supplementary figure 3-11: Modeling of C, A and G at position 32 in the anticodon loop of *Ec*tRNA$^{Thr}_{CGU}$.

A) C32 in a C32–U36•A38 triple in a cWH-cWH configuration. **B)** A32 in a A32–U36•A38 triple in a cWH-cWH configuration. **C)** Even G32, which does not naturally occur in bacterial t^{6}A tRNAs and is very rare in tRNA in general, can be accommodated in a G32–U36•A38 triple in a cSH-cWH configuration.

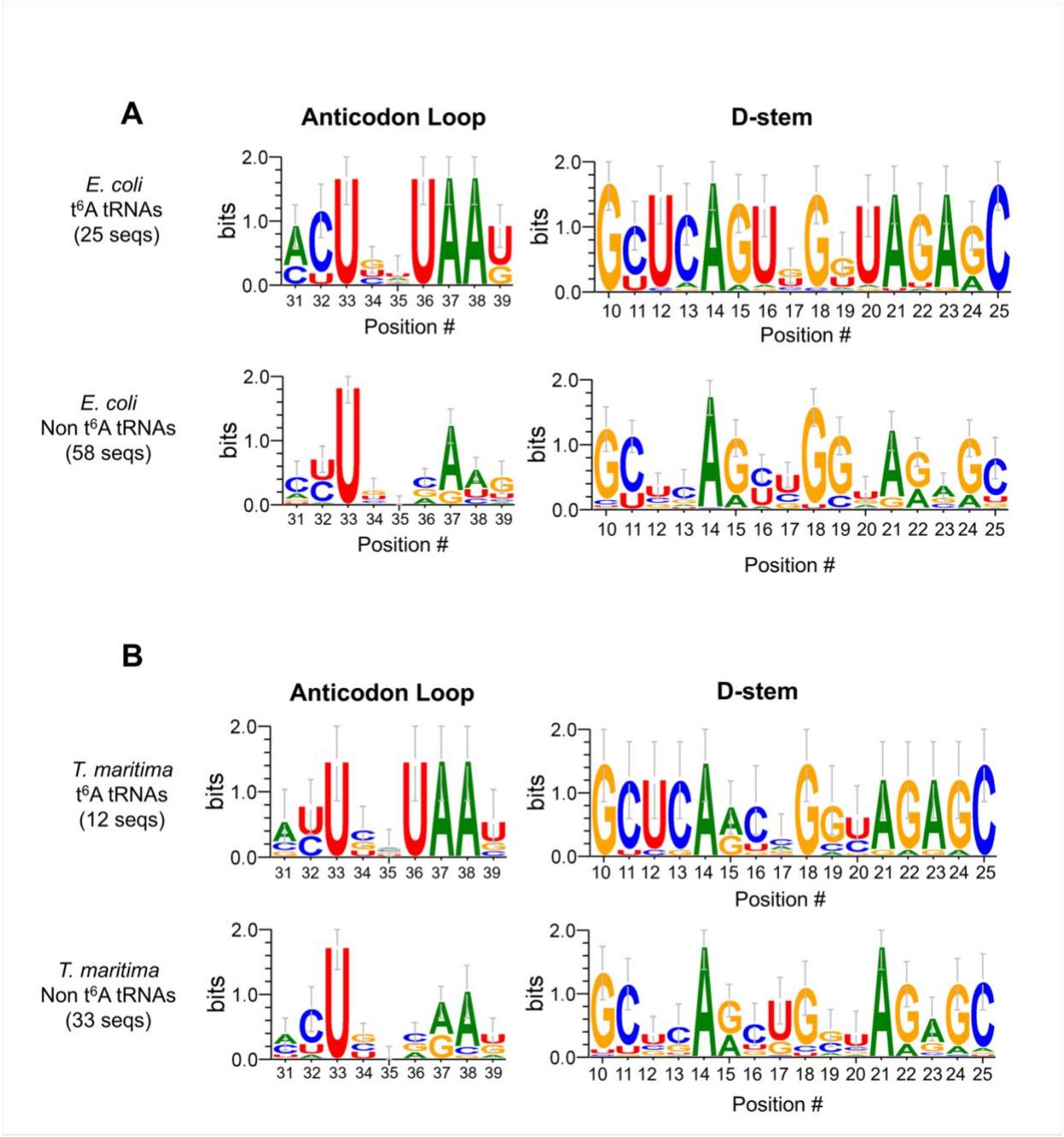

Supplementary figure 3-12: Sequence logo for the anticodon loop and D-stem regions of t^6A tRNAs versus non t^6A tRNAs from A) *E. coli* and B) *T. maritima*.

Amino Acid	ANN codon	Decoding 34-NNU-36 anticodon	Count in sequence analysis	Comment
Arg	AGG	CCU	336	
Arg	AGA	UCU	380	
Asn	AA**U**	**A**UU	1	Decoded by tRNAAsn-**G**UU via wobble pairing.
Asn	AAC	GUU	390	
Ile	AU**U**	**A**AU	2	Decoded by tRNAIle-**G**AU via wobble pairing.
Ile	AUC	GAU	340	
Ile	AUA	UAU	9	Rare codon. Decoded by tRNAIle-CAU where C is modified to lysidine.
Lys	AAG	CUU	262	
Lys	AAA	UUU	370	
Met	AUG	CAU	218	
Ser	AG**U**	**A**CU	0	Rare codon. Decoded by tRNASer-**G**CU via wobble pairing, except in few organisms.
Ser	AGC	GCU	318	
Thr	AC**U**	**A**GU	9	Rare codon.
Thr	ACG	CGU	331	
Thr	ACC	GGU	345	
Thr	ACA	UGU	394	
		Total	3705	

Supplementary figure 3-13: Abundances of the different NNU anticodons in a sample of 3705 bacterial t^6A substrate tRNAs (ANN-decoding tRNAs) used to generate the sequence conservation logo in Figure 4D. N is G, C, A or U. The ANN codon, corresponding NNU anticodon and number of sequences representing each anticodon are listed. The underrepresented codons are either rare or decoded by a represented tRNA. Position 34 in t^6A substrate tRNAs is always U/G/C (see Figure 4D). There are almost no occurrences of A at position 34 in sequences of bacterial t^6A substrate tRNAs because ANU codons are either rare or decoded by tRNAs carrying GNU anticodons via G34•U3 wobble base pairing, or CNU anticodons in which C34 is modified to lysidine.

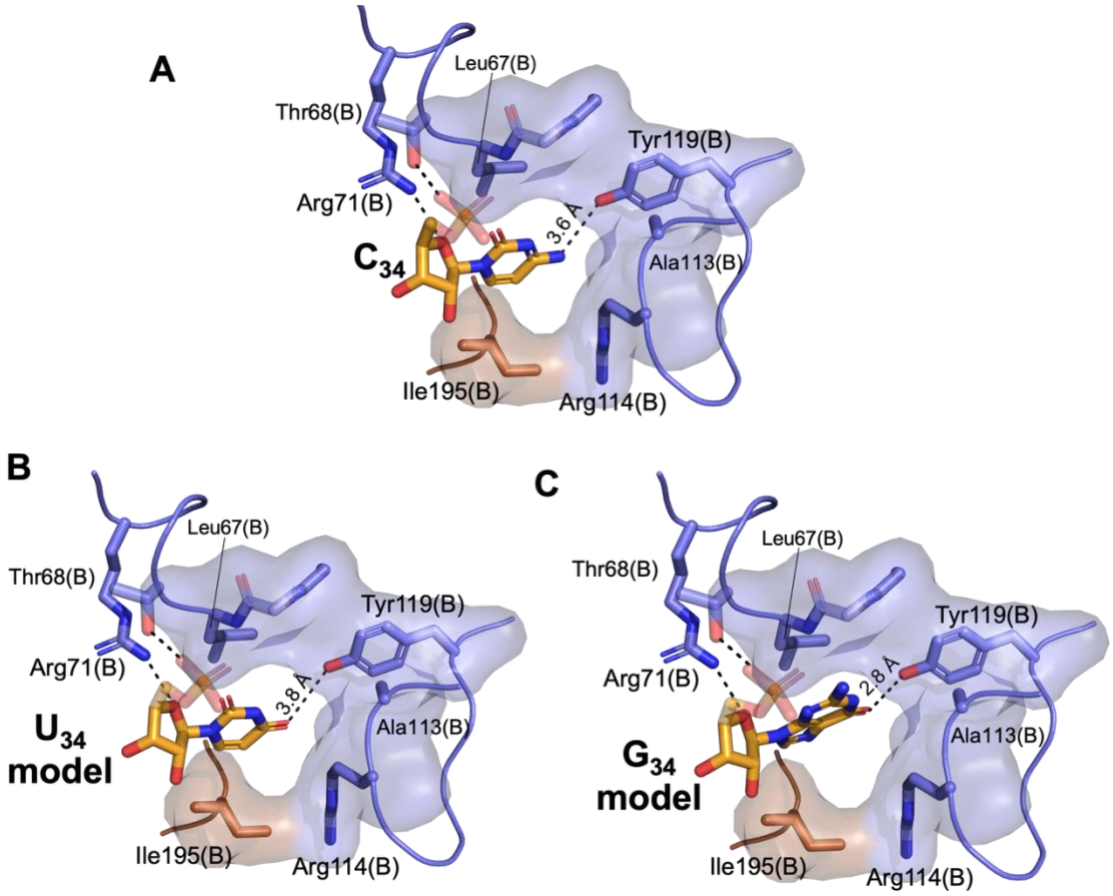

Supplementary figure 3-14: The pocket for binding the tRNA wobble base is shallow and large enough to accommodate the U34, C34 and G34 found in t^6A substrate tRNAs.
A) van der Waals surface representation of the hydrophobic binding pocket on TsaB for C34 as observed in the present cryo-EM structures. The two contacts with the sugar-phosphate backbone, and potential (water-mediated) hydrogen bond of TsaB-Tyr119 with the nucleobase are shown. **B and C)** Docking models of U and G in the C34 binding pocket, illustrating possible accommodation of U34 or G34 through similar interactions. The docking was performed onto the cryo-EM model of the *Tm*TsaB$_2$D/*Ec*tRNA$^{Thr}_{CGU}$ structure.

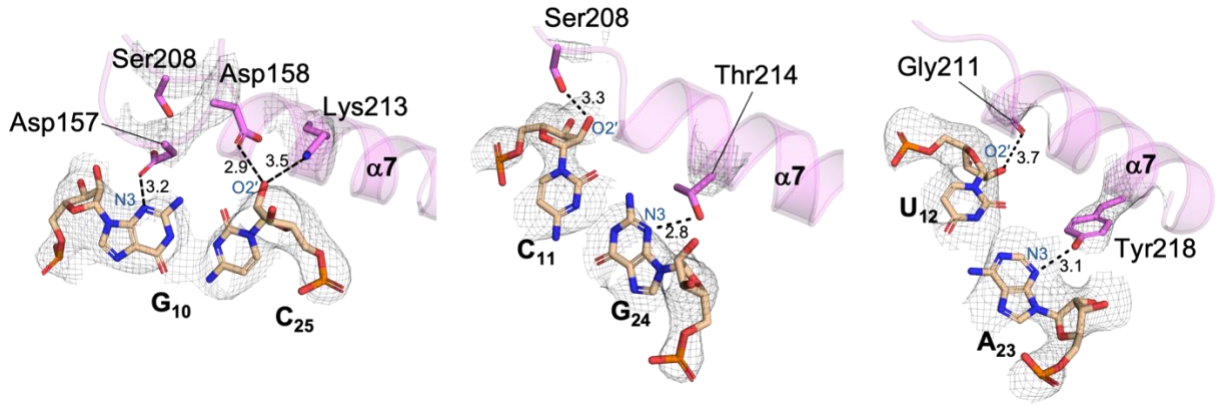

Supplementary figure 3-15: D-stem recognition in *Tm*tRNA$^{Lys}_{CUU}$-bound *Tm*TsaB$_2$D. Unsharpened cryo-EM map and fitted model of individual D-stem base pairs and interacting TsaD side chains. The map local resolution in this region is 3.34-3.58 Å. Dashed lines highlight hydrogen bonding networks with distances in Å.

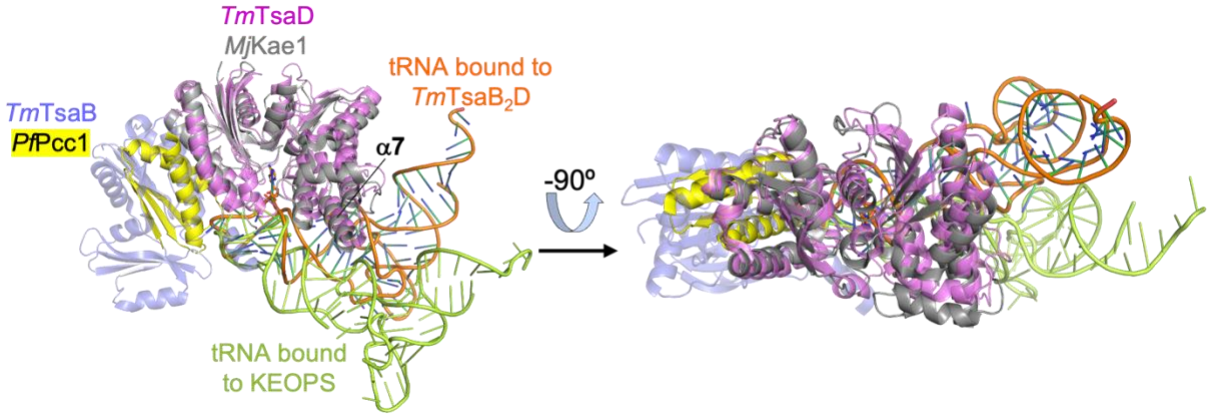

Supplementary figure 3-16: Comparison of the positioning of tRNA at the TsaB/TsaD interface in the *Tm*TsaB$_2$D/*Ec*tRNA$^{Thr}_{CGU}$ complex to its position at the Kae1/Pcc1 interface in archaeal KEOPS (PDB ID 8up5). For clarity, the Bud32 and Cgi121 subunits of KEOPS are not shown.

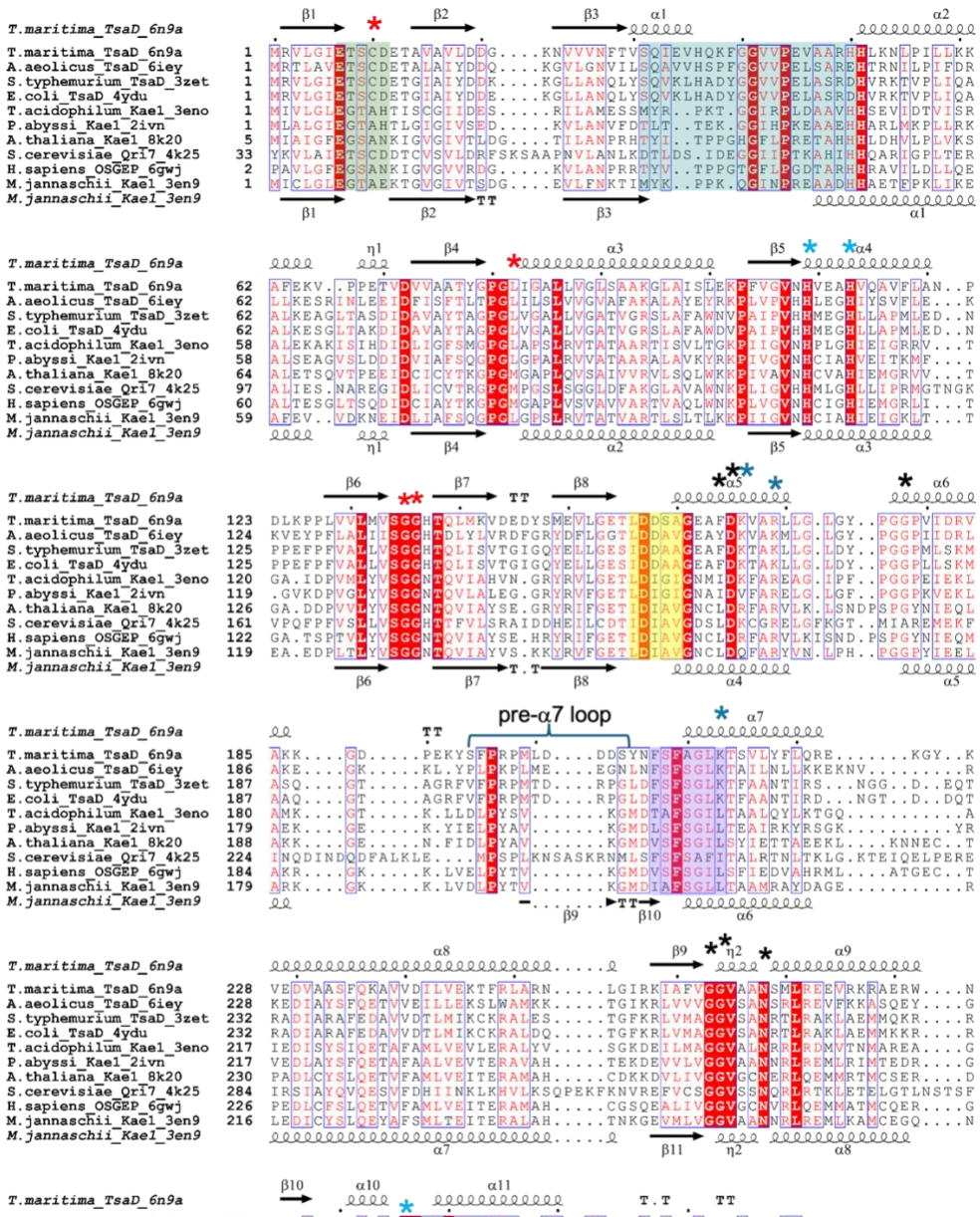

Supplementary figure 3-17: Structure-based multisequence alignment of characterized TsaD, Kae1, OSGEP and Qri7 proteins.
PDB IDs of the aligned structures are indicated in the sequence names. Invariant and conserved residues are highlighted in red background and red font, respectively. Colored highlights: green, E_7-S/T-SCD_{11} motif; teal, α1-α2 helical hairpin; yellow, $h_{156}DDs_{159}$ motif (h=hydrophobic, s=small residue); purple, $F_{207}SFSGLK_{213}$ motif; bracket, pre-α7 loop (Ser194-Ser204). Red stars: A37 pocket. Blue stars: positive residues stabilizing backbone phosphates. Cyan stars: zinc binding. Black stars: TC-AMP binding.

Supplementary table 3-1: Cryo-EM data collection and processing, and model refinement and validation statistics.

Structure	*Tm*TsaB$_2$D bound to *in vivo* *Ec*tRNA$^{Thr}_{CGU}$	*Tm*TsaB$_2$D bound to synthetic *Tm*tRNA$^{Lys}_{CUU}$
Deposition IDs: PDB, EMDB, EMPIAR	pdb_000013fn, EMD-77046, EMPIAR-13544	pdb_000013fo, EMD-77048, EMPIAR-13543
Data collection		
Microscope	Titan Krios	Titan Krios
Detector	Falcon 4i DED	Falcon 4i DED
Data Collection Software	SerialEM	SerialEM
Magnification	105,000	105,000
Voltage (kV)	300	300
Electron exposure ($e^-/Å^2$)	50	50
Defocus range (μm)	-0.8 to -2.2	-0.8 to -2.2
Pixel size (Å)	0.8266	0.8266
Tilt angle (°)	37	37
No. of movies	9,495	8,646
Cryo-EM data processing		
Data processing software	cryoSPARC v4.7.1	cryoSPARC v4.7.1
No. of micrographs	4,207	2,506
Initial particle images	401,971	535,379 (blob picker) 376,761 (template picker)
Final particle images	323,313	63,799
Symmetry imposed	C1	C1
Map resolution (FSC 0.143)	3.2 Å	3.2 Å
Resolution range	3.09 to 3.76	3.13 to 4.17
Map sharpening B factor	-142	-124
Structural refinement		
Initial model used (PDB)	6N9A (protein),1QF6 (tRNA)	6N9A (protein)
<u>Model composition</u>		
Non-hydrogen atoms	7,142	7,173
Protein residues	724	724
Nucleotides	71	73
Metal ions	1	0
<u>R.m.s. deviations</u>		
Bong lengths (Å)	0.003	0.004
Bond angles (°)	0.677	0.643
<u>Validation</u>		
MolProbity score	2.00	1.96
Clashscore	10.42	10.09
Rotamer outliers (%)	0	0
<u>Ramachandran Plot</u>		
Favored (%)	92.76	93.31
Allowed (%)	7.24	6.69
Outliers (%)	0	0

Supplementary table 3-2: Primers used for generating point mutations in *Tm*TsaD and *Tm*TsaB. The mutagenic triplets are shown in lowercase.

Mutation	**Primer**	**Sequence (5′-3′)**
TsaD-C10A	F	AGAAACGTCCgcgGATGAAACGGC
	R	ATTCCAAGAACTCTCATAAC
TsaD-F39A	F	CCACCAGAAGgcgGGAGGGGTGG
	R	ACCTCTATCTGAGAAACTG
TsaD-P44G	F	AGGGGTGGTGggcGAAGTGGCGG
	R	CCAAACTTCTGGTGGAC
TsaD-P44A	F	AGGGGTGGTGgcgGAAGTGGCGG
	R	CCAAACTTCTGGTGGACCTCTATCTG
TsaD-L82A	F	TGGACCTGGCgcgATCGGTGCCC
	R	TAGGTGGCCGCAACG
TsaD-I83N	F	ACCTGGCCTAaacGGTGCCCTCC
	R	CCATAGGTGGCCGCAACG
TsaD-I83A	F	ACCTGGCCTAgcgGGTGCCCTCC
	R	CCATAGGTGGCCGCA
TsaD-D157A	F	TGAAACGCTCgcgGATTCGGCGG
	R	CCCAGCACTTCCATGG
TsaD-D158A	F	AACGCTCGATgcgTCGGCGGGGG
	R	TCACCCAGCACTTCCATG
TsaD-E162A	F	TTCGGCGGGGgcgGCATTCGATA
	R	TCATCGAGCGTTTCACCCAGC
TsaD-R169A	F	TAAGGTGGCTgcgCTCCTCGGACTC
	R	TCGAATGCCTCCCCC

Supplementary table 3-2: Primers used for generating point mutations in *Tm*TsaD and *Tm*TsaB, continued. The mutagenic triplets are shown in lowercase.

Mutation	**Primer**	**Sequence (5′-3′)**
TsaD-S208A	F	TTACAACTTCgcgTTTGCGGGTTTGAAG
	R	CTGTCATCATCCAGC
TsaD-T214A	F	GGGTTTGAAGgcaTCTGTCCTCTATTTC
	R	GCAAAGCTGAAGTTGTAAC
TsaD-Y218A	F	TTCTGTCCTCgcgTTCCTCCAGAGGG
	R	GTCTTCAAACCCGCAAAG
TsaB-T68A	F	TGGAGGATTGgcgGGTCTCAGGG
	R	GGGCCAATTCCCACTC
TsaB-R114A	F	TAGAAGAGCGgcgAAAGGTTACC
	R	GCCACGAGTACAACAC
TsaB-Y119A	F	AGGTTACCACgcgTGTGCGGTTTATC
	R	TTCCTCGCTCTTCTAG
TsaB-I195A	F	TCAGAAATCCgcgGCGGAATTGAACTG
	R	AGATACAAAGGTTCGATTTC
TsaB-W200A	F	GGAATTGAACgcgGAAAAAAAGAAAAGGG
	R	GCTATGGATTTCTGAAGATAC

3.6. Acknowledgements

Chapter 3, in part is a reprint of the material as it appears in Kutchuashvili, A., Scheleen, E., Guynes, G., Wu, J., Chan, C.K., Dedon, P., Iwata-Reuyl, D. and Swairjo, M.A., 2026. Anticodon loop remodeling and D-stem shape drive the specific recognition of ANN-decoding tRNAs for t^6A modification. *Nucleic Acids Research*, *54*(11), p.gkag599. The dissertation author was the first author of this paper.

Chapter 4: Conclusions and future directions

4.1. Conclusions

The data presented here address longstanding questions concerning both steps of the t^6A biosynthesis pathway. Specifically, this work examines two outstanding mechanistic questions: i) does synthesis of the pathway intermediate TC-AMP by TsaC/TsaC2 proceed through the proposed N-carboxy-L-threonine intermediate? and ii) how does the TsaD/TsaB complex recognize and selectively modify ANN-decoding tRNAs?

Time- and pH-dependent soaking of *Tm*TsaC2 crystals captured substrate-, intermediate-, and product-bound states of the enzyme. The *Tm*TsaC2/CT/ATP structure provides direct evidence for N-carboxy-L-threonine as a reaction intermediate for TsaC2 enzymes, supporting a mechanism where L-threonine first reacts with CO_2 to form N-carboxy-L-threonine, which then attacks ATP to generate TC-AMP and pyrophosphate. SEC-SAXS analysis shows that the relative orientation of the catalytic TsaC domain and the SU5 domain of TsaC2 is dynamic in solution. Upon substrate binding, the enzyme adopts the closed, catalytically competent conformation observed in the crystal structures. Structural and mutagenesis data further identify an interdomain salt bridge that is critical for catalysis, likely by contributing to stabilization of the closed conformation.

Cryo-EM structures of the *Tm*$TsaB_2D_2$ bound to two distinct tRNA substrates reveal that the bacterial t^6A synthase recognizes substrate tRNAs mainly through an indirect readout mechanism. These structures show that productive tRNA binding requires extensive remodeling of the anticodon loop, largely mediated by formation of a U36-A38-U32 base triple within the anticodon loop. Remarkably, the main t^6A determinants, U36 and A38, do not engage in any base-specific interactions with the enzyme. Additionally, although contacts with the tRNA D-stem are essential for substrate recognition and catalysis, they too rely on indirect readout of the

D-stem shape rather than direct readout of specific base pairs. These structures provide the first view of the tRNA-bound t^6A synthase in which the tRNA anticodon loop is fully resolved, revealing for the first time how U36 and A38 are accommodated by the enzyme. Because U36 and A38 are universal determinants of t^6A modification, and because the overall architecture of the bacterial TsaD/TsaB complex is conserved in the Kae1/Pcc1 core of the archaeal and eukaryotic KEOPS complex, the mode of recognition of tRNA identity described here may be broadly conserved. Whether the same mechanism applies to the mitochondrial t^6A synthase Qri7, which lacks a TsaB ortholog and functions as a homodimer, remains less clear.

The structures also reveal bacterial-specific features of the TsaD/TsaB interface that contribute to productive binding of tRNA. These features may provide opportunities for selective inhibition. Thus, the structures presented here not only clarify how bacterial t^6A enzymes recognize substrate tRNAs but also identify bacteria-specific protein-RNA interactions that may inform future efforts to develop antimicrobial drugs targeting t^6A biosynthesis.

4.2. Future directions

4.2.1. TC-AMP channeling

Because the pathway intermediate TC-AMP is unstable in solution, it has been proposed that TC-AMP may be channeled from TsaC/TsaC2 to TsaD. To test this possibility, our collaborators performed a two-chamber dialysis experiment in which only small molecules could freely diffuse between chambers (prof. Dirk Iwata-Reuyl and Erik Schleen, Portland State University). Reactions were carried out in 100 mM Tris, pH 7.5, 300 mM KCl, 5 mM DTT, 2 mM ATP, 20 mM $MgCl_2$, 20 µM *Tm*$tRNA^{Thr}$CGU transcript, 10 mM $NaHCO_3$, and 250 µM L-[^{14}C]-threonine (50 µCi/µmol). One chamber contained 20 µM *Ec*TsaC, while the second

chamber contained 10 μM each TsaB, TsaD, and TsaE from either *T. maritima* or *E. coli* (here named the threonylcarbamoyl-transfer chamber or TC-transfer chamber).

This experiment showed that TC-AMP generated by *Ec*TsaC in the first chamber supported t^6A formation when *Ec*TsaBDE, but not when *Tm*TsaBDE, was present in the TC-transfer chamber. These results show that *Ec*TsaC-generated TC-AMP can diffuse between chambers but is used productively only by the *E. coli* TC-transfer system. For the *T. maritima* t^6A biosynthesis system, t^6A formation required the presence of active, full-length *Tm*TsaC2 in the same chamber as *Tm*TsaBDE, whereas isolated *Tm*TsaC2 domains or the inactive Ser144Ala *Tm*TsaC2 mutant did not support t^6A synthesis. These observations suggest that TC-AMP transfer in the *T. maritima* system may require a physical contact between *Tm*TsaC2 and *Tm*TsaBDE, consistent with substrate channeling.

To explore a potential channeling interface in the *T. maritima* system, a docking model was generated based on the *E. coli* HypF enzyme (134). HypF contains TsaC-like and TsaD-like domains that interact face-to-face and catalyze carbamoyladenylate synthesis and carbamoyl transfer reactions in pathways unrelated to t^6A synthesis (Fig. 4.1B). Docking the catalytic domain of *Tm*TsaC2 onto the TsaD subunit from the crystal structure of *Tm*$TsaB_2D_2E_2$ resulted in severe steric clashes with the TsaD lever arm, which adopts an "up" conformation upon TsaE binding (Fig. 4.1C, right). In contrast, the cryo-EM structure of *Tm*$TsaB_2D_2$ bound to tRNA shows the TsaD lever arm in a "down" position, which allows TsaC2 docking without clashes (Fig. 4.1C, left). These models suggest that TsaE and TsaC2 cannot bind TsaD simultaneously, whereas TsaC2 and tRNA could potentially interact with the $TsaB_2D_2$ platform at the same time. Such an arrangement could provide a structural understanding of TC-AMP channeling from *Tm*TsaC2 to *Tm*TsaD.

The TsaC2/TsaD docking model generated in the presence of tRNA revealed a putative enclosed path between the TsaC2 catalytic domain and the TsaD active site. This proposed channel is lined with highly conserved hydrophobic residues, which could protect TC-AMP from solvent-mediated hydrolysis, as well as basic residues that could stabilize the phosphate moiety of TC-AMP during channeling (Fig. 4.1D). Because the interaction between TsaC2 and TsaD is transient, a stable TsaC2/TsaD complex has been difficult to isolate biochemically (53), precluding structural studies. Instead, I tested the proposed channeling model using site-directed mutagenesis and t^6A biosynthesis assays. Residues predicted to line the putative channel, but located away from the active sites of either enzyme, were targeted for mutagenesis. Small hydrophobic residues were replaced with bulkier residues, such as phenylalanine or tyrosine, to sterically obstruct the proposed channel, whereas basic residues were replaced with neutral or acidic residues, such as glutamine or glutamate, to disrupt potential electrostatic stabilization of TC-AMP in the channel.

However, none of these mutations, including double mutants, reduced t^6A biosynthesis activity. These results suggest that either TC-AMP is channeled through a different route, or the proposed TsaC2/TsaD docking model does not accurately describe the channel. It is also possible that the channeling interface is dynamic, or dependent on transient conformational states that are not captured by the static docking model.

Future studies will be needed to identify the location and nature of the TsaC2/TsaD interaction interface. Two-dimensional NMR could be used to map chemical shift perturbations upon formation of a transient TsaC2/TCT complex, thereby identifying residues involved in interactions. Additionally, cross-linking coupled to liquid chromatography–mass spectrometry could help define the location and orientation of TsaC2 on the TCT complex during catalysis.

However, both of these techniques can be challenging to optimize for this kind of complex biochemical system.

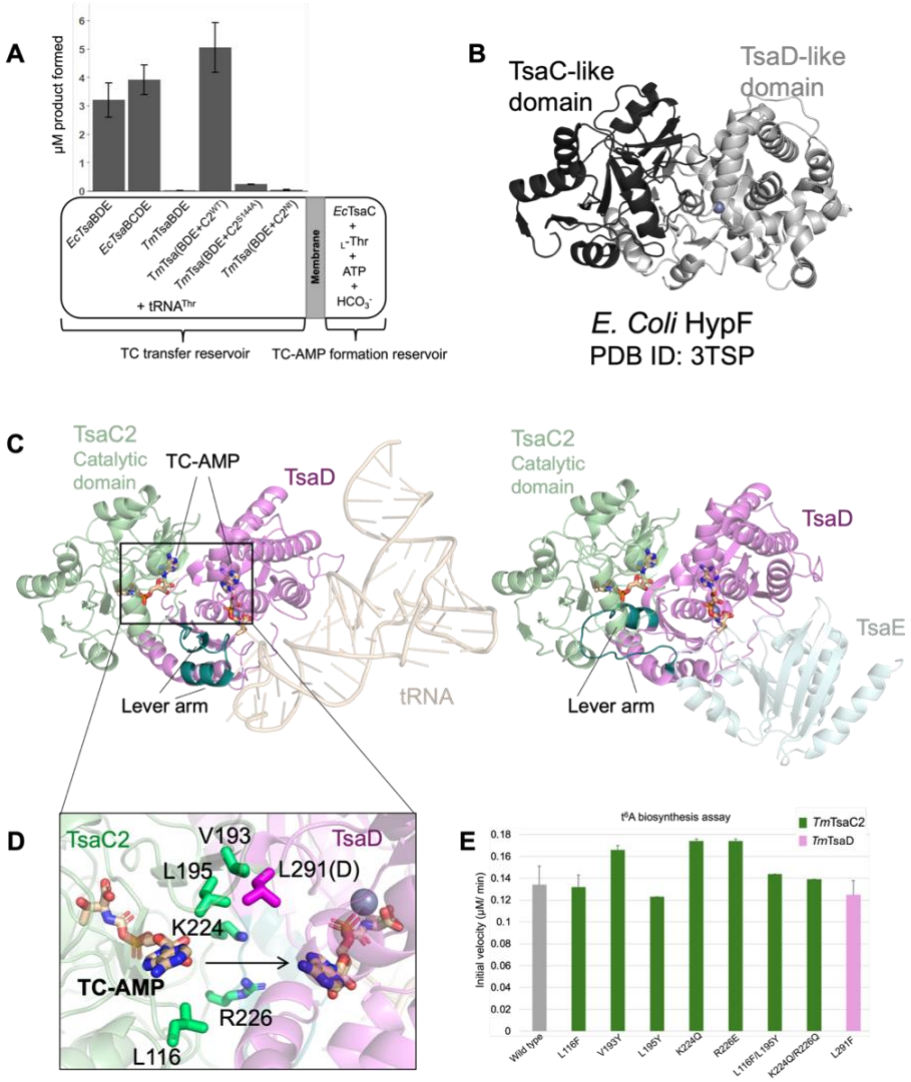

Figure 4-1: Preliminary investigations of the TC-AMP channeling hypothesis.
A) Channeling experiment performed in a dialysis cassette (unpublished data). **B)** Crystal structure of *E. coli* HypF, with its TsaC-like and TsaD-like domains shown in dark gray and light gray, respectively. **C)** Docking models of the catalytic domain of *Tm*TsaC2 onto the *Tm*TsaB$_2$D$_2$-tRNA cryo-EM structure (left), and onto the *Tm*TsaB$_2$D$_2$E$_2$ crystal structure (right). The TsaC/catalytic domain of *Tm*TsaC2 and the TsaD subunit in each model are positioned based on the orientations of the homologous domains in *E. coli* HypF. TsaD is shown in violet, TsaD lever arm in teal, *Tm*TsaC2 catalytic domain in green, tRNA in wheat, and TsaE in cyan. For clarity, the TsaB subunit is not displayed. The SUA5 domain of TsaC2 was not included in the model. **D)** Close-up view of the putative channel in the *Tm*TsaB$_2$D$_2$-tRNA-*Tm*TsaC2 docking model. **E)** t^{6}A biosynthesis activities of *Tm*TsaC2 and *Tm*TsaD mutants carrying site-directed mutations in the putative channel.

4.2.2. Investigating the nature of $TsaB_2D_2$ inactivation and TsaE-dependent reactivation by cryo-EM

Although the $TsaB_2D_2$–tRNA structure reveals how substrate tRNA is recognized, it does not address another major unresolved question in the t^6A field: the nature of the inactivation of $TsaB_2D_2$ following TC-transfer to tRNA, and the mechanism of its reactivation by TsaE-catalyzed ATP hydrolysis. Previous studies showed that *Tm*$TsaB_2D_2$ becomes inactive after one cycle of catalysis and releases the modified tRNA product in the absence of *Tm*TsaE, while TsaE and its ATPase activity are required for multiple turnovers of the catalytic cycle. However, the nature of $TsaB_2D_2$ inactivation and TsaE-dependent reactivation remains unclear. One possibility is that, after a single catalytic cycle, $TsaB_2D_2$ undergoes a conformational change and becomes trapped in an inactive state. TsaE binding and ATP hydrolysis may then restore the active conformation, allowing the complex to enter another catalytic cycle.

If inactivation and reactivation involve large conformational changes, cryo-EM should be well suited to investigate these states, especially since sample preparation and data collection strategies for this complex have already been optimized. One approach would be to generate the inactivated $TsaB_2D_2$ complex by incubating $TsaB_2D_2$ with TsaC2, Mg-ATP, L-threonine, bicarbonate, and an excess of substrate tRNA, ensuring that most $TsaB_2D_2$ complexes complete one catalytic cycle. This mixture could be directly applied to the grid. Alternatively, the resulting inactivated $TsaB_2D_2$ could be purified by SEC, and its inactivation verified using the t^6A biosynthesis assay conducted in the absence of TsaE. Inactive $TsaB_2D_2$ can then be subjected to cryo-EM analysis either alone or in complex with substrate tRNA following verification of tRNA binding by EMSA. To capture reactivation intermediates, the purified inactivated $TsaB_2D_2$ complex could be mixed with TsaE and ATP for a short time immediately before vitrification.

This approach may reveal transient conformational states associated with TsaE binding, ATP hydrolysis, and restoration of the active $TsaB_2D_2$ conformation.

4.2.3. Elucidating the TC-transfer reaction

Although my cryo-EM structures and docking model of TC-AMP in the TC-transfer site provide insight into the mechanism of TC transfer from TC-AMP onto A37 of tRNA, experimental validation of the proposed reaction mechanism is still needed. This could be addressed by determining a structure of *Tm*$TsaB_2D_2$ bound to synthetic $tRNA^{Lys}$ and BK951, a previously developed TC-AMP analog (122), which may help capture a substrate-bound or pre-transfer state of the $TsaB_2D_2$/tRNA complex.

4.3. Acknowledgements

In Chapter 4, Figure 4-1A is adapted from material currently being prepared for publication: Kutchuashvili, A., Wood, E., Scheleen, E., Luthra, A., Sankaran, B., Iwata-Reuyl, D., and Swairjo, M. A., "Structure–Function Analysis of the *Thermotoga maritima* t^6A Biosynthesis Enzyme TsaC2." The figure and the underlying data were generated by Erik Scheleen and Dirk Iwata-Reuyl.

References

1. Cardone G, Heymann JB, Steven AC. One number does not fit all: mapping local variations in resolution in cryo-EM reconstructions. J Struct Biol. 2013;184(2):226–36.

2. Luthra A, Paranagama N, Swinehart W, Bayooz S, Phan P, Quach V, Schiffer JM, Stec B, Iwata-Reuyl D, Swairjo MA. Conformational communication mediates the reset step in t^6A biosynthesis. Nucleic Acids Research. 2019;47(12):6551–67.

3. Suzuki T. The expanding world of tRNA modifications and their disease relevance. Nat Rev Mol Cell Biol. 2021;22(6):375–92.

4. Sylvers LA, Rogers KC, Shimizu M, Ohtsuka E, Soll D. A 2-thiouridine derivative in tRNAGlu is a positive determinant for aminoacylation by Escherichia coli glutamyl-tRNA synthetase. Biochemistry. 1993;32(15):3836–41.

5. Muramatsu T, Nishikawa K, Nemoto F, Kuchino Y, Nishimura S, Miyazawa T, Yokoyama S. Codon and Amino-Acid Specificities of a Transfer RNA are Both Converted by a Single Post-Transcriptional Modification. Nature. 1988;336:179–81.

6. Senger B, Auxilien S, Englisch U, Cramer F, Fasiolo F. The modified wobble base inosine in yeast tRNAIle is a positive determinant for aminoacylation by isoleucyl-tRNA synthetase. Biochemistry. 1997;36(27):8269–75.

7. Thiaville PC, El Yacoubi B, Kohrer C, Thiaville JJ, Deutsch C, Iwata-Reuyl D, Bacusmo JM, Armengaud J, Bessho Y, Wetzel C, Cao X, Limbach PA, RajBhandary UL, de Crécy-Lagard V. Essentiality of threonylcarbamoyladenosine (t^6A), a universal tRNA modification, in bacteria. Mol Microbiol. 2015;98(6):1199–221.

8. Suzuki T, Ueda T, Watanabe K. The 'polysemous' codon--a codon with multiple amino acid assignment caused by dual specificity of tRNA identity. EMBO J. 1997;16(5):1122–34.

9. Czerwoniec A, Dunin-Horkawicz S, Purta E, Kaminska KH, Kasprzak JM, Bujnicki JM, Grosjean H, Rother K. MODOMICS: a database of RNA modification pathways. 2008 update. Nucleic Acids Research. 2009;37:D118–D21.

10. Pan T. Modifications and functional genomics of human transfer RNA. Cell Res. 2018;28(4):395–404.

11. Väre VYP, Eruysal ER, Narendran A, Sarachan KL, Agris PF. Chemical and Conformational Diversity of Modified Nucleosides Affects tRNA Structure and Function. Biomolecules. 2017;7(1):29.

12. Yarian C, Townsend H, Czestkowski W, Sochacka E, Malkiewicz AJ, Guenther R, Miskiewicz A, Agris PF. Accurate translation of the genetic code depends on tRNA modified nucleosides. JBC. 2002;277(19):16391–5.

13. Crick FH. Codon--anticodon pairing: the wobble hypothesis. J Mol Biol. 1966;19(2):548–55.

14. Schweizer U, Bohleber S, Fradejas-Villar N. The modified base isopentenyladenosine and its derivatives in tRNA. RNA Biol. 2017;14(9):1197–208.

15. Pavlakis SG, Phillips PC, DiMauro S, De Vivo DC, Rowland LP. Mitochondrial myopathy, encephalopathy, lactic acidosis, and strokelike episodes: a distinctive clinical syndrome. Ann Neurol. 1984;16(4):481–8.

16. Fukuhara N, Tokiguchi S, Shirakawa K, Tsubaki T. Myoclonus epilepsy associated with ragged-red fibres (mitochondrial abnormalities): disease entity or a syndrome? Light-and electron-microscopic studies of two cases and review of literature. J Neurol Sci. 1980;47(1):117–33.

17. Goto Y-i, Nonaka I, Horai S. A Mutation in the $tRNA^{Leu(UUR)}$ Gene Associated with the MELAS Subgroup of Mitochondrial Encephalomyopathies. Nature. 1990;348(6302):651–3.

18. Shoffner JM, Lott MT, Lezza AM, Seibel P, Ballinger SW, Wallace DC. Myoclonic epilepsy and ragged-red fiber disease (MERRF) is associated with a mitochondrial DNA tRNA(Lys) mutation. Cell. 1990;61(16):931–7.

19. Suzuki T, Yashiro Y, Kikuchi I, Ishigami Y, Saito H, Matsuzawa I, Okada S, Mito M, Iwasaki S, Ma D, Zhao X, Asano K, Lin H, Kirino Y, Sakaguchi Y, Suzuki T. Complete chemical structures of human mitochondrial tRNAs. Nature Communications. 2020;11(1):4269.

20. Suzuki T, Nagao A, Suzuki T. Human mitochondrial diseases caused by lack of taurine modification in mitochondrial tRNAs. Wiley Interdiscip Rev RNA. 2011;2(3):376–86.

21. Yasukawa T, Suzuki T, Ishii N, Ohta S, Watanabe K. Wobble modification defect in tRNA disturbs codon-anticodon interaction in a mitochondrial disease. EMBO J. 2001;20(17):4794–802.

22. Parthasarathy R, Ohrt JM, Chheda GB. Modified nucleosides and conformation of anticodon loops: crystal structure of t6A and g6A. Biochemistry. 1977;16(23):4999–5008.

23. Adamiak RW, Biala E, Grzeskowiak K, Kierzek R, Kraszewski A, Markiewicz WT, Okupniak J, Stawinski J, Wiewiorowski M. The chemical synthesis of the anticodon loop of an eukaryotic initiator tRNA containing the hypermodified nucleoside N6-/N-threonylcarbonyl/-adenosine/t6A/1. Nucleic Acids Res. 1978;5(6):1889–905.

24. Zhang W, Westhof E. The Biology of tRNA t(6)A Modification and Hypermodifications-Biogenesis and Disease Relevance. J Mol Biol. 2025;437(16):169091.

25. Yarian C, Marszalek M, Sochacka E, Malkiewicz A, Guenther R, Miskiewicz A, Agris PF. Modified nucleoside dependent Watson-Crick and wobble codon binding by tRNALysUUU species. Biochemistry. 2000;39(44):13390–5.

26. Joshi K, Bhatt MJ, Farabaugh PJ. Codon-specific effects of tRNA anticodon loop modifications on translational misreading errors in the yeast Saccharomyces cerevisiae. Nucleic Acids Research. 2018;46(19):10331–9.

27. Nureki O, Niimi T, Muramatsu T, Kanno H, Kohno T, Florentz C, Giege R, Yokoyama S. Molecular recognition of the identity-determinant set of isoleucine transfer RNA from *Escherichia coli*. Journal of Molecular Biology. 1994;236:710–24.

28. Lin H, Miyauchi K, Harada T, Okita R, Takeshita E, Komaki H, Fujioka K, Yagasaki H, Goto Y-i, Yanaka K, Nakagawa S, Sakaguchi Y, Suzuki T. CO2-sensitive tRNA modification associated with human mitochondrial disease. Nature Communications. 2018;9(1):1875.

29. Zhang Y, Zhou JB, Yin Y, Wang ED, Zhou XL. Multifaceted roles of t6A biogenesis in efficiency and fidelity of mitochondrial gene expression. Nucleic Acids Res. 2024;52(6):3213–33.

30. Wang J-T, Zhou J-B, Mao X-L, Zhou L, Chen M, Zhang W, Wang E-D, Zhou X-L. Commonality and diversity in tRNA substrate recognition in t6A biogenesis by eukaryotic KEOPSs. Nucleic Acids Research. 2022;50(4):2223–39.

31. Rozov A, Demeshkina N, Khusainov I, Westhof E, Yusupov M, Yusupova G. Novel base-pairing interactions at the tRNA wobble position crucial for accurate reading of the genetic code. Nat Commun. 2016;7:10457.

32. Murphy FVt, Ramakrishnan V, Malkiewicz A, Agris PF. The role of modifications in codon discrimination by tRNA(Lys)^{UUU}. Nat Struct Mol Biol. 2004;11(12):1186–91.

33. Rozov A, Westhof E, Yusupov M, Yusupova G. The ribosome prohibits the G*U wobble geometry at the first position of the codon-anticodon helix. Nucleic Acids Res. 2016;44(13):6434–41.

34. Seelam Prabhakar P, Takyi NA, Wetmore SD. Posttranscriptional modifications at the 37th position in the anticodon stem-loop of tRNA: structural insights from MD simulations. RNA. 2021;27(2):202–20.

35. Weiss MC, Sousa FL, Mrnjavac N, Neukirchen S, Roettger M, Nelson-Sathi S, Martin WF. The physiology and habitat of the last universal common ancestor. Nat Microbiol. 2016;1(9):16116.

36. Schneider C, Becker S, Okamura H, Crisp A, Amatov T, Stadlmeier M, Carell T. Noncanonical RNA Nucleosides as Molecular Fossils of an Early Earth-Generation by Prebiotic Methylations and Carbamoylations. Angew Chem Int Ed Engl. 2018;57(20):5943–6.

37. Grosjean H, Westhof E. An integrated, structure- and energy-based view of the genetic code. Nucleic Acids Res. 2016;44(17):8020–40.

38. Galperin MY, Koonin EV. 'Conserved hypothetical' proteins: prioritization of targets for experimental study. Nucl Acids Res. 2004;32(18):5452–63.

39. Jin M, Zhang Z, Yu Z, Chen W, Wang X, Lei D, Zhang W. Structure–function analysis of an ancient TsaD–TsaC–SUA5–TcdA modular enzyme reveals a prototype of tRNA t6A and ct6A synthetases. Nucleic Acids Research. 2023;51(16):8711–29.

40. de Crecy-Lagard V. The universal YrdC/Sua5 family is required for the formation of threonylcarbamoyladenosine in tRNA. J Biol Chem. 2009;37(9):2894–909.

41. Deutsch C, El Yacoubi B, de Crécy-Lagard V, Iwata-Reuyl D. Biosynthesis of threonylcarbamoyl adenosine (t^6A), a universal tRNA nucleoside. Journal of Biological Chemistry. 2012;287(17):13666–73.

42. Lauhon CT. Mechanism of N6-Threonylcarbamoyladenonsine (t^6A) Biosynthesis: Isolation and Characterization of the Intermediate Threonylcarbamoyl-AMP. Biochemistry. 2012;51(44):8950–63.

43. Thiaville PC, El Yacoubi B, Perrochia L, Hecker A, Prigent M, Thiaville JJ, Forterre P, Namy O, Basta T, de Crécy-Lagard V. Cross kingdom functional conservation of the core universally conserved threonylcarbamoyladenosine tRNA synthesis enzymes. Eukaryot Cell. 2014;13(9):1222–31.

44. Thiaville PC, Iwata-Reuyl D, de Crecy-Lagard V. Diversity of the biosynthesis pathway for threonylcarbamoyladenosine (t^6A), a universal modification of tRNA. RNA Biol. 2014;11(12):1529–39.

45. Pichard-Kostuch A, Da Cunha V, Oberto J, Sauguet L, Basta T. The universal Sua5/TsaC family evolved different mechanisms for the synthesis of a key tRNA modification. Front Microbiol. 2023;14:1204045.

46. Perrochia L, Guetta D, Hecker A, Forterre P, Basta T. Functional assignment of KEOPS/EKC complex subunits in the biosynthesis of the universal t^6A tRNA modification. Nucleic Acids Research. 2013;4(20):9484–99.

47. Srinivasan M, Mehta P, Yu Y, Prugar E, Koonin EV, Karzai AW, Sternglanz R. The highly conserved KEOPS/EKC complex is essential for a universal tRNA modification, t^6A. The EMBO Journal. 2011;30:873–81.

48. Daugeron M-C, Lenstra TL, Frizzarin M, El Yacoubi B, Liu X, Baudin-Baillieu A, Lijnzaad P, Decourty L, Saveanu C, Jacquier A, Holstege FCP, de Crécy-Lagard V, van Tilbeurgh H, Libri D. Gcn4 misregulation reveals a direct role for the evolutionary conserved EKC/KEOPS in the t^6A modification of tRNAs. Nucleic Acids Research. 2011;39(14):6148–60.

49. Wu P, Gan Q, Zhang X, Yang Y, Xiao Y, She Q, Ni J, Huang Q, Shen Y. The archaeal KEOPS complex possesses a functional Gon7 homolog and has an essential function independent of the cellular t(6)A modification level. mLife. 2023;2(1):11–27.

50. Wan LC, Mao DY, Neculai D, Strecker J, Chiovitti D, Kurinov I, Poda G, Thevakumaran N, Yuan F, Szilard RK, Lissina E, Nislow C, Caudy AA, Durocher D, Sicheri F. Reconstitution and characterization of eukaryotic N6-threonylcarbamoylation of tRNA using a minimal enzyme system. Nucleic Acids Research. 2013.

51. Zhang W, Collinet B, Perrochia L, Durand D, van Tilbeurgh H. The ATP-mediated formation of the YgjD–YeaZ–YjeE complex is required for the biosynthesis of tRNA t^6A in *Escherichia coli*. Nucleic Acids Research. 2015;43(3):1804–17.

52. Nichols CE, Lamb HK, Thompson P, Omari KE, Lockyer M, Charles I, Hawkins AR, Stammers DK. Crystal structure of the dimer of two essential *Salmonella typhimurium* proteins, YgjD & YeaZ and calorimetric evidence for the formation of a ternary YgjD–YeaZ–YjeE complex. Protein Science. 2013;22(5):628–40.

53. Luthra A, Swinehart W, Bayooz S, Phan P, Stec B, Iwata-Reuyl D, Swairjo MA. Structure and mechanism of a bacterial t^6A biosynthesis system. Nucleic Acids Research. 2018;46(3):1395–411.

54. Lu S, Jin M, Yu Z, Zhang W. Structure-function analysis of tRNA t(6)A-catalysis, assembly, and thermostability of Aquifex aeolicus TsaD(2)B(2) tetramer in complex with TsaE. J Biol Chem. 2024;300(12):107962.

55. Koonin EV. A common set of conserved motifs in a vast variety of putative nucleic acid-dependent ATPases including MCM proteins involved in the initiation of eukaryotic DNA replication. Nucleic Acids Res. 1993;21(11):2541–7.

56. Kimura S, Miyauchi K, Ikeuchi Y, Thiaville PC, Crecy-Lagard V, Suzuki T. Discovery of the beta-barrel-type RNA methyltransferase responsible for N6-methylation of N6-threonylcarbamoyladenosine in tRNAs. Nucleic Acids Res. 2014;42(14):9350–65.

57. Rak R, Polonsky M, Eizenberg-Magar I, Mo Y, Sakaguchi Y, Mizrahi O, Nachshon A, Reich-Zeliger S, Stern-Ginossar N, Dahan O, Suzuki T, Friedman N, Pilpel Y. Dynamic changes in tRNA modifications and abundance during T cell activation. Proc Natl Acad Sci U S A. 2021;118(42).

58. Kang BI, Miyauchi K, Matuszewski M, D'Almeida GS, Rubio MAT, Alfonzo JD, Inoue K, Sakaguchi Y, Suzuki T, Sochacka E, Suzuki T. Identification of 2-methylthio cyclic N6-threonylcarbamoyladenosine (ms2ct6A) as a novel RNA modification at position 37 of tRNAs. Nucleic Acids Res. 2017;45(4):2124–36.

59. Wei F, Suzuki T, Watanabe S, Kimura S. Deficit of $tRNA^{Lys}$ modification by Cdkal1 causes the development of type 2 diabetes in mice Journal of clinical investigation. 2011;121(3598–3608).

60. Miyauchi K, Kimura S, Suzuki T. A cyclic form of N6-threonylcarbamoyladenosine as a widely distributed tRNA hypermodification. Nat Chem Biol. 2013;9(2):105–11.

61. Nagao A, Ohara M, Miyauchi K, Yokobori SI, Yamagishi A, Watanabe K, Suzuki T. Hydroxylation of a conserved tRNA modification establishes non-universal genetic code in echinoderm mitochondria. Nat Struct Mol Biol. 2017;24(9):778–82.

62. Yu N, Jora M, Solivio B, Thakur P, Acevedo-Rocha CG, Randau L, de Crécy-Lagard V, Addepalli B, Limbach PA. tRNA Modification Profiles and Codon-Decoding Strategies in Methanocaldococcus jannaschii. Journal of bacteriology. 2019;201(9):e00690–18.

63. Reddy DM, Crain PF, Edmonds CG, Gupta R, Hashizume T, Stetter KO, Widdel F, McCloskey JA. Structure determination of two new amino acid-containing derivatives of adenosine from tRNA of thermophilic bacteria and archaea. Nucleic Acids Res. 1992;20(21):5607–15.

64. Wolff P, Villette C, Zumsteg J, Heintz D, Antoine L, Chane-Woon-Ming B, Droogmans L, Grosjean H, Westhof E. Comparative patterns of modified nucleotides in individual tRNA species from a mesophilic and two thermophilic archaea. RNA. 2020;26(12):1957–75.

65. Swinehart WE, Deutsch CW, Sarachan KL, Luthra A, Bacusmo JM, de Crécy-Lagard V, Swairjo MA, Agris PF, Iwata-Reuyl D. Specificity in the Biosynthesis of the Universal tRNA Nucleoside N6-Threonylcarbamoyl Adenosine (t6A) - TsaD is the Gatekeeper. RNA. 2020.

66. Edvardson S, Prunetti L, Arraf A, Haas D, Bacusmo JM, Hu JF, Ta-Shma A, Dedon PC, de Crecy-Lagard V, Elpeleg O. tRNA N6-adenosine threonylcarbamoyltransferase defect due to KAE1/TCS3 (OSGEP) mutation manifest by neurodegeneration and renal tubulopathy. Eur J Hum Genet. 2017;25(5):545–51.

67. Braun DA, Rao J, Mollet G, Schapiro D, Daugeron MC, Tan W, Gribouval O, Boyer O, Revy P, Jobst-Schwan T, Schmidt JM, Lawson JA, Schanze D, Ashraf S, Ullmann JFP, Hoogstraten CA, Boddaert N, Collinet B, Martin G, Liger D, Lovric S, Furlano M, Guerrera IC, Sanchez-Ferras O, Hu JF, Boschat AC, Sanquer S, Menten B, Vergult S, De Rocker N, Airik M, Hermle T, Shril S, Widmeier E, Gee HY, Choi WI, Sadowski CE, Pabst WL, Warejko JK, Daga A, Basta T, Matejas V, Scharmann K, Kienast SD, Behnam B, Beeson B, Begtrup A, Bruce M, Ch'ng GS, Lin SP, Chang JH, Chen CH, Cho MT, Gaffney PM, Gipson PE, Hsu CH, Kari JA, Ke YY, Kiraly-Borri C, Lai WM, Lemyre E, Littlejohn RO, Masri A, Moghtaderi M, Nakamura K, Ozaltin F, Praet M, Prasad C, Prytula A, Roeder ER, Rump P, Schnur RE, Shiihara T, Sinha MD, Soliman NA, Soulami K, Sweetser DA, Tsai WH, Tsai JD, Topaloglu R, Vester U, Viskochil DH, Vatanavicharn N, Waxler JL, Wierenga KJ, Wolf MTF, Wong SN, Leidel SA, Truglio G, Dedon PC, Poduri A, Mane S, Lifton RP, Bouchard M, Kannu P, Chitayat D, Magen

D, Callewaert B, van Tilbeurgh H, Zenker M, Antignac C, Hildebrandt F. Mutations in KEOPS-complex genes cause nephrotic syndrome with primary microcephaly. Nat Genet. 2017;49(10):1529–38.

68. Arrondel C, Missoury S, Snoek R, Patat J, Menara G, Collinet B, Liger D, Durand D, Gribouval O, Boyer O, Buscara L, Martin G, Machuca E, Nevo F, Lescop E, Braun DA, Boschat A-C, Sanquer S, Guerrera IC, Revy P, Parisot M, Masson C, Boddaert N, Charbit M, Decramer S, Novo R, Macher M-A, Ranchin B, Bacchetta J, Laurent A, Collardeau-Frachon S, van Eerde AM, Hildebrandt F, Magen D, Antignac C, van Tilbeurgh H, Mollet G. Defects in t6A tRNA modification due to GON7 and YRDC mutations lead to Galloway-Mowat syndrome. Nature Communications. 2019;10(1):3967.

69. Thiaville PC, Legendre R, Rojas-Benitez D, Baudin-Baillieu A, Hatin I, Chalancon G, Glavic A, Namy O, de Crécy-Lagard V. Global translational impacts of the loss of the tRNA modification t^6A in yeast. Microb Cell. 2016;3(1):29–45.

70. Pollo-Oliveira L, Klassen R, Davis N, Ciftci A, Bacusmo JM, Martinelli M, DeMott MS, Begley TJ, Dedon PC, Schaffrath R, de Crécy-Lagard V. Loss of Elongator- and KEOPS-Dependent tRNA Modifications Leads to Severe Growth Phenotypes and Protein Aggregation in Yeast. Biomolecules. 2020;10(2):E322.

71. Rojas-Benitez D, Thiaville PC, de Crécy-Lagard V, Glavic A. The Levels of a Universally Conserved tRNA Modification Regulate Cell Growth. The Journal of biological chemistry. 2015;290(30):18699–707.

72. Handford JI, Ize B, Buchanan G, Butland GP, Greenblatt J, Emili A, Palmer T. Conserved Network of Proteins Essential for Bacterial Viability. J Bacteriol. 2009;191(15):4732–49.

73. Tsui HT, Chan CK, Yuan Y, Elias R, Sun J, Marchand V, Jaroch M, Sun G, Manzoor I, Kutchuashvili A, Leszczynska G, Seaton K, Motorin Y, Rice K, Swairjo M, Dedon PC, Winkler ME, de Crecy-Lagard V. tRNA modification landscapes in streptococci: shared losses and clade-specific adaptations. Open Biol. 2026;16(4).

74. Bitoun JP, Liao S, Xie GG, Beatty WL, Wen ZT. Deficiency of BrpB causes major defects in cell division, stress responses and biofilm formation by Streptococcus mutans. Microbiology (Reading, England). 2014;160(Pt 1):67–78.

75. Nguyen HA, El Khoury T, Guiral S, Laaberki MH, Candusso MP, Galisson F, Foucher AE, Kesraoui S, Ballut L, Vallet S, Orelle C, Zucchini L, Martin J, Page A, Attieh J, Aghajari N, Grangeasse C, Jault JM. Expanding the Kinome World: A New Protein Kinase Family Widely Conserved in Bacteria. J Mol Biol. 2017;429(20):3056–74.

76. Suzuki T, Nakamura A, Kato K, Soll D, Tanaka I, Sheppard K, Yao M. Structure of the Pseudomonas aeruginosa transamidosome reveals unique aspects of bacterial tRNA-dependent asparagine biosynthesis. Proc Natl Acad Sci U S A. 2015;112(2):382–7.

77. Devarkar Swapnil C, Budding Christina R, Pathirage C, Kavoor A, Herbert C, Limbach Patrick A, Musier-Forsyth K, Xiong Y. Structural basis for aminoacylation of cellular modified tRNALys3 by human lysyl-tRNA synthetase. Nucleic Acids Res. 2025;53(5).

78. Jumper J, Evans R, Pritzel A, Green T, Figurnov M, Ronneberger O, Tunyasuvunakool K, Bates R, Žídek A, Potapenko A, Bridgland A, Meyer C, Kohl SAA, Ballard AJ, Cowie A, Romera-Paredes B, Nikolov S, Jain R, Adler J, Back T, Petersen S, Reiman D, Clancy E, Zielinski M, Steinegger M, Pacholska M, Berghammer T, Bodenstein S, Silver D, Vinyals O, Senior AW, Kavukcuoglu K, Kohli P, Hassabis D. Highly accurate protein structure prediction with AlphaFold. Nature. 2021;596(7873):583–9.

79. Lerner CG, Hajduk PJ, Wagner R, Wagenaar FL, Woodall C, Gu YG, Searle XB, Florjancic AS, Zhang T, Clark RF, Cooper CS, Mack JC, Yu L, Cai M, Betz SF, Chovan LE, McCall JO, Black-Schaefer CL, Kakavas SJ, Schurdak ME, Comess KM, Walter KA, Edalji R, Dorwin SA, Smith RA, Hebert EJ, Harlan JE, Metzger RE, Merta PJ, Baranowski JL, Coen ML, Thornewell SJ, Shivakumar AG, Saiki AY, Soni N, Bui M, Balli DJ, Sanders WJ, Nilius AM, Holzman TF, Fesik SW, Beutel BA. From bacterial genomes to novel antibacterial agents: discovery, characterization, and antibacterial activity of compounds that bind to HI0065 (YjeE) from Haemophilus influenzae. Chem Biol Drug Des. 2007;69(6):395–404.

80. Agari Y, Sato S, Wakamatsu T, Bessho Y, Ebihara A, Yokoyama S, Kuramitsu S, Shinkai A. X-ray crystal structure of a hypothetical Sua5 protein from Sulfolobus tokodaii strain 7. Proteins: Structure, Function, and Bioinformatics. 2008;70(3):1108–11.

81. Kuratani M, Kasai T, Akasaka R, Higashijima K, Terada T, Kigawa T, Shinkai A, Bessho Y, Yokoyama S. Crystal structure of *Sulfolobus tokodaii* Sua5 complexed with L-threonine and AMPPNP. Proteins. 2011;79(7):2065–75.

82. Pichard-Kostuch A, Zhang W, Liger D, Daugeron MC, Letoquart J, Li de la Sierra-Gallay I, Forterre P, Collinet B, van Tilbeurgh H, Basta T. Structure-function analysis of Sua5 protein reveals novel functional motifs required for the biosynthesis of the universal t(6)A tRNA modification. Rna. 2018;24(7):926–38.

83. Minor W, Cymborowski M, Otwinowski Z, Chruszcz M. HKL-3000: the integration of data reduction and structure solution--from diffraction images to an initial model in minutes. Acta Crystallogr D Biol Crystallogr. 2006;62(Pt 8):859–66.

84. Kabsch W. XDS. Acta Crystallographica Section D. 2010;66(2):125–32.

85. McCoy AJ, Grosse-Kunstleve RW, Adams PD, Winn MD, Storoni LC, Read RJ. Phaser crystallographic software. J Appl Crystallogr. 2007;40:658–74.

86. Emsley P, Lohkamp B, Scott WG, Cowtan K. Features and development of Coot. Acta Crystallogr D Biol Crystallogr. 2010;66(Pt 4):486–501.

87. Murshudov GN, Skubak P, Lebedev AA, Pannu NS, Steiner RA, Nicholls RA, Winn MD, Long F, Vagin AA. REFMAC5 for the refinement of macromolecular crystal structures. Acta Crystallogr D Biol Crystallogr. 2011;67(Pt 4):355–67.

88. Rosenberg DJ, Hura GL, Hammel M. Size exclusion chromatography coupled small angle X-ray scattering with tandem multiangle light scattering at the SIBYLS beamline. Methods Enzymol. 2022;677:191–219.

89. Classen S, Hura GL, Holton JM, Rambo RP, Rodic I, McGuire PJ, Dyer K, Hammel M, Meigs G, Frankel KA, Tainer JA. Implementation and performance of SIBYLS: a dual endstation small-angle X-ray scattering and macromolecular crystallography beamline at the Advanced Light Source. J Appl Crystallogr. 2013;46(Pt 1):1–13.

90. Hopkins JB, Gillilan RE, Skou S. BioXTAS RAW: improvements to a free open-source program for small-angle X-ray scattering data reduction and analysis. J Appl Crystallogr. 2017;50(Pt 5):1545–53.

91. Svergun D. Determination of the regularization parameter in indirect-transform methods using perceptual criteria. J Appl Crystallogr. 1992;25(4):495–503.

92. Manalastas-Cantos K, Konarev PV, Hajizadeh NR, Kikhney AG, Petoukhov MV, Molodenskiy DS, Panjkovich A, Mertens HDT, Gruzinov A, Borges C, Jeffries CM, Svergun DI, Franke D. ATSAS 3.0: expanded functionality and new tools for small-angle scattering data analysis. J Appl Crystallogr. 2021;54(Pt 1):343–55.

93. Piiadov V, Ares de Araújo E, Oliveira Neto M, Craievich AF, Polikarpov I. SAXSMoW 2.0: Online calculator of the molecular weight of proteins in dilute solution from experimental SAXS data measured on a relative scale. Protein Sci. 2019;28(2):454–63.

94. Schneidman-Duhovny D, Hammel M, Tainer JA, Sali A. FoXS, FoXSDock and MultiFoXS: Single-state and multi-state structural modeling of proteins and their complexes based on SAXS profiles. Nucleic Acids Research. 2016;44(W1):W424–W9.

95. Yuki Yamamoto J-yH, Yoshikatsu Ito. Kinetic investigation on carbamate formation from the reaction of carbon dioxide with amino acids in homogeneous aqueous solution. Journal of Physical Organic Chemistry 2012;25(3):239–47.

96. Morin A, Auxilien S, Senger B, Tewari R, Grosjean H. Structural requirements for enzymatic formation of threonylcarbamoyladenosine (t^6A) in tRNA: an *in vivo* study with *Xenopus laevis* oocytes. RNA. 1998;4(1):24–37.

97. Su C, Jin M, Zhang W. Conservation and Diversification of tRNA t(6)A-Modifying Enzymes across the Three Domains of Life. Int J Mol Sci. 2022;23(21).

98. Zheng X, Su C, Duan L, Jin M, Sun Y, Zhu L, Zhang W. Molecular basis of A. thaliana KEOPS complex in biosynthesizing tRNA t6A. Nucleic Acids Res. 2024;52(8):4523–40.

99. Zhou J-B, Wang Y, Zeng Q-Y, Meng S-X, Wang E-D, Zhou X-L. Molecular basis for t6A modification in human mitochondria. Nucleic Acids Research. 2020.

100. Wang Y, Zeng Q-Y, Zheng W-Q, Ji Q-Q, Zhou X-L, Wang E-D. A natural non-Watson-Crick base pair in human mitochondrial tRNAThr causes structural and functional susceptibility to local mutations. Nucleic acids research. 2018;46(9):4662–76.

101. Chuquimarca SMO, Beenstock J, Daou S, Porat J, Keszei AFA, Yin JZ, Beschauner T, Bayfield MA, Mazhab-Jafari MT, Sicheri F. Author Correction: Structures of KEOPS bound to tRNA reveal functional roles of the kinase Bud32. Nature Communications. 2025;16(1):6810.

102. Ona Chuquimarca SM, Beenstock J, Daou S, Porat J, Keszei AFA, Yin JZ, Beschauner T, Bayfield MA, Mazhab-Jafari MT, Sicheri F. Structures of KEOPS bound to tRNA reveal functional roles of the kinase Bud32. Nat Commun. 2024;15(1):10633.

103. Beenstock J, Ona SM, Porat J, Orlicky S, Wan LCK, Ceccarelli DF, Maisonneuve P, Szilard RK, Yin Z, Setiaputra D, Mao DYL, Khan M, Raval S, Schriemer DC, Bayfield MA, Durocher D, Sicheri F. A substrate binding model for the KEOPS tRNA modifying complex. Nat Commun. 2020;11(1):6233.

104. El Yacoubi B, Lyons B, Cruz Y, Reddy R, Nordin B, Agnelli F, Williamson JR, Schimmel PR, Swairjo MA, de Crécy-Lagard V. The universal YrdC/Sua5 family is required for the formation of threonylcarbamoyladenosine in tRNA. Nucleic Acids Research. 2009;37(9):2894–909.

105. Spears JL, Gaston KW, Alfonzo JD. Analysis of tRNA editing in native and synthetic substrates. Methods in molecular biology. 2011;718:209–26.

106. Chambers MC, Maclean B, Burke R, Amodei D, Ruderman DL, Neumann S, Gatto L, Fischer B, Pratt B, Egertson J, Hoff K, Kessner D, Tasman N, Shulman N, Frewen B, Baker TA, Brusniak M-Y, Paulse C, Creasy D, Flashner L, Kani K, Moulding C, Seymour SL, Nuwaysir LM, Lefebvre B, Kuhlmann F, Roark J, Rainer P, Detlev S, Hemenway T, Huhmer A, Langridge J, Connolly B, Chadick T, Holly K, Eckels J, Deutsch EW, Moritz RL, Katz JE, Agus DB, MacCoss M, Tabb DL, Mallick P. A cross-platform toolkit for mass spectrometry and proteomics. Nature Biotechnology. 2012;30(10):918–20.

107. Wein S, Andrews B, Sachsenberg T, Santos-Rosa H, Kohlbacher O, Kouzarides T, Garcia BA, Weisser H. A computational platform for high-throughput analysis of RNA sequences and modifications by mass spectrometry. Nature Communications. 2020;11(1):926.

108. Röst HL, Sachsenberg T, Aiche S, Bielow C, Weisser H, Aicheler F, Andreotti S, Ehrlich H-C, Gutenbrunner P, Kenar E, Liang X, Nahnsen S, Nilse L, Pfeuffer J, Rosenberger G, Rurik M, Schmitt U, Veit J, Walzer M, Wojnar D, Wolski WE, Schilling O, Choudhary JS, Malmström L, Aebersold R, Reinert K, Kohlbacher O. OpenMS: a flexible open-source software platform for mass spectrometry data analysis. Nature Methods. 2016;13(9):741–8.

109. Chan PP, Lowe TM. GtRNAdb 2.0: an expanded database of transfer RNA genes identified in complete and draft genomes. Nucleic Acids Research. 2015;44(D1):D184–D9.

110. Punjani A, Rubinstein JL, Fleet DJ, Brubaker MA. cryoSPARC: algorithms for rapid unsupervised cryo-EM structure determination. Nat Methods. 2017;14(3):290–6.

111. Tan YZ, Baldwin PR, Davis JH, Williamson JR, Potter CS, Carragher B, Lyumkis D. Addressing preferred specimen orientation in single-particle cryo-EM through tilting. Nature Methods. 2017;14(8):793–6.

112. Sanchez-Garcia R, Gomez-Blanco J, Cuervo A, Carazo JM, Sorzano COS, Vargas J. DeepEMhancer: a deep learning solution for cryo-EM volume post-processing. Commun Biol. 2021;4(1):874.

113. Sankaranarayanan R, Dock-Bregeon AC, Romby P, Caillet J, Springer M, Rees B, Ehresmann C, Ehresmann B, Moras D. The structure of threonyl-tRNA synthetase-tRNA(Thr) complex enlightens its repressor activity and reveals an essential zinc ion in the active site. Cell. 1999;97(3):371–81.

114. Abramson J, Adler J, Dunger J, Evans R, Green T, Pritzel A, Ronneberger O, Willmore L, Ballard AJ, Bambrick J, Bodenstein SW, Evans DA, Hung C-C, O'Neill M, Reiman D, Tunyasuvunakool K, Wu Z, Žemgulytė A, Arvaniti E, Beattie C, Bertolli O, Bridgland A, Cherepanov A, Congreve M, Cowen-Rivers AI, Cowie A, Figurnov M, Fuchs FB, Gladman H, Jain R, Khan YA, Low CMR, Perlin K, Potapenko A, Savy P, Singh S, Stecula A, Thillaisundaram A, Tong C, Yakneen S, Zhong ED, Zielinski M, Žídek A, Bapst V, Kohli P, Jaderberg M, Hassabis D, Jumper JM. Accurate structure prediction of biomolecular interactions with AlphaFold 3. Nature. 2024;630(8016):493–500.

115. Liebschner D, Afonine PV, Baker ML, Bunkóczi G, Chen VB, Croll TI, Hintze B, Hung LW, Jain S, McCoy AJ, Moriarty NW, Oeffner RD, Poon BK, Prisant MG, Read RJ, Richardson JS, Richardson DC, Sammito MD, Sobolev OV, Stockwell DH, Terwilliger TC, Urzhumtsev AG, Videau LL, Williams CJ, Adams PD. Macromolecular structure determination using X-rays, neutrons and electrons: recent developments in Phenix. Acta Crystallogr D Struct Biol. 2019;75(Pt 10):861–77.

116. Afonine PV, Poon BK, Read RJ, Sobolev OV, Terwilliger TC, Urzhumtsev A, Adams PD. Real-space refinement in PHENIX for cryo-EM and crystallography. Acta Crystallographica Section D. 2018;74(6):531–44.

117. Young JY, Westbrook JD, Feng Z, Sala R, Peisach E, Oldfield TJ, Sen S, Gutmanas A, Armstrong DR, Berrisford JM, Chen L, Chen M, Di Costanzo L, Dimitropoulos D, Gao G, Ghosh S, Gore S, Guranovic V, Hendrickx PMS, Hudson BP, Igarashi R, Ikegawa Y, Kobayashi N, Lawson CL, Liang Y, Mading S, Mak L, Mir MS, Mukhopadhyay A, Patwardhan A, Persikova I, Rinaldi L, Sanz-Garcia E, Sekharan MR, Shao C, Swaminathan GJ, Tan L, Ulrich EL, van Ginkel G, Yamashita R, Yang H, Zhuravleva MA, Quesada M, Kleywegt GJ, Berman HM, Markley JL, Nakamura H, Velankar S, Burley SK. OneDep: Unified wwPDB System for Deposition, Biocuration, and Validation of Macromolecular Structures in the PDB Archive. Structure. 2017;25(3):536–45.

118. Sherlin LD, Bullock TL, Nissan TA, Perona JJ, Lariviere FJ, Uhlenbeck OC, Scaringe SA. Chemical and enzymatic synthesis of tRNAs for high-throughput crystallization. Rna. 2001;7(11):1671–8.

119. Lyakhov DL, He B, Zhang X, Studier FW, Dunn JJ, McAllister WT. Mutant bacteriophage T7 RNA polymerases with altered termination properties. J Mol Biol. 1997;269(1):28–40.

120.Pei J, Kim B-H, Grishin NV. PROMALS3D: a tool for multiple protein sequence and structure alignments. Nucleic Acids Research. 2008;36(7):2295–300.

121.Missoury S, Plancqueel S, Li de la Sierra-Gallay I, Zhang W, Liger D, Durand D, Dammak R, Collinet B, van Tilbeurgh H. The structure of the TsaB/TsaD/TsaE complex reveals an unexpected mechanism for the bacterial t^6A tRNA-modification. Nucleic Acids Res. 2018.

122.Kopina BJ, Missoury S, Collinet B, Fulton MG, Cirio C, van Tilbeurgh H, Lauhon CT. Structure of a reaction intermediate mimic in t6A biosynthesis bound in the active site of the TsaBD heterodimer from Escherichia coli. Nucleic Acids Res. 2021;49(4):2141–60.

123.Abu Almakarem AS, Petrov AI, Stombaugh J, Zirbel CL, Leontis NB. Comprehensive survey and geometric classification of base triples in RNA structures. Nucleic Acids Res. 2012;40(4):1407–23.

124.Bick T, Dominiak PM, Wendler P. Exploiting the full potential of cryo-EM maps. BBA Adv. 2024;5:100113.

125.Auffinger P, Westhof E. Singly and bifurcated hydrogen-bonded base-pairs in tRNA anticodon hairpins and ribozymes. J Mol Biol. 1999;292(3):467–83.

126.Demeshkina N, Jenner L, Westhof E, Yusupov M, Yusupova G. A new understanding of the decoding principle on the ribosome. Nature. 2012;484(7393):256–9.

127.Olejniczak M, Uhlenbeck OC. tRNA residues that have coevolved with their anticodon to ensure uniform and accurate codon recognition. Biochimie. 2006;88(8):943–50.

128.Ashraf SS, Ansari G, Guenther R, Sochacka E, Malkiewicz A, Agris PF. The uridine in "U-turn": Contributions to tRNA-ribosomal binding. RNA. 1999;5(4):503–11.

129.Hattne J, Shi D, Glynn C, Zee C-T, Gallagher-Jones M, Martynowycz MW, Rodriguez JA, Gonen T. Analysis of Global and Site-Specific Radiation Damage in Cryo-EM. Structure. 2018;26(5):759–66.e4.

130.Zuker M. Mfold web server for nucleic acid folding and hybridization prediction. Nucleic Acids Res. 2003;31(13):3406–15.

131.Meynier V, Hardwick SW, Catala M, Roske JJ, Oerum S, Chirgadze DY, Barraud P, Yue WW, Luisi BF, Tisné C. Structural basis for human mitochondrial tRNA maturation. Nature communications. 2024;15(1):4683.

132.Abbassi NE, Jaciuk M, Scherf D, Böhnert P, Rau A, Hammermeister A, Rawski M, Indyka P, Wazny G, Chramiec-Głąbik A, Dobosz D, Skupien-Rabian B, Jankowska U, Rappsilber J, Schaffrath R, Lin TY, Glatt S. Cryo-EM structures of the human Elongator complex at work. Nature communications. 2024;15(1):4094.

133.Wan LC, Pillon MC, Thevakumaran N, Sun Y, Chakrabartty A, Guarne A, Kurinov I, Durocher D, Sicheri F. Structural and functional characterization of KEOPS dimerization by Pcc1 and its role in t6A biosynthesis. Nucleic Acids Res. 2016;44(14):6971–80.

134.Shomura Y, Higuchi Y. Structural basis for the reaction mechanism of S-carbamoylation of HypE by HypF in the maturation of [NiFe]-hydrogenases. J Biol Chem. 2012;287(34):28409–19.